

1

2

CONNECTING MICROBURST PRECIPITATION WITH ITS SCATTERING
MECHANISM

3

by

Mykhaylo Sergeevich Shumko

4

A dissertation submitted in partial fulfillment
of the requirements for the degree

of

Doctor of Philosophy

in

Physics

5

MONTANA STATE UNIVERSITY
Bozeman, Montana

December 2019

6

7

©COPYRIGHT

8

by

Mykhaylo Sergeevich Shumko

2019

All Rights Reserved

DEDICATION

⁹ I dedicate this to all MSU students who use L^AT_EX. Dedication is optional
¹⁰ and may be no longer than one page, single spaced, and should precede the
¹¹ acknowledgments page.

ACKNOWLEDGEMENTS

¹² I would like acknowledge the countless engineers, technicians, and scientists who
¹³ made the FIREBIRD, AC-6, and RBSP missions a success. This work was supported
¹⁴ by Montana State University and by NASA Headquarters under the NASA Earth and
¹⁵ Space Science Fellowship Program - Grant 80NSSC18K1204. **Add co-author support.**

TABLE OF CONTENTS

16	1. INTRODUCTION	1
17	Particle Populations and Their Interractions in the Magnetosphere	3
18	Populations in the Inner Magnetosphere	5
19	Plasmasphere.....	7
20	Ring Current	9
21	Radiation Belts.....	9
22	Charged Particle Motion in Electric and Magnetic Fields	13
23	Radiation Belt Particle Sources and Sinks	18
24	Adiabatic Heating	20
25	Wave Resonance Heating	20
26	Particle Losses	23
27	Microbursts	25
28	Scope of Reserach	31
29	2. CHAPTER TWO	
30	EVIDENCE OF MICROBURSTS OBSERVED NEAR THE EQUA-	
31	TORIAL PLANE IN THE OUTER VAN ALLEN RADIATION	
32	BELT	33
33	Contribution of Authors and Co-Authors	33
34	Manuscript Information	34
35	Key Points	35
36	Abstract	35
37	Introduction	35
38	Spacecraft Instrumentation	38
39	Observations	39
40	Analysis	42
41	Microburst and Source PSD	42
42	Motion of resonant electrons in phase space	45
43	Comparing the microburst PSD to diffusion theory	48
44	Discussion and Conclusions	50
45	Acknowledgments	51
46	3. CHAPTER THREE	
47	MICROBURST SCALE SIZE DERIVED FROM MULTIPLE BOUNCES	
48	OF A MICROBURST SIMULTANEOUSLY OBSERVED WITH	
49	THE FIREBIRD-II CUBESATS	53
50	Contribution of Authors and Co-Authors	53

TABLE OF CONTENTS – CONTINUED

51	Manuscript Information	54
52	Key Points	55
53	Abstract	55
54	Introduction	56
55	Spacecraft and Observation	58
56	Analysis.....	61
57	Electron Bounce Period	62
58	Microburst Energy Spectra	64
59	Microburst Scale Sizes	64
60	Discussion and Conclusions	67
61	Acknowledgments	69
62	4. CHAPTER FOUR	
63	MICROBURST SIZE DISTRIBUTION DERIVED WITH AEROCUBE-	
64	6	70
65	Contribution of Authors and Co-Authors	70
66	Manuscript Information	71
67	Key Points	72
68	Abstract	72
69	Introduction	73
70	Instrumentation.....	76
71	Methodology	77
72	Microburst Detection.....	77
73	Microburst Size Distribution in LEO and Magnetic Equator	79
74	Modeling the Distribution of Microburst Sizes	85
75	Monte Carlo and Analytic Models to Calculate $\bar{F}(s)$	85
76	Methods for estimating optimal θ parameters.....	86
77	Estimating optimal parameters for various microburst size models.....	89
78	Discussion	91
79	Conclusions	96
80	Acknowledgments	97
82	5. CONCLUSIONS AND FUTURE WORK	98
83	Future work	99
84	Future missions	101
85	REFERENCES CITED	103

TABLE OF CONTENTS – CONTINUED

⁸⁶	APPENDIX: Appendix A.....	113
⁸⁷	APPENDIX: Appendix B.....	116
⁸⁸	APPENDIX: Appendix C.....	124

LIST OF TABLES

Table		Page
89	C.1 Range of log-normal model parameters consistent 90 with the observed AC6 $\bar{F}(s)$	127
91	C.2 Range of Weibull model parameters consistent with 92 the observed AC6 $\bar{F}(s)$	127

LIST OF FIGURES

Figure		Page
93	1.1 A few macroscopic structures in the magnetosphere. The magnetosphere boundary with the solar wind is the magnetopause. The magnetotail consists of two lobes that contain Earth's magnetic flux with the plasma sheet separating the two lobes. The inner magnetosphere contains the plasmasphere, the ring current, and the radiation belts which are co-located.
94	Figure from Baumjohann and Treumann (1997).....	4
95		
96		
97		
98		
99		
100		
101	1.2 The dipole coordinate system. The magnetic latitude of \mathbf{r} is λ . The radial distance to a magnetic field line in the equatorial plane is typically given by $L = r_{eq}/R_e$. Figure from Baumjohann and
102	Treumann (1997).	6
103		
104		
105		
106	1.3 Equipotential lines and electric field arrows due to the superposition of the co-rotation and convection electric fields. Electrons in the shaded region execute closed orbits. Outside of the shaded regions the electrons are not trapped and will escape. The region separating the two regimes is called the Alfvén layer. Figure from Baumjohann and Treumann (1997).....	8
107		
108		
109		
110		
111		
112		

LIST OF FIGURES – CONTINUED

Figure	Page
113 1.4 The DST index during the St. Patrick's Day 2015 114 storm. This storm was caused by a coronal mass 115 ejection on March 15th, 2015. The storm phases 116 are: initial phase, main phase, and recovery phase. 117 The initial phase occurred when the Dst peaked 118 at +50 nT on March 17th during which the ring 119 current was eroded by the coronal mass ejection 120 during the interval shown by the red bar shown 121 at the bottom. Then the following rapid decrease 122 to ≈ -200 nT was during the main phase where 123 many injections from the magnetotail enhanced the 124 ring current, which reduced Earth's magnetic field 125 strength at the ground, and is shown with the green 126 bar. Lastly, the recovery phase lasted from March 127 18th to approximately March 29th during which the 128 ring current particles were lost and the ring current 129 returned to its equilibrium state. The recovery phase 130 is shown with the blue bar.	10
131 1.5 The two radiation belts with a the locations of 132 various satellites and orbits. Figure from (Horne 133 et al., 2013).	11
134 1.6 The dynamics of the outer radiation belt in 1997 135 from the POLAR satellite. Top panel shows the 1.2- 136 2.4 MeV electron flux as a function of L and 1997 day 137 of year. The middle panel shows the DST index, and 138 bottom panel shows the solar wind velocity. Figure 139 from (Reeves et al., 2003).	12
140 1.7 The three periodic motions of charged particles 141 in Earth's dipole magnetic field. These motions 142 are: gyration about the magnetic field line, bounce 143 motion between the magnetic poles, and azimuthal 144 drift around the Earth. Figure from (Baumjohann 145 and Treumann, 1997).	14

LIST OF FIGURES – CONTINUED

Figure	Page
146 1.8 Charged particle motion in a uniform magnetic field 147 \vec{B} . Panel (A) shows the geometry defining the 148 pitch angle, α . Panel (B) and (C) show two helical 149 electron trajectories with dashed lines assuming a 150 large and small α (corresponding to a small and large 151 parallel velocity $v_{ }$), respectively.	17
152 1.9 Contours of constant gyration, bounce, and drift 153 frequencies for electrons and protons in a dipole field. 154 Figure from Schulz and Lanzerotti (1974).	19
155 1.10 The trajectories of an electron and a right-hand cir- 156 cularly polarized wave during a cyclotron resonance. 157 The electron's $v_{ }$ and the wave's $k_{ }$ are in opposite 158 directions such that the wave's frequency is Doppler 159 shifted to a integer multiple of the electron cyclotron 160 frequency. Figure from (Tsurutani and Lakhina, 1997).	22
161 1.11 Various wave modes in the magnetosphere. Ultra 162 low frequency waves occur throught the magneto- 163 sphere. Chorus waves are typically observed in 164 the 0-12 midnight-dawn region. EMIC waves are 165 typically observed in the dusk MLT sector. Hiss 166 waves are observed inside the plasmasphere. Figure 167 from Millan and Thorne (2007).	24
168 1.12 An example train of microbursts observed by FIREBIRD- 169 II unit 4 on February 2nd, 2015. The colored curves 170 show the differential energy channel count rates in 171 five channels from ≈ 200 keV to 1 MeV and a sixth 172 integral energy channel with a 1 MeV threshold. The 173 x-axis labels show auxiliary information such as time 174 of observation and the spacecraft position in L, MLT, 175 latitude and longitude coordinates.....	27

LIST OF FIGURES – CONTINUED

Figure	Page
176 1.13 Distribution of > 1 MeV microburst occurrence 177 rates as a function of L and MLT. The three panels 178 show the microburst occurrence rate dependence on 179 geomagnetic activity, parameterized by the auroral 180 electrojet (AE) index for (a) AE < 100 nT, (b) 181 $100 < \text{AE} < 300$ nT and (c) AE > 300 nT. Figure 182 from Douma et al. (2017). ..	28
183 1.14 Three snapshots of a temporal microburst observed 184 simultaneously by a pair of polar-orbiting spacecraft. 185 The spacecraft are identified by labels "A" and 186 "B" and are traveling upwards on the blue dashed 187 orbital track. At T_1 the spacecraft are traveling 188 upwards and no microburst is observed. Then at T_2 189 both spacecraft simultaneously observe a microburst 190 shown by the red circle and the microburst size must 191 be greater than the spacecraft separation. In the last 192 snapshot, T_3 , the microburst has precipitated and no 193 longer observed by the spacecraft.	31

LIST OF FIGURES – CONTINUED

Figure	Page
194 2.1 Electron and wave conditions from the MagEIS-A 195 and EMFISIS WFR sensors for the microburst time 196 interval. Panels (a), (b), and (c) are from RBSP-A 197 with its position information annotated in panel (a). 198 Panels (d), (e), and (f) are from RBSP-B with its 199 position information annotated in panel (d). Panel 200 (a) is the MagEIS-A high rate timeseries. Panels (b) 201 and (e) show the evolution of the MagEIS-A J as a 202 function of α_L from the ~ 40 to ~ 60 keV channel. 203 Every 10th point is shown in panel (b). The solid 204 black line in panels (a) and (b) mark the end of 205 the time period used for the PSD fit extrapolation 206 analysis explained in section 3. The dashed black 207 lines in panels (a) and (b) show the time interval 208 used for the observed microburst PSD. Panels (c) 209 and (f) show the EMFISIS WFR spectra, with the 210 available burst data superposed. The red, green, and 211 cyan traces are equatorial f_{ce0} , $f_{ce0}/2$, and $f_{ce0}/10$, 212 respectively.	41
213 2.2 Panel (a) shows the MagEIS-A high rate timeseries. 214 Panel (b) shows the RBSPICE EBR count rate 215 timeseries for $\zeta 19$ keV electrons. The microbursts 216 were observed between 11:17:10 - 11:17:12 UT and 217 are indicated with the vertical black arrows in panels 218 (a) and (b) for MagEIS-A times. Panel (c) shows the 219 RBSPICE EBR (family of relatively sparse sampled 220 curves) and MagEIS-A J from the 29-41 keV energy 221 channel (single curve) as a function of α_L . The 222 vertical dashed lines show the time interval for the 223 PSD analysis.....	43

LIST OF FIGURES – CONTINUED

Figure	Page
224 2.3 The colored annulus represents $f(p_\perp, p_{\parallel})$ in normalized momentum space, parallel and perpendicular to the background magnetic field. The microburst $f(p_\perp, p_{\parallel})$ is highlighted with the white circle. The columns show different powers of the sine extrapolation, and rows show the different magnetic latitudes of the scattering. The white dotted traces represent the boundary between the data and extrapolation. The green, red, and white solid traces are the resonance curves for $\omega = 0.2\Omega_{ce}$, $0.4\Omega_{ce}$, $0.6\Omega_{ce}$, respectively. The cyan dashed traces are the diffusion curves for a $\omega = 0.4\Omega_{ce}$ wave (waves of other frequency have similar diffusion curves). The magnetic latitude of the scattering, the ratio of the plasma to the cyclotron frequency, and the power of the sine extrapolation is annotated in each panel. For the resonance and diffusion curves, the density model assumed a $n_L = 1 e^-/cm^3$ and $\psi = -1$	46
242 3.1 HiRes data of the microburst observed at February 2nd, 2015 at 06:12:53 UT, smoothed with a 150 ms rolling average. The subsequent bounces showed some energy dispersion. As discussed in Appendix B, a time correction of -2.28 s was applied to FU3. While the flux from five energy channels is shown, only channels with reasonable counting statistics were used for the spatial scale analysis. Vertical colored bars show the \sqrt{N} error every 10th data point and vertical black bars are lined up with the peaks in the 220-283 keV energy channel to help identify dispersion.	60

LIST OF FIGURES – CONTINUED

Figure	Page
254 3.2 Observed and theoretical t_b for electrons of energies 255 from 200 to 770 keV. The solid black line is t_b 256 in a dipole magnetic field, derived in Schulz and 257 Lanzerotti (1974). The red dotted and cyan dashed 258 lines are the t_b derived using the T89, and T04 259 magnetic field models with IRBEM-Lib. Lastly, 260 the blue dot-dash curve is the t_b derived using the 261 Olson & Pfitzer Quiet model. The green and purple 262 rectangles represent the observed t_b for FU3 and 263 FU4 using a Gaussian fit, respectively. The blue 264 rectangles represent the observed t_b calculated with 265 the minima between the bounces. The width of the 266 boxes represent the width of those energy channels, 267 and the height represents the uncertainty from the fit.....	63
268 3.3 The topology of the FIREBIRD-II orbit and the 269 multiple bounces of the microburst projected onto 270 latitude and longitude with axis scaled to equal 271 distance. Attributes relating to FU3 shown in red 272 dashed lines, and FU4 with blue solid lines. The 273 spacecraft path is shown with the diagonal lines, 274 starting at the upper right corner. The labels P1- 275 4 for FU4 and P1-5 for FU3 indicate where the 276 spacecraft were when the N^{th} peak was seen in 277 the lowest energy channel in the HiRes data. The 278 stars with the accompanying energy labels represent 279 the locations of the electrons with that energy that 280 started at time of P1, and were seen at the last peak 281 on each spacecraft. The rectangles represent the 282 lower bound of the microburst scale size, assuming 283 that the majority of the electrons were in the upper 284 boundary of energy channel 4.....	66
285 4.1 AC6 mission properties for (a) spacecraft separation 286 and (b) number of simultaneous quality 10 Hz 287 samples as a function of L and MLT.....	77

LIST OF FIGURES – CONTINUED

Figure	Page
288 4.2 Examples of > 35 keV microbursts observed simultaneously by AC6-A in red and AC6-B in blue. Panels 289 (a), (c), (e), and (g) show the temporally-aligned 290 time series when AC6 were separated by $s = 5$, 291 16, 37, and 69 km, respectively. The corresponding 292 panels (b), (d), (f), and (h) show the spatially- 293 aligned time series which is made by shifting the 294 AC6-A time series in the above panels by the in- 295 track lag (annotated with dt) that show any spatially 296 correlated structures. The clear temporal correla- 297 tion and lack of spatial correlation demonstrates that 298 these events are microbursts.	80
300 4.3 Microburst size distribution in low Earth orbit. 301 Panel (a) shows the percent of microbursts observed 302 above that separation after normalizing for the 303 uneven AC6 sampling in separation. Panel (b) shows 304 the microburst probability density (size histogram) 305 as a function of separation. Lastly, panel (c) shows 306 the normalization, i.e. number of simultaneous 307 samples AC6 observed as a function of separation. 308 The colored lines show the distributions binned by 309 L, and the thick black curve for the entire radiation 310 belt ($4 < L < 8$). The gray shading around the 311 black curve shows the uncertainty due to counting 312 statistics.	83
313 4.4 Microburst size distribution mapped to the magnetic 314 equator in the same format as Fig. 4.3.	84

LIST OF FIGURES – CONTINUED

Figure	Page
315 4.5 Panels A-C show the varying geometries of the 316 analytic model. The two spacecraft are shown 317 as black dots. The enclosing black circle around 318 each spacecraft bounds the area where a microburst 319 will be observed by one or both AC6 units if the 320 microburst's center lies inside the circle. Panel 321 (A) shows the case where microburst diameter is 322 smaller than the AC6 separation and all microbursts 323 will be observed by either unit A or B and never 324 simultaneously. Panel (B) shows the intermediate 325 case where the microburst diameter is comparable to 326 the AC6 separation and some fraction of microbursts 327 will be observed simultaneously. The fraction of the 328 microbursts simultaneously observed is proportional 329 to the circle intersection area $A(r, s)$ and is shown 330 with grey shading. Panel (C) shows the case where 331 the microburst diameter is much larger than the 332 spacecraft separation and nearly all microbursts will 333 be observed by both spacecraft. Lastly panel (D) 334 shows $\bar{F}(s)$ from the AC6 data with a solid black 335 line, and modeled MC and analytic $\bar{F}(s)$ curves for 336 a single-sized microburst distribution with $d = 40$ km.....	87
337 4.6 Range of plausible microburst sizes assuming all 338 microbursts are one fixed size. Panel (a) shows the 339 posterior probability density function of microburst 340 diameters in black. The red, green, and blue vertical 341 lines at 38, 73, and 129 km represent the 2.5, 50, and 342 97.5 posterior percentiles, respectively. A uniform 343 prior between 0 and 200 km was assumed for this 344 MCMC run and is shown in cyan. Panel (b) shows 345 the percent of microbursts observed above an AC6 346 separation for $4 < L < 8$ in black. The 2.5, 50 347 and 97.5 size percentiles were estimated from the 348 posterior and plotted in red, green, and blue curves, 349 respectively.....	92

LIST OF FIGURES – CONTINUED

Figure	Page
350 4.7 Plausible microburst percent curves assuming mi- 351 croburst size distribution is bimodal consisting of 352 two sizes d_0 and d_1 with a mixing term that quanti- 353 fies the relative occurrence of the d_0 to d_1 microburst 354 populations. Panel (a) shows the posterior distri- 355 bution for the microburst population mixing term, 356 a with a median value of 0.02. The a prior was 357 uniform between 0 and 0.2. Panel (b) shows the 358 posterior distribution for d_0 , the larger microburst 359 population estimated with a uniform prior between 360 50 and 200 km and the posterior median diameter of 361 122 km. Panel (c) shows the posterior distribution 362 for d_1 , the smaller microburst population, estimated 363 using a uniform prior between 0 and 50 km with a 364 median diameter of 28 km. Panel (d) is similar to 365 Fig. 4.6b and shows the AC6 microburst fraction for 366 $4 < L < 8$ in black. A set of 1000 random parameter 367 triples (a , d_0 , and d_1) were drawn from the posterior 368 and used to generate a family of $\bar{F}(s)$ curves. At 369 each s the range of consistent $\bar{F}(s)$ were quantified 370 by the 2.5, 50 and 97.5 percentiles and shown with 371 the red, green, and blue curves, respectively.	93
372 A.1 Panel (A) shows the magnetic power spectral density 373 as a function of frequency and time from the EMFI- 374 SIS WFR instrument on board RBSP-A. The “hiss- 375 like” wave used for the resonant diffusion analysis 376 was observed starting at 11:17:03 UT. In the same 377 format as panel (A), panel (B) shows the polar angle 378 of the wave vector for this time period. The wave 379 of interest had a normal wave vector, $\theta_k < 30^\circ$. 380 Since the results in panel (B) are valid only for high 381 planarity, panel (C) shows planarity in the same 382 format as panels (A) and (B). The wave of interest 383 was found to have a planarity of > 0.8 . Lastly, panel 384 (D) shows the available burst mode data.	114

LIST OF FIGURES – CONTINUED

Figure	Page
385 A.2 Ratio of the RBSPICE EBR at microburst times 386 indicated with the black vertical arrows in Fig. 2, 387 to the EBR at the same pitch angles one spin prior 388 (quiet time). The microburst flux was enhanced by 389 10-80% across $100^\circ < \alpha_L < 160^\circ$ PA, and appear to 390 be peaked closer to $\alpha_L = 90^\circ$	115
391 B.1 Cross-correlation time lag analysis applied to a train 392 of microbursts. Panel (a) and (b) show the count 393 rate from the lowest energy channel. Panel (c) shows 394 the cross-correlation coefficient as a function of time 395 lag. Panel (d) shows the shifted timeseries. Clock 396 difference was 2.23 s	118
397 B.2 Same analysis as Fig. B.1 on a different time period. 398 Clock difference was 2.21 s.....	119
399 B.3 Same analysis as Fig. B.1 on a different time period. 400 Clock difference was 2.25 s.....	120
401 B.4 Same analysis as Fig. B.1 on a different time period. 402 Clock difference was 2.27 s.....	121
403 B.5 Same cross-correlation time lag analysis applied to 404 stationary spatial structures. The cross-correlation 405 lag between these events is a sum of the clock differ- 406 ence and time lag due to the spacecraft separation. 407 The lag derived at this time was 4.95 s	122
408 B.6 Same analysis as Fig. B.5 applied to a different 409 stationary spatial feature. The lag derived at this 410 time was 5.01 s	123

NOMENCLATURE

L	L-Shell
MLT	magnetic local time
λ	magnetic latitude
α	pitch angle
α_L	local pitch angle at the spacecraft
α_{eq}	pitch angle maped to the magnetic equator
c	speed of light
R_E	Earth's radius
J	flux
f	phase space density
E	energy
E_0	exponential e-folding energy
p	momentum
\vec{E}	electric field
\vec{B}	magnetic field
B_w	wave amplitude
v	velocity
Ω_e	electron gyrofrequency
ω_{pe}	plasma frequency
k	wave vector
D_{xx}	diffusion coefficient
s	spacecraft separation
t_b	electron bounce period

411

412

INTRODUCTION

413 Above Earth's atmosphere are the Van Allen radiation belts, a toroidally-shaped
414 pair of belts that consist of a complex and dynamic plasma environment. The inner
415 radiation belt is stable, consists of mostly energetic protons, and is located within 2
416 Earth radii (measured near the equator) above Earth's surface. The outer radiation
417 belt, on the other hand, consists of mostly energetic electrons, is dynamic on hour
418 time scales, and is typically found between three and eight Earth radii above Earth's
419 surface. These belts pose a threat to space exploration due to their adverse effects on
420 our bodies and electrical components. A few effects include: a high radiation dose for
421 manned missions, degradation of silicon that causes transistor malfunction, computer
422 memory corruption due to bit flips, etc. With these effects in mind, it is no surprise
423 that the radiation belts have been extensively studied since their discovery in the
424 1960s.

425 The radiation belt particles, mostly consisting of electrons and protons, are at
426 times unstable to wave growth and generate electric and magnetic waves. These waves
427 can then accelerate and scatter radiation belt particles with a variety of wave-particle
428 mechanisms. These wave-particle interactions are believed to be responsible for
429 scattering electron microbursts—a short and intense increase of precipitating electrons
430 into Earth's atmosphere—that are capable of destroying ozone molecules and rapidly
431 deplete the outer belt's electrons.

432 Electron microbursts, henceforth referred to as microbursts, are typically
433 observed by low Earth orbiting spacecraft, sounding rockets, and high altitude
434 balloons as a sub-second impulse of electrons. Some of the most intense microbursts

435 have electron fluxes that are a factor of 10 to 100 above the background (for example
436 see Fig. 7 in Blake et al. (1996)). Since they were first reported by Anderson and
437 Milton (1964), the intense transient nature of microbursts have compelled researchers
438 to pursue an understanding of their properties, their effects on the environment, and
439 the physical mechanism(s) that create microbursts. Microbursts are widely believed
440 to be created by wave-particle scattering between a plasma wave called whistler
441 mode chorus and outer radiation belt electrons, although many details regarding the
442 scattering mechanism are unconstrained or unknown. The goal of this dissertation
443 is to expand our knowledge of the wave-particle scattering mechanism that causes
444 electron microbursts.

445 This chapter serves as an introduction to the fundamental physical concepts
446 that are essential to understand wave-particle interactions in Earth's magnetosphere.
447 We will review the main structures in the magnetosphere, the motion of charged
448 particles in electric and magnetic fields, how particles are accelerated and lost in the
449 magnetosphere, and asses the current state of our understanding of microbursts.

450 Then the rest of this dissertation expands our knowledge of microbursts. In
451 Chapter 2 (chapter numbers will be filled in the full dissertation) we will investigate
452 and model the scattering mechanism responsible for microbursts observed inside the
453 outer radiation belt, near the magnetic equator. Then in Chapters 3 and 4 we
454 will investigate the microburst scattering mechanism indirectly by estimating the
455 microburst footprint size in low Earth orbit and the magnetic equator (near where
456 microburst electrons are believed to be scattered) and compare it to sizes of chorus
457 waves estimated in prior literature.

458 Particle Populations and Their Interractions in the Magnetosphere

459 To set the scene, we will briefly tour the various populations in the magneto-
460 sphere that are most relevant to this dissertation, and are illustrated in Fig. 1.1.

461 The sun and its solar wind are ultimately the source of energy input into the
462 magnetosphere. The solar wind at Earth's orbit is a plasma traveling at supersonic
463 speeds with an embedded interplanetary magnetic field (IMF). When the solar
464 wind encounters Earth's magnetic field, the plasma can not easily penetrate into
465 the magnetosphere. The plasma can not easily penetrate into the magnetosphere
466 because it is frozen-in on the magnetic field lines because plasma has a nearly
467 infinite conductivity. Thus the plasma and its magnetic field drapes around the
468 magnetosphere, forming a cavity in the solar wind that qualitatively has a shape
469 similar to in Fig. 1.1. The solar wind is supersonic at 1 AU so a bow shock
470 exists upstream of the magnetosphere which compresses and heats the solar wind.
471 Downstream of the bow shock, the solar wind plasma flows around the magnetosphere
472 inside the magnetosheath. The magnetopause is the surface where the solar wind
473 ram and Earth's magnetic pressures balance. To first order, the magnetopause can
474 be thought of as a boundary between the solar wind and Earth's magnetosphere.
475 The shocked plasma then flows past the Earth where it shapes the magnetotail. In
476 the magnetotail, the magnetopause exists where the solar wind magnetic pressure
477 balances Earth's magnetic field pressure in the lobes. The magnetotail extends on
478 the order of 100 R_E downstream of Earth, and the tailward stretching of magnetic
479 field lines creates a region where Earth's earthward and anti-earthward magnetic fields
480 are in proximity. In this region, the curl of \vec{B} is non-zero, thus by Ampere's law there
481 must be a current (called the plasma sheet) near the magnetic equator (e.g. Eastwood
482 et al., 2015).

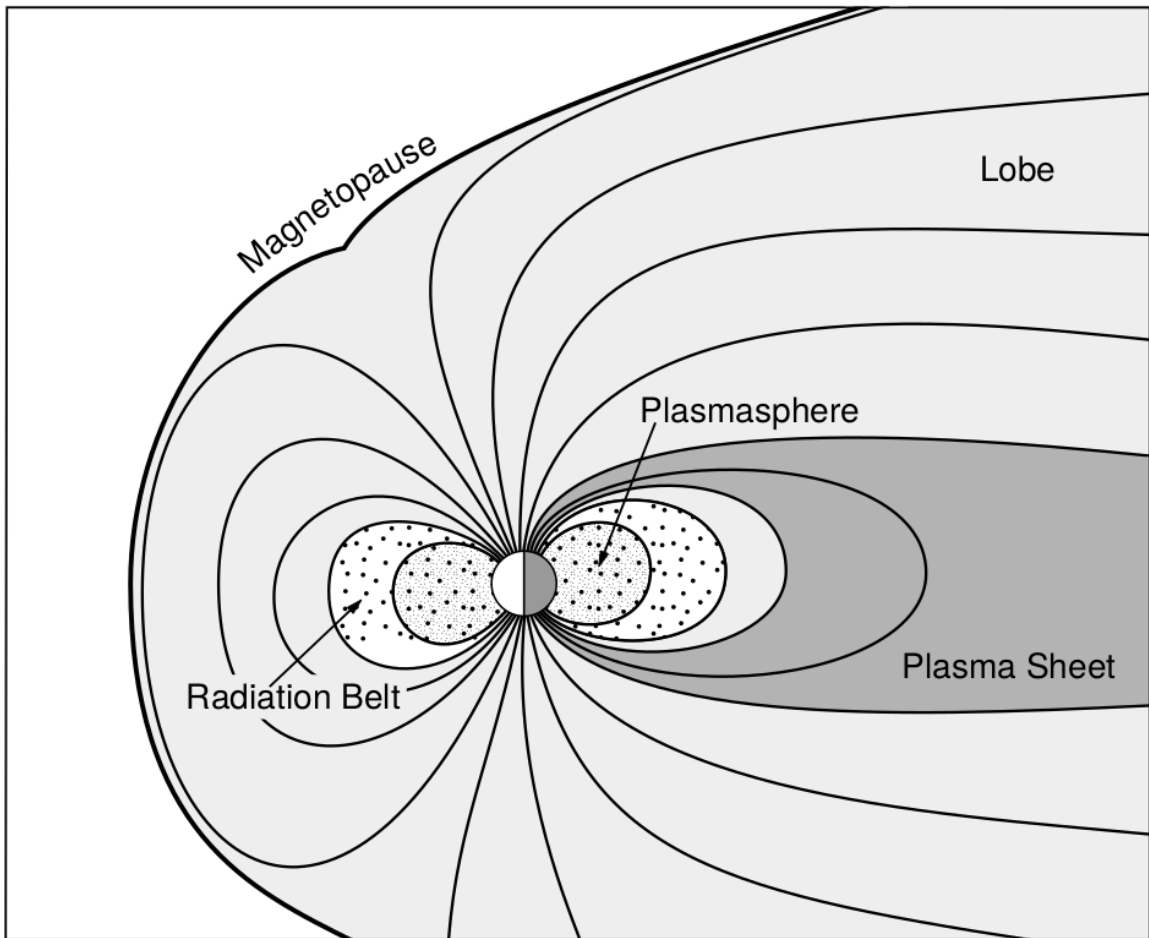


Figure 1.1: A few macroscopic structures in the magnetosphere. The magnetosphere boundary with the solar wind is the magnetopause. The magnetotail consists of two lobes that contain Earth's magnetic flux with the plasma sheet separating the two lobes. The inner magnetosphere contains the plasmasphere, the ring current, and the radiation belts which are co-located. Figure from Baumjohann and Treumann (1997).

483 Populations in the Inner Magnetosphere

484 Closer to Earth, where the magnetic field is largely dipolar, are three plasma
 485 populations that comprise the inner magnetosphere: the plasmasphere, the ring
 486 current, and the radiation belts which are shown in Fig. 1.1. Before we describe
 487 these three particle populations in detail, we will introduce the coordinate system
 488 that most naturally describes the inner magnetosphere environment, and the electric
 489 fields that mostly effect low energy particles.

490 This coordinate system is shown in Fig. 1.2 and it naturally describes particles
 491 in a dipole magnetic field geometry. In this coordinate system the “radial” coordinate
 492 is the L shell. The L -shell (L) is the distance from the Earth’s center to the location
 493 where a particular magnetic field line crosses the magnetic equator, in units of
 494 Earth radii, $R_e = 6,371$ km. The azimuthal coordinate is the magnetic local time
 495 (MLT). For an observer above Earth’s north pole looking down, MLT is defined to
 496 be 0 (midnight) in the anti-sunward direction and increases in the counter-clockwise
 497 direction with 6 at dawn, 12 at noon (sunward direction), and 18 at dusk. The final
 498 coordinate is the magnetic latitude, λ , which is analogous to the latitude coordinate in
 499 the spherical coordinate system and is defined to be 0 at the magnetic equator. This
 500 coordinate system naturally describes the inner magnetosphere populations described
 501 below.

502 Low energy particle dynamics in the inner magnetosphere are driven by the
 503 co-rotation and the dawn-dusk (pointing from approximately 6 to 18 MLT) electric
 504 fields. The co-rotation electric field arises from Earth’s rotation. Earth’s magnetic
 505 field and the particles frozen on it rotate with the Earth so in the magnetosphere (non-
 506 rotating) reference frame the particles appear to $\vec{E} \times \vec{B}$ drift (which will be described
 507 in the next section) with Earth’s rotation. The co-rotation \vec{E} points towards Earth.
 508 The convection electric field points from dawn to dusk, and is due to the Earthward

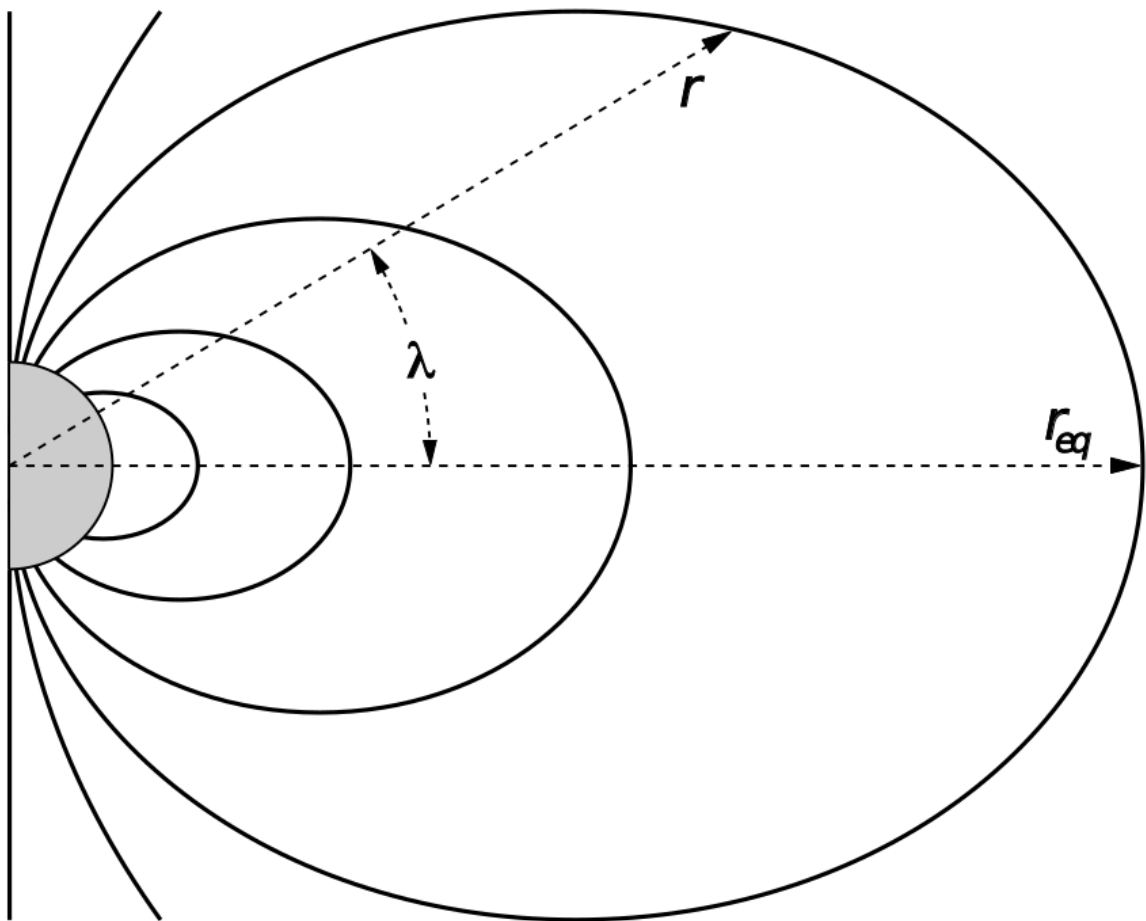


Figure 1.2: The dipole coordinate system. The magnetic latitude of \mathbf{r} is λ . The radial distance to a magnetic field line in the equatorial plane is typically given by $L = r_{eq}/R_e$. Figure from Baumjohann and Treumann (1997).

509 transport of particles from the magnetotail. The superposition of the co-rotation
 510 and convection electric fields is a potential field shown in Fig. 1.3. The shaded
 511 area in Fig. 1.3 shows where low energy electrons execute closed orbits around Earth
 512 (i.e. particles are trapped), and outside this region the electrons are not trapped. The
 513 dynamic topology of the shaded region in Fig. 1.3 is controlled by only the convection
 514 electric field which is dependent on the solar wind speed and the IMF. The lowest
 515 energy particles that orbit along equipotential lines in the shaded region in Fig. 1.3
 516 make up the plasmasphere.

517 Plasmasphere The plasmasphere is a relatively dense ($n_e \sim 10^3/\text{cm}^3$) and cool
 518 ($\sim \text{eV}$) plasma. The plasmasphere typically extends to $L \sim 4$ and the spatial extent
 519 is highly dependent on the solar wind and magnetospheric conditions. The source
 520 of the plasmasphere is the ionosphere, a layer in Earth's upper atmosphere that
 521 contains a high concentration of electrons and ions. The main mechanisms that
 522 ionize the ionosphere are ultraviolet light from the sun and particle precipitation.
 523 The ultraviolet ionization by sunlight is strongly dependent on the time of day
 524 and latitude, while particle precipitation is highly dependent on magnetospheric
 525 conditions and mostly occurs at high latitudes.

526 The outer boundary of the plasmasphere is called the plasmapause which is
 527 typically identified by a steep radial gradient in plasma density from $\sim 10^3/\text{cm}^3$ to
 528 $\sim 1/\text{cm}^3$. It is important to know the location of the plasmapause since the plasma
 529 density strongly controls the efficiency of particle scattering by waves. For example,
 530 electron scattering by chorus waves is more efficient when the ratio of the plasma and
 531 gyro frequency is low which is typically found in low plasma density regions outside
 532 of the plasmapause (e.g. Horne et al., 2005; O'Brien and Moldwin, 2003; ?).

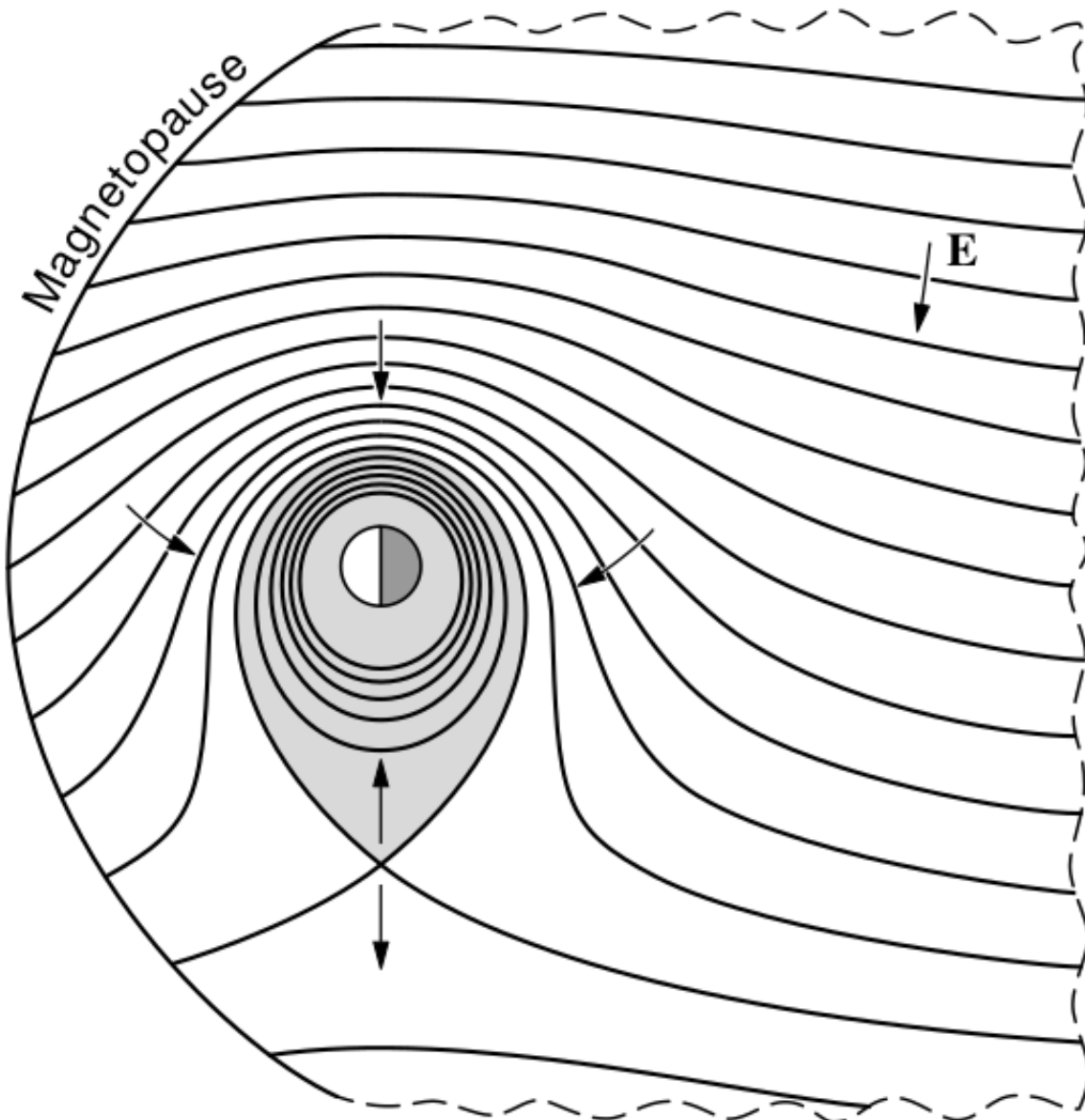


Figure 1.3: Equipotential lines and electric field arrows due to the superposition of the co-rotation and convection electric fields. Electrons in the shaded region execute closed orbits. Outside of the shaded regions the electrons are not trapped and will escape. The region separating the two regimes is called the Alfvén layer. Figure from Baumjohann and Treumann (1997).

533 Ring Current A higher energy population is the ring current. This population
534 consists of protons and electrons between tens and a few hundred keV that drift
535 around the Earth. The orbits of higher energy particles are not as affected by the
536 convection and co-rotation electric field, instead they drift around the Earth due to
537 gradient and curvature drifts which will be described in the following section. Since
538 the direction of the drift is dependent on charge, protons drift west around the Earth
539 and electrons drift East. This effect creates a current around the Earth.

540 The ring current generates a magnetic field which decreases the magnetic field
541 strength at the surface of the Earth and increases it outside of the ring current. The
542 decrease of Earth's magnetic field strength is readily observed by a system of ground-
543 based magnetometers and is merged into a Disturbance Storm Time (DST) index
544 to quantify the global reduction in the magnetic field. An example of a DST index
545 time series from the 2015 St. Patrick's Day storm, driven by a coronal mass ejection
546 (CME), is shown in Fig. 1.4. At the start of a storm, DST sometimes increases in
547 response to the compression of the magnetopause by a shock wave (termed the initial
548 phase or sudden storm commencement) and is shown by the red horizontal bar in Fig.
549 1.4. During the main phase of the storm the ring current population is rapidly built
550 up and DST rapidly decreases which is shown by the green bar in Fig. 1.4. After
551 the storm is over, the ring current slowly recovers to pre-storm conditions during the
552 recovery phase shown by the blue bar in Fig. 1.4. In the recovery phase, the ring
553 current gradually decays due to particles losses into the atmosphere, or transport
554 through the magnetopause via mechanisms described later in this chapter. The DST
555 index, along with other geomagnetic indices, are used by the space physics community
556 to quantify the global state of the magnetosphere.

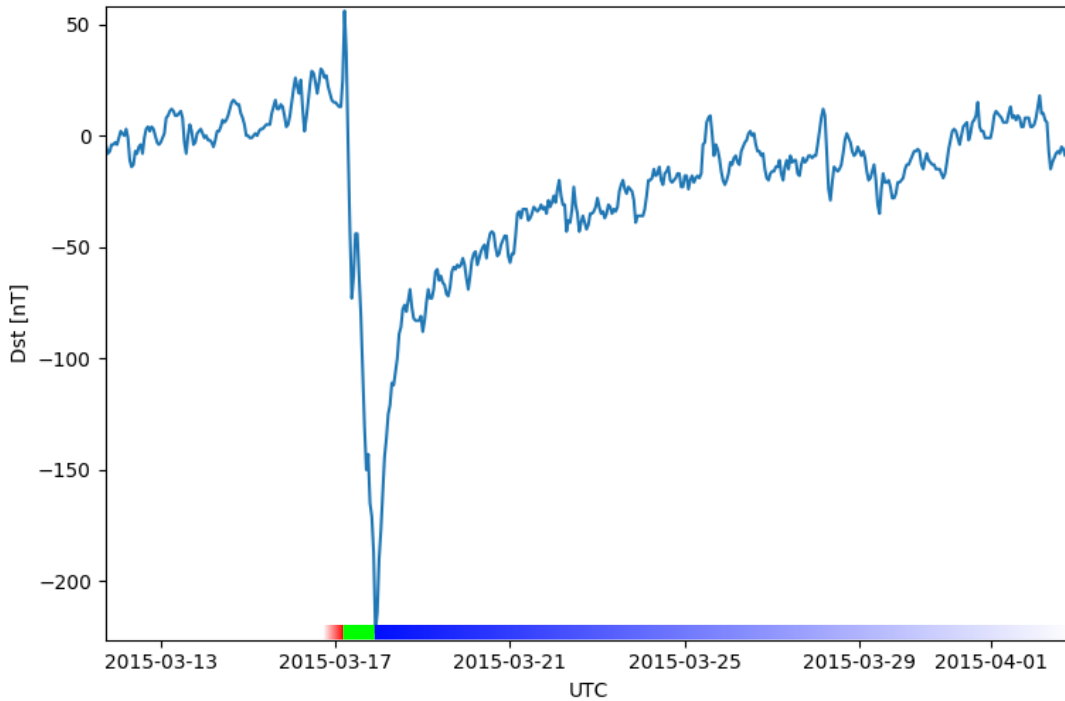


Figure 1.4: The DST index during the St. Patrick's Day 2015 storm. This storm was caused by a coronal mass ejection on March 15th, 2015. The storm phases are: initial phase, main phase, and recovery phase. The initial phase occurred when the Dst peaked at $+50$ nT on March 17th during which the ring current was eroded by the coronal mass ejection during the interval shown by the red bar shown at the bottom. Then the following rapid decrease to ≈ -200 nT was during the main phase where many injections from the magnetotail enhanced the ring current, which reduced Earth's magnetic field strength at the ground, and is shown with the green bar. Lastly, the recovery phase lasted from March 18th to approximately March 29th during which the ring current particles were lost and the ring current returned to its equilibrium state. The recovery phase is shown with the blue bar.

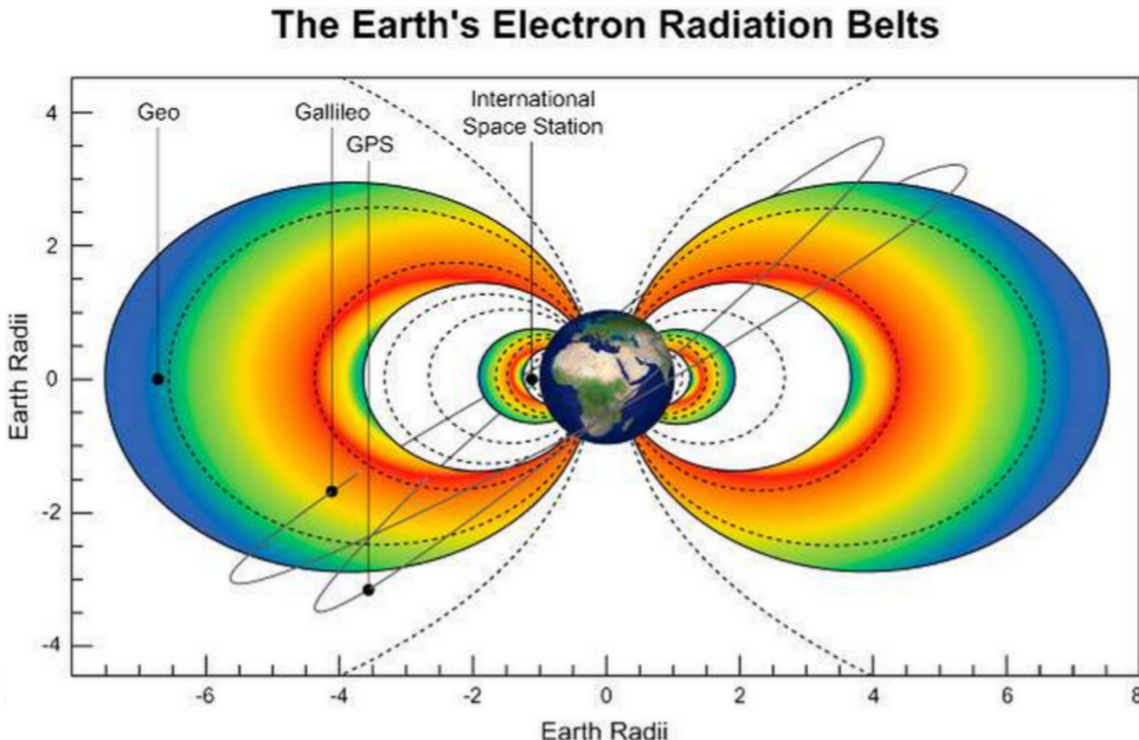


Figure 1.5: The two radiation belts with the locations of various satellites and orbits. Figure from (Horne et al., 2013).

557 Radiation Belts The highest particle energy populations are in the Van Allen
 558 radiation belts. These belts were discovered by Van Allen (1959) and Vernov and
 559 Chudakov (1960) during the Cold War and are a pair of toroidally shaped populations
 560 of trapped electrons and protons shown in Fig. 1.5. Their quiescent toroidal shape,
 561 similar to the shape of the plasmasphere and ring current, is a result of Earth's dipole
 562 magnetic field.

563 The inner radiation belt is extremely stable on year time periods, extends to
 564 $L \approx 3$, and mainly consists of protons with energies between MeV and GeV and
 565 electrons with energies up to ≈ 1 MeV (Claudepierre et al., 2019). The source of
 566 inner radiation belt protons is believed to be due to cosmic-ray albedo neutron decay
 567 (e.g. Li et al., 2017) and inward radial diffusion for electrons (e.g. O'Brien et al.,

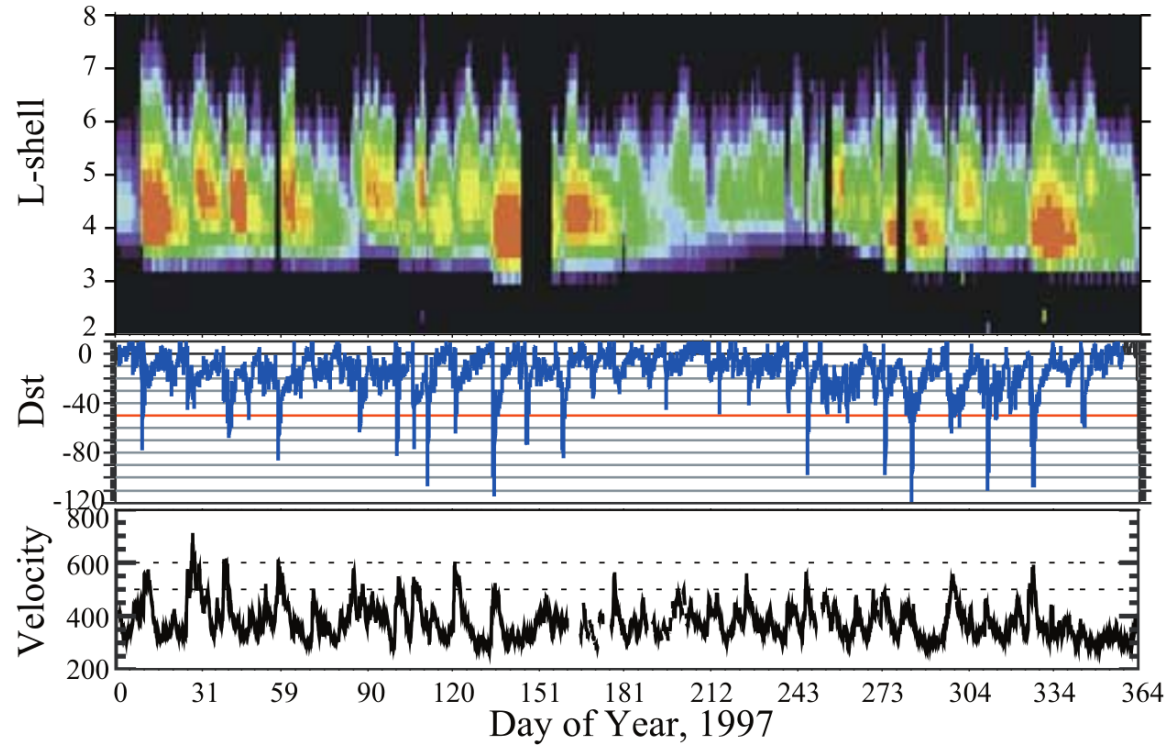


Figure 1.6: The dynamics of the outer radiation belt in 1997 from the POLAR satellite. Top panel shows the 1.2-2.4 MeV electron flux as a function of L and 1997 day of year. The middle panel shows the DST index, and bottom panel shows the solar wind velocity. Figure from (Reeves et al., 2003).

568 2016a). The gap between the inner and outer radiation belt is called the slot, which is
 569 believed to be due to hiss waves inside the plasmasphere (described below) scattering
 570 particles into the atmosphere (e.g. Breneman et al., 2015; Lyons and Thorne, 1973).

571 The outer radiation belt is much more dynamic and consists of mainly electrons
 572 of energies up to a few MeV. The outer belt's spatial extent is highly variable as
 573 shown in Fig. 1.6, and is typically observed between L of 4 and 8. The source of
 574 outer radiation belt electrons is widely believed to be injections of plasma from the
 575 magnetotail that is then accelerated to high energies.

576

Charged Particle Motion in Electric and Magnetic Fields

A charged particle trapped in the magnetosphere will experience three types of periodic motion in Earth's nearly dipolar magnetic field in the absence of electric fields. The three motions are ultimately due to the Lorentz force that a particle of momentum \vec{p} , charge q , and velocity \vec{v} experiences in an electric field \vec{E} and magnetic field \vec{B} and is given by

$$\frac{d\vec{p}}{dt} = q(\vec{E} + \vec{v} \times \vec{B}). \quad (1.1)$$

577 For many vector quantities in this dissertation, we will adopt a widely-used
 578 convention by splitting up vectors into parallel, $x_{||}$, and perpendicular, x_{\perp} components
 579 with respect to the background magnetic field. In the magnetosphere, the three
 580 periodic motions, in decreasing frequency, are gyration, bounce, and drift and are
 581 schematically shown in Fig. 1.7. Each periodic motion has a corresponding conserved
 582 quantity or adiabatic invariant.

The highest frequency periodic motion is gyration about a magnetic field of

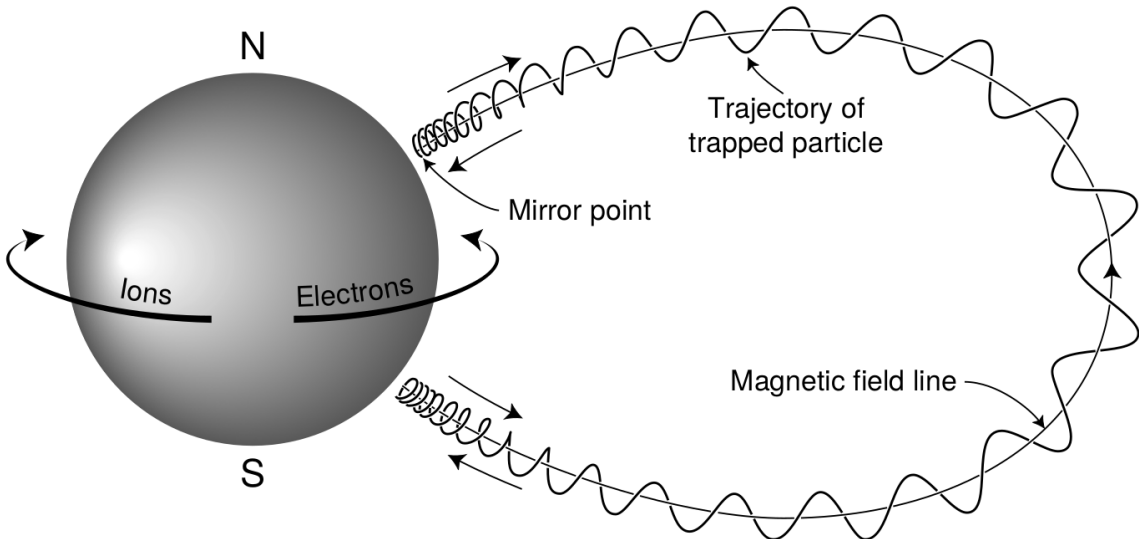


Figure 1.7: The three periodic motions of charged particles in Earth's dipole magnetic field. These motions are: gyration about the magnetic field line, bounce motion between the magnetic poles, and azimuthal drift around the Earth. Figure from (Baumjohann and Treumann, 1997).

magnitude B . This motion is circular with a Larmor radius of

$$r = \frac{mv_{\perp}}{|q|B} \quad (1.2)$$

where m is the mass and v_{\perp} the particle's velocity perpendicular to \vec{B} . This motion has a corresponding gyrofrequency of

$$\Omega = \frac{|q|B}{m} \quad (1.3)$$

in units of radians/second. In the radiation belts, the electron gyrofrequency, Ω_e , is on the order of a kHz near the magnetic equator. The corresponding adiabatic invariant is found by integrating the particle's canonical momentum around the particle's path of gyration,

$$J_i = \oint (\vec{p} + q\vec{A}) \cdot d\vec{l} \quad (1.4)$$

583 where J_i is the i^{th} adiabatic invariant and \vec{A} is the magnetic vector potential. This
 584 integral is carried out by integrating the first term over the circumference of the
 585 gyro orbit and integrating the second term using Stokes theorem to calculate the
 586 magnetic flux enclosed by the gyro orbit. The gyration invariant is $J_1 \sim v_\perp^2/B$ which
 587 is conserved when the frequency, ω , of a force acting on the gyrating electron satisfies
 588 $\omega \ll \Omega_e$.

589 The second highest frequency periodic motion is bouncing due to a parallel
 590 gradient in \vec{B} . This periodic motion naturally arises in the magnetosphere because
 591 Earth's magnetic field is stronger near the poles. To understand this motion we first
 592 we need to define the concept of pitch angle, α as the angle between \vec{B} and \vec{v} which
 593 is schematically shown in Fig. 1.8a. The pitch angle relates v with v_\perp and v_\parallel , the
 594 component of the particles velocity parallel to \vec{B} . As shown in Fig. 1.8b and 1.8c,
 595 a smaller (larger) α will increase (decrease) the distance that the charged particle
 596 travels parallel to \vec{B} during one gyration.

Assuming the particle's kinetic energy is conserved, the conservation of J_1
 implies that given a particle's $v_\perp(0)$ and $B(0)$ at the magnetic equator (where
 Earth's magnetic field is usually at a minimum) we can calculate its $v_\perp(s)$ along
 the particle's path, s , by calculating $B(s)$ from magnetic field models. Thus the
 particle's perpendicular velocity is then related via

$$\frac{v_\perp^2(0)}{B(0)} = \frac{v_\perp^2(s)}{B(s)} \quad (1.5)$$

597 which can be rewritten as

$$\frac{v^2 \sin^2 \alpha(0)}{B(0)} = \frac{v^2 - v_\parallel^2(s)}{B(s)} \quad (1.6)$$

⁵⁹⁸ and re-arranged to solve for $v_{||}(s)$ by

$$v_{||}(s) = v \sqrt{1 - \frac{B(s)}{B(0)} \sin^2 \alpha(0)} \quad (1.7)$$

⁵⁹⁹ which will tend towards 0 as the second term in the radical approaches 1.

⁶⁰⁰ The location where $v_{||}(s) = 0$ is called the mirror point and is where a particle
⁶⁰¹ stops and reverses direction. Since Earth's magnetic field is stronger towards both
⁶⁰² poles, the mirroring particle will execute periodic bounce motion between two mirror
⁶⁰³ points in the northern and southern hemispheres. The corresponding adiabatic
⁶⁰⁴ invariant, J_2 is

$$J_2 = \oint p_{||} ds \quad (1.8)$$

where ds describes the particle path between the mirror points in the northern and southern hemispheres (see Fig. 1.7). J_2 is found by substituting Eq. 1.7 into Eq. 1.8 and defining the magnetic field strength at the mirror points as B_m (where $\alpha(m) = 90^\circ$). The J_2 integral can be written as

$$J_2 = 2p \int_{m_n}^{m_s} \sqrt{1 - \frac{B(s)}{B(m)}} ds \quad (1.9)$$

⁶⁰⁵ where m_n and m_s are the northern and southern mirror points, respectively. The
⁶⁰⁶ bounce period can be estimated (e.g. Baumjohann and Treumann, 1997) to be

$$t_b \approx \frac{LR_e}{\sqrt{W/m}} (3.7 - 1.6 \sin \alpha(0)) \quad (1.10)$$

⁶⁰⁷ where W is the particle's kinetic energy. As with gyration, the particle will bounce
⁶⁰⁸ between the mirror points as long as $\omega \ll \Omega_b$, where Ω_b is the bounce frequency.

⁶⁰⁹ At this stage it is instructional to introduce loss cone pitch angle, α_L .

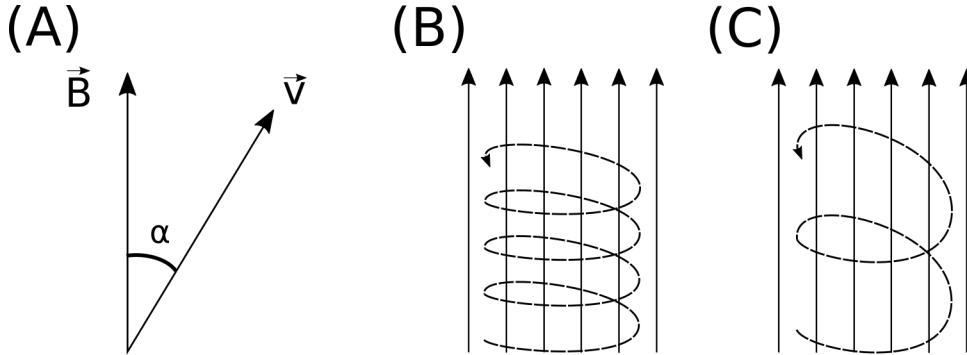


Figure 1.8: Charged particle motion in a uniform magnetic field \vec{B} . Panel (A) shows the geometry defining the pitch angle, α . Panel (B) and (C) show two helical electron trajectories with dashed lines assuming a large and small α (corresponding to a small and large parallel velocity $v_{||}$), respectively.

610 Conventionally, the loss cone pitch angle is defined as the pitch angle where a particle
 611 will mirror at ≈ 100 km altitude in the atmosphere. A charged particle gyrating at
 612 those altitudes will encounter, and likely Coulomb scatter, with the dense atmosphere
 613 and be lost. The 100 km altitude is only a convention and not a hard boundary, e.g.
 614 the peak in the 1 MeV electron ionization rate is at ≈ 60 km altitudes (Fang et al.,
 615 2010).

616 The slowest periodic motion experienced by charged particles in Earth's
 617 magnetic field is azimuthal drift around the Earth. This drift primarily results from
 618 a combination of a radial gradient in \vec{B} and the curvature of the magnetic field. The
 619 radial gradient drift arises because Earth's magnetic field is stronger near the Earth.
 620 The particle's gyroradius shrinks as it gyrates towards Earth, and expands when it
 621 gyrates away from Earth. The overall effect is the particle gyro orbit does not close
 622 on itself causing eastward drift of negatively charged particles and westward drift
 623 of positively charged particles. The radial gradient drift is further enhanced by the
 624 centrifugal force that a particle experiences as it bounces along the curved field lines.
 625 The drift adiabatic invariant, J_3 is found by integrating Eq. 1.4 over the complete

626 particle orbit around the Earth. The shape of this drift orbit is known as a drift shell,
 627 and can be visualized by rotating the trapped particle trajectory in Fig. 1.7 around
 628 the axis that connects the poles. For J_3 , the first term is negligible and the second
 629 term is the magnetic flux enclosed by the drift shell, Φ_m i.e. $J_3 \sim \Phi_m$.

630 To quantify the frequencies of the three periodic motions, Fig. 1.9 from Schulz
 631 and Lanzerotti (1974) shows contours of the gyration, bounce, and drift frequencies
 632 for electrons and protons in Earth's dipole magnetic field.

Up until now we have considered the three periodic motions due Earth's magnetic field in the absence of electric fields. If there is an electric field, \vec{E} , perpendicular to \vec{B} , a particle's center of gyration (averaged position of the particle over a gyration) will drift with a velocity perpendicular to both \vec{E} and \vec{B} . The drift velocity can be solved using Eq. 1.1 and is

$$\vec{v}_E = \frac{\vec{E} \times \vec{B}}{B^2}. \quad (1.1)$$

633 If there is a parallel magnetic field, $E_{||}$, then the particle is accelerated along the
 634 magnetic field line. An $E_{||}$ pointing away from the Earth will contribute to the mirror
 635 force and raise the particle's mirror point. On the contrary, an Earthward pointing
 636 $E_{||}$ will oppose the mirror force and lower the mirror point. If the Earthward $E_{||}$
 637 lowers the mirror point into the atmosphere, those particles will precipitate into the
 638 atmosphere. This is the mechanism that generates the aurora.

639

Radiation Belt Particle Sources and Sinks

640 Due to the highly energetic and dynamic nature of the radiation belts, and
 641 their impact on space exploration, the radiation belts have been studied for over
 642 half a century. Researchers have studied and attempted to predict the dynamics of
 643 radiation belt particles, waves, and wave-particle interactions by considering various

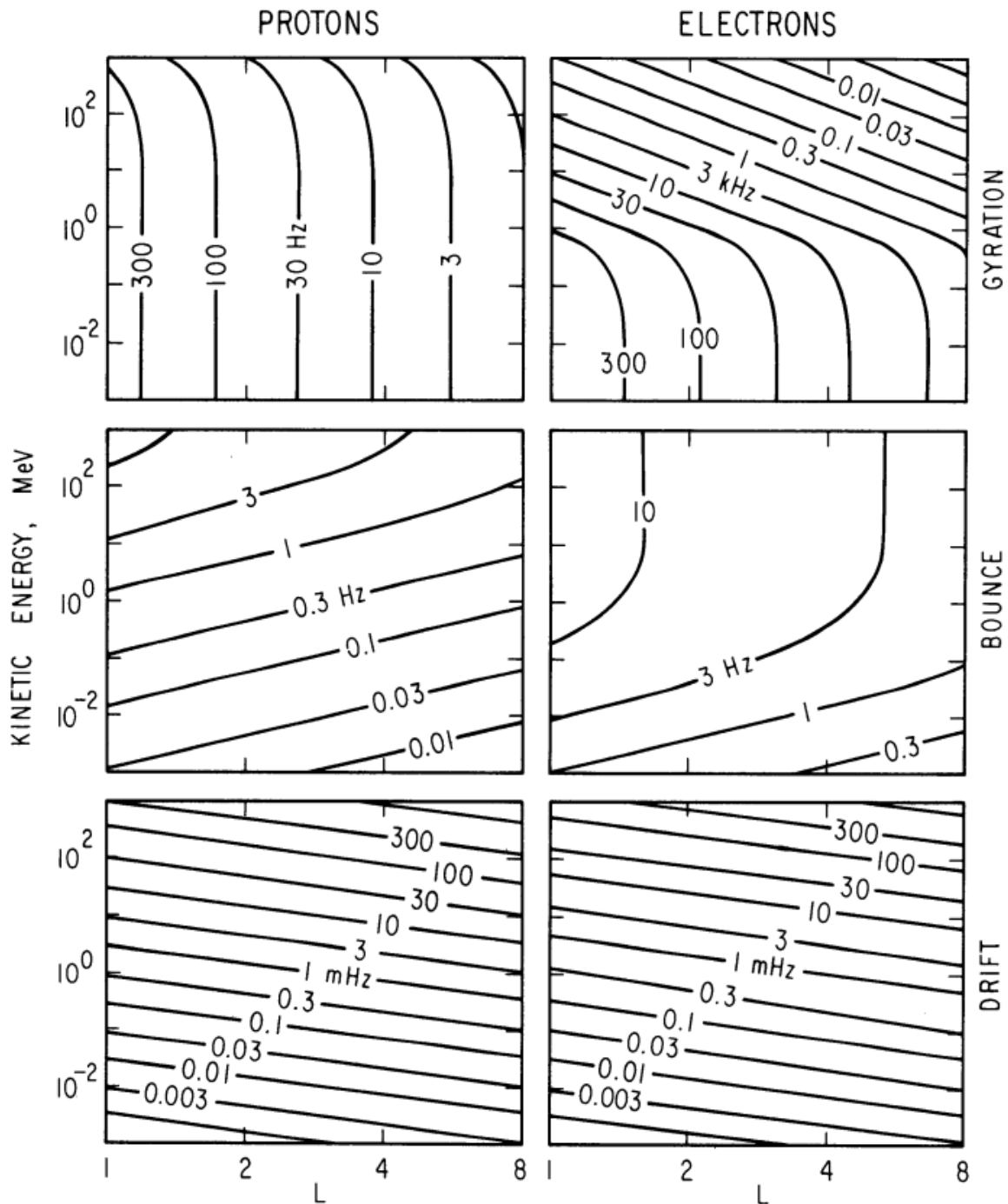


Figure 1.9: Contours of constant gyration, bounce, and drift frequencies for electrons and protons in a dipole field. Figure from Schulz and Lanzerotti (1974).

644 competing particle acceleration and loss mechanisms which are described below.

645 Adiabatic Heating

One of the particle heating and transport mechanisms arises from the earthward convection of particles. As shown in Eq. 1.5, the conservation of J_1 implies that the initial and final v_\perp depends on the change in the magnetic field magnitude. As a particle convects earthward $B_f > B_i$ and thus v_\perp must also increase. The dipole magnetic field magnitude falls off radially as $B \sim L^{-3}$, and the change in v_\perp^2 as the particle convects towards a stronger magnetic field is

$$\frac{v_{\perp f}^2}{v_{\perp i}^2} = \left(\frac{L_i}{L_f} \right)^3. \quad (1.12)$$

646 For a particle convecting earthward, if J_2 is conserved, its v_\parallel also increases because
 647 the distance between the particle's mirror points decreases. Calculating the increase
 648 in v_\parallel is somewhat difficult and is approximately

$$\frac{v_{\parallel f}^2}{v_{\parallel i}^2} = \left(\frac{L_i}{L_f} \right)^k \quad (1.13)$$

649 where k ranges from 2 for equatorial pitch angles, $\alpha_{eq} = 0^\circ$, to 2.5 for $\alpha_{eq} = 90^\circ$
 650 (Baumjohann and Treumann, 1997). Since the rate of adiabatic heating is greater in
 651 the perpendicular direction than heating in the parallel direction, an initially isotropic
 652 particle distribution will become anisotropic during its convection. These isotropic
 653 particles can then become unstable to wave growth and generate waves in order to
 654 reach equilibrium.

655 Wave Resonance Heating

656 Another mechanism that heats particles is caused by particles resonating with
 657 plasma waves. A few of the electromagnetic wave modes responsible for particle

658 acceleration (and scattering) relevant to radiation belt dynamics are hiss, whistler
 659 mode chorus (chorus), and electromagnetic ion cyclotron (EMIC) waves. These waves
 660 are created by the loss cone instability that is driven by an anisotropy of electrons for
 661 chorus waves, and protons for EMIC waves. The level of anisotropy can be quantified
 662 by the ratio of the perpendicular to parallel particle temperatures (T_{\perp}/T_{\parallel}). A particle
 663 distribution is unstable when $T_{\perp}/T_{\parallel} > 1$. Since electrons gyrate in a right-handed
 664 sense, the chorus waves also tend to be right hand circularly polarized (Tsurutani and
 665 Lakhina, 1997). The same argument also applies to protons and left hand circularly
 666 polarized EMIC waves.

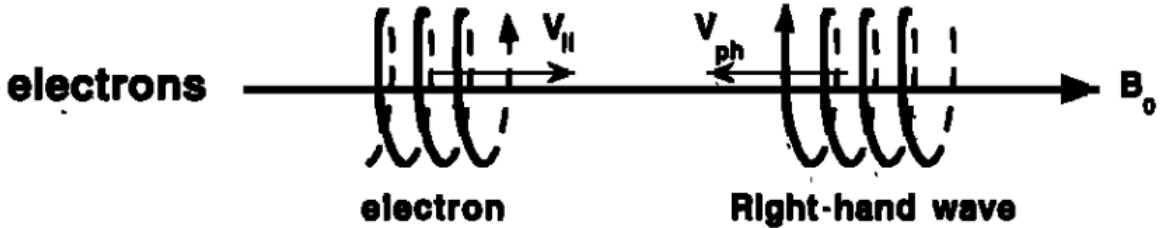
667 These circularly polarized waves can resonate with electrons and/or protons
 668 when their relative motion results in a static \vec{E} in the particle's reference frame. One
 669 example of a resonance between a right hand circularly polarized wave and an electron
 670 is shown in Fig. 1.10. The electron's v_{\parallel} and the wave's parallel wave vector, k_{\parallel} , are in
 671 opposite directions such that the wave frequency, ω , is Doppler shifted to an integer
 672 multiple of the Ω_e where the electron feels a static electric field and is accelerated or
 673 decelerated. Quantitatively, this resonance condition is easier to understand with the
 674 following toy model.

675 Assume a uniform magnetic field, $\vec{B} = B_0\hat{z}$, with a parallel propagating ($k = k\hat{z}$),
 676 right-hand circularly polarized wave. The wave's electric field as a function of position
 677 and time can be written as

$$\vec{E} = E_0(\cos(\omega t - kz)\hat{x} + \sin(\omega t - kz)\hat{y}). \quad (1.14)$$

The angular component of \vec{E} that will effect the particle's v_{\perp} is

$$E_{\theta} = \vec{E} \cdot \hat{\theta} = E_0 \cos(\omega t - kz + \theta). \quad (1.15)$$



$$\omega + k_{\parallel} v_{\parallel} = \Omega^-$$

Figure 1.10: The trajectories of an electron and a right-hand circularly polarized wave during a cyclotron resonance. The electron's v_{\parallel} and the wave's k_{\parallel} are in opposite directions such that the wave's frequency is Doppler shifted to an integer multiple of the electron cyclotron frequency. Figure from (Tsurutani and Lakhina, 1997).

⁶⁷⁸ Now assume that the electron is traveling in the $-\hat{z}$ direction with a velocity, $\vec{v} =$
⁶⁷⁹ $-v_0 \hat{z}$, so its time dependent position along \hat{z} is

$$z(t) = -v_0 t \quad (1.16)$$

⁶⁸⁰ and gyrophase is

$$\theta(t) = -\Omega t + \theta(0) \quad (1.17)$$

⁶⁸¹ where the first negative sign comes from the electron's negative charge. Now we put
⁶⁸² this all together into Eq. 1.1 and find the force that the electron will experience

$$m \frac{dv_{\theta}}{dt} = q E_{\theta} = q E_0 \sin((\omega + kv_0 - \Omega)t + \theta(0)). \quad (1.18)$$

⁶⁸³ This is a relatively complex expression, but when the time dependent component is
⁶⁸⁴ zero, i.e.

$$\omega + kv_0 - \Omega = 0, \quad (1.19)$$

685 the electron will feel a static electric field and be accelerated or decelerated depending
 686 on $\theta(0)$, the phase between the wave and the electron. The expression in Eq. 1.19 is
 687 commonly referred to as the resonance condition and is more generally written as

$$\omega - k_{||}v_{||} = \frac{n\Omega_e}{\gamma} \quad (1.20)$$

688 where n is the resonance order, and γ is the relativistic correction (e.g. Millan and
 689 Thorne, 2007). In the case of the cyclotron resonance ($n = 1$), the wave and cyclotron
 690 frequencies are approximately equal and thus J_1 is violated. Since J_1 is violated, J_2
 691 and J_3 are also violated since the conditions required to violate J_2 and J_3 are less
 692 stringent than J_1 .

693 It is important to remember that a particle will experience the effects of many
 694 waves along its drift orbit. The typical MLT extent of a handful of waves that are
 695 capable of resonating with radiation belt electrons are shown in Fig. 1.11.

696 Particle Losses

697 Now that we have seen two general mechanisms with which particles are
 698 accelerated in the magnetosphere, we will consider a few specific mechanisms that
 699 remove particles from the magnetosphere into the atmosphere or the solar wind.
 700 One mechanism that transports magnetosperic particles into the solar wind is
 701 magnetopause shadowing (e.g. Ukhorskiy et al., 2006). Magnetopause shadowing
 702 occurs when the ring current is strengthened and Earth's magnetic field strength is
 703 increased outside of the ring current. If the ring current increases slowly enough (such
 704 that J_3 is conserved), a particle drift shell will move outward to conserve J_3 . If the
 705 particle's drift shell expands past the magnetopause, the particle will be lost to the
 706 solar wind.

707 Another particle loss (and acceleration) mechanism is called radial diffusion and

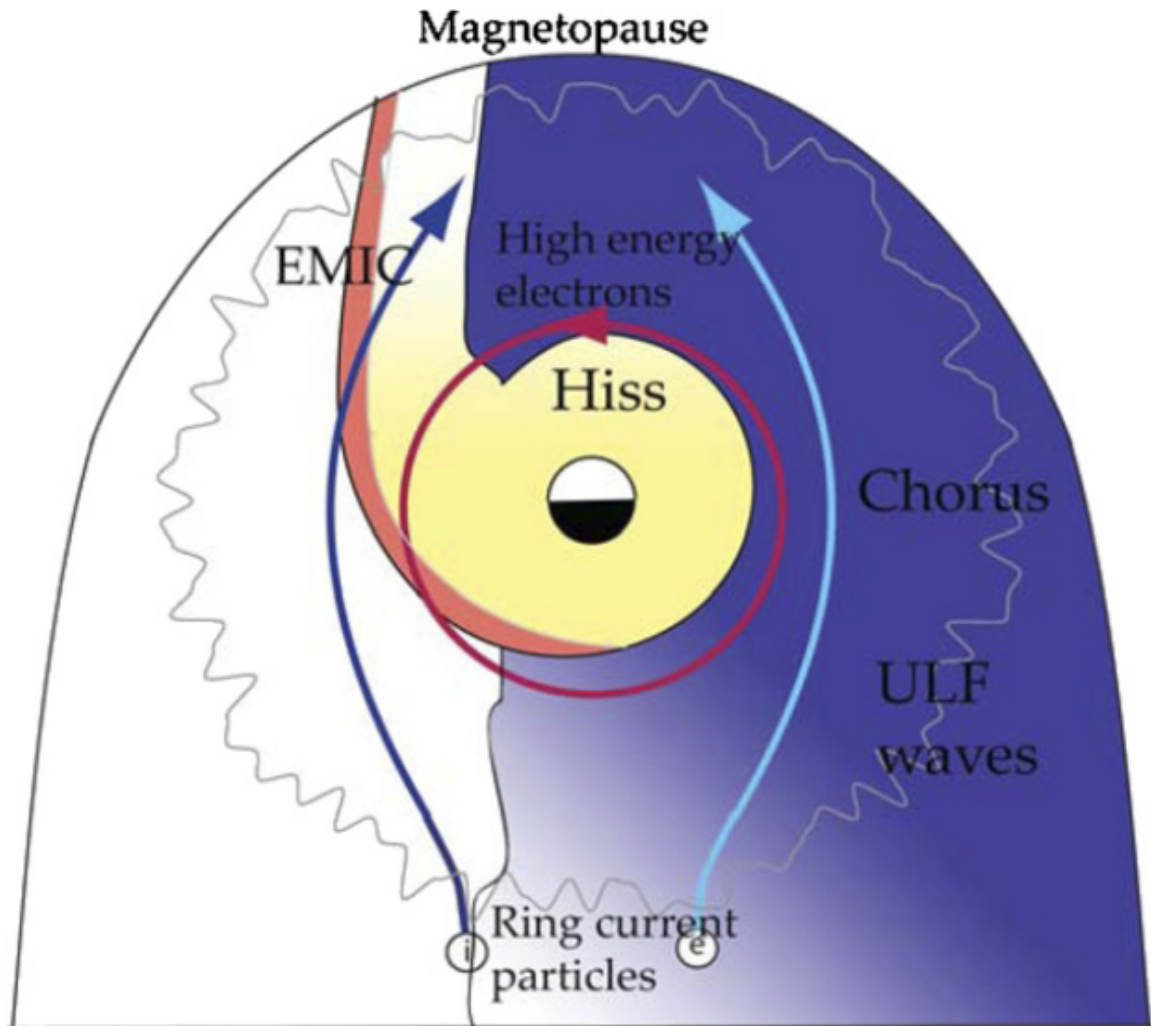


Figure 1.11: Various wave modes in the magnetosphere. Ultra low frequency waves occur through the magnetosphere. Chorus waves are typically observed in the 0-12 midnight-dawn region. EMIC waves are typically observed in the dusk MLT sector. Hiss waves are observed inside the plasmasphere. Figure from Millan and Thorne (2007).

is driven by ultra low frequency (ULF) modulation of Earth's magnetic field. For example, if the solar wind compresses the magnetopause on time scales shorter than the drift period, particles will experience radial diffusion. If the transport is radially inward, particles will be accelerated. On the other hand, radially outward radial diffusion can transport particles through the magnetopause where they will be lost to the solar wind. Reeves et al. (2013) investigated the driver of particle acceleration during the October 2012 storm and observationally found that inward radial diffusion was not dominant, rather local acceleration via wave-resonance heating appeared to be the dominant acceleration mechanism.

The loss mechanism central to this dissertation is pitch angle and energy scattering of electrons by waves. Some of the waves that scatter electrons in energy and pitch angle in the inner magnetosphere are: plasmaspheric hiss (e.g. Breneman et al., 2015; O'Brien et al., 2014), EMIC waves (e.g. Capannolo et al., 2019; Hendry et al., 2017), and chorus waves (e.g. Breneman et al., 2017; Kasahara et al., 2018; Ozaki et al., 2019). These wave-particle interactions occur when the resonance condition in Eq. 1.20 is satisfied and the particle's energy and α is modified by the wave. More details regarding the theory of pitch angle and energy diffusion is given in Chapter 2. If the wave changes α towards zero and $\alpha < \alpha_L$, then the particle's mirror point dips below 100 km altitude where the particle can be lost from the magnetosphere. One manifestation of pitch angle scattering of particles into the loss cone are microbursts, a sub-second duration impulse of electrons.

729

Microbursts

Microbursts were first seen with high altitude balloons which measured bremsstrahlung X-rays emitted by microburst electrons impacting the atmosphere by Anderson and Milton (1964). In the following years, numerous balloon flights expanded our

knowledge of non-relativistic (< 500 keV) microbursts by quantifying the microburst spatial extent, temporal width, occurrence frequency, extent in L and MLT, and their source. It is worth noting that relativistic microbursts have not yet been observed by high altitude balloons. The microburst source was initially believed to be either a local plasma instability or a propagating disturbance in the magnetosphere (Barcus et al., 1966; Brown et al., 1965; Parks, 1967; Trefall et al., 1966). Soon after, both non-relativistic and relativistic microburst electrons were directly observed in LEO with spacecraft including the Solar Anomalous and Magnetospheric Particle Explorer (SAMPEX) (e.g. Blake et al., 1996; Blum et al., 2015; Douma et al., 2019, 2017; Greeley et al., 2019; Lorentzen et al., 2001a,b; Nakamura et al., 1995, 2000; O'Brien et al., 2004, 2003), Montana State University's (MSU) Focused Investigation of Relativistic Electron Bursts: Intensity, Range, and Dynamics II (FIREBIRD-II) (Anderson et al., 2017; Breneman et al., 2017; Crew et al., 2016; Klumpar et al., 2015; Spence et al., 2012), and Science Technologies Satellite (STSAT-I) (e.g. Lee et al., 2012, 2005). An example microburst time series is shown in Fig. 1.12 and was observed by the FIREBIRD-II CubeSats. The prominent features of the example microbursts in Fig. 1.12 are their sub-second duration, half order of magnitude increase in count rate above the falling background, and their 200-800 keV energy extent.

Microbursts are observed on magnetic field footprints that are connected to the outer radiation belt (approximately $4 < L < 8$). They are predominately observed in the 0-12 MLT sector with an elevated occurrence frequency during magnetospherically disturbed times as shown in Fig. 1.13. O'Brien et al. (2003) used SAMPEX relativistic electron data and found that microbursts predominately occur during the main phase of storms, with a heightened occurrence rate during the recovery phase. Microburst occurrence rates are also higher during high solar wind velocity events e.g. from

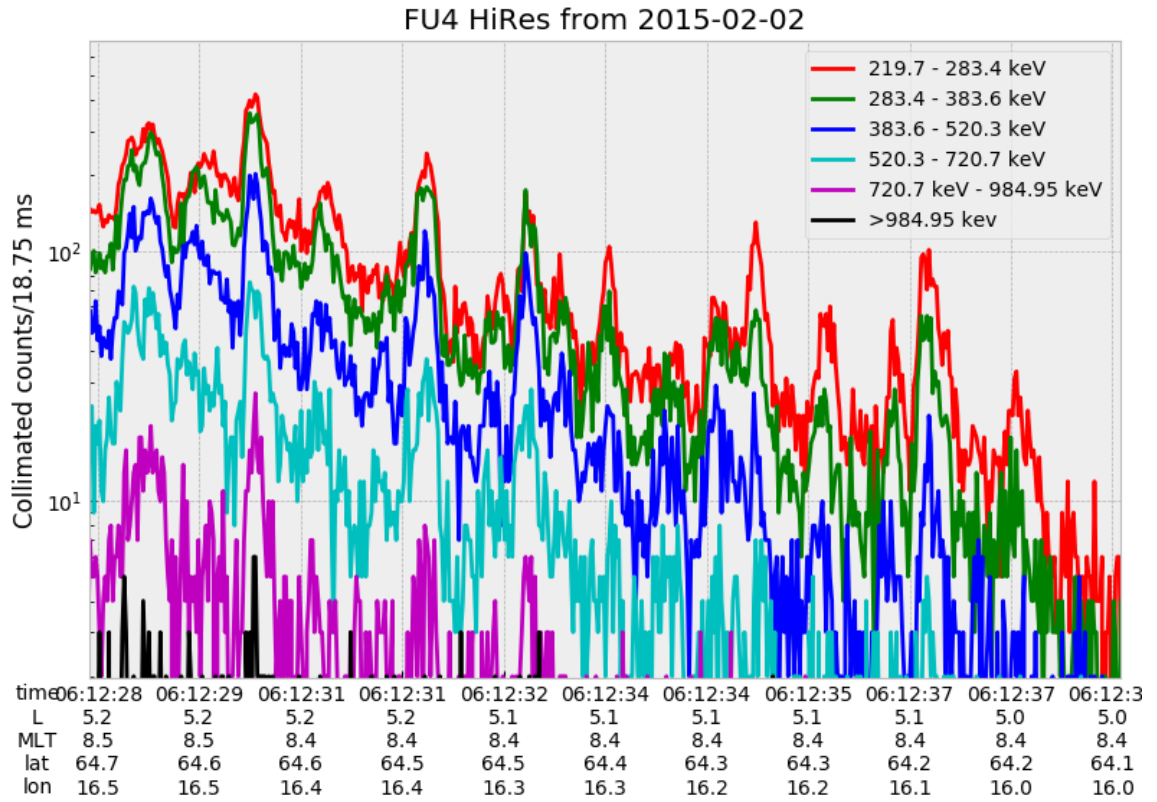


Figure 1.12: An example train of microbursts observed by FIREBIRD-II unit 4 on February 2nd, 2015. The colored curves show the differential energy channel count rates in five channels from ≈ 200 keV to 1 MeV and a sixth integral energy channel with a 1 MeV threshold. The x-axis labels show auxiliary information such as time of observation and the spacecraft position in L, MLT, latitude and longitude coordinates.

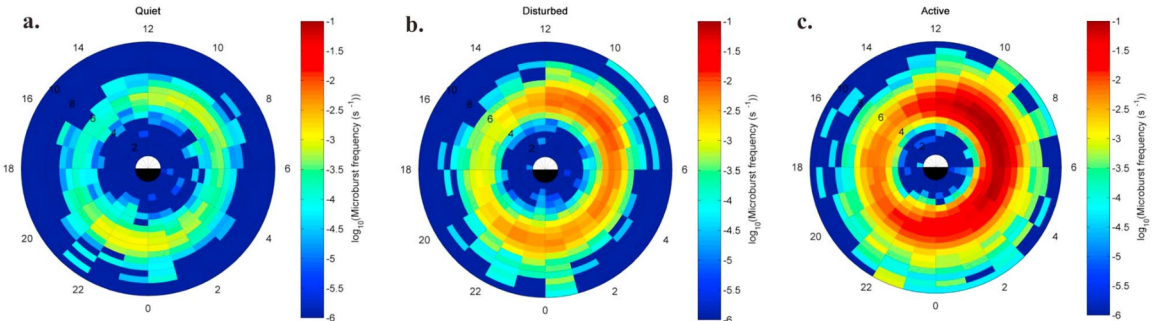


Figure 1.13: Distribution of > 1 MeV microburst occurrence rates as a function of L and MLT. The three panels show the microburst occurrence rate dependence on geomagnetic activity, parameterized by the auroral electrojet (AE) index for (a) $\text{AE} < 100 \text{ nT}$, (b) $100 < \text{AE} < 300 \text{ nT}$ and (c) $\text{AE} > 300 \text{ nT}$. Figure from Douma et al. (2017).

759 co-rotating interaction regions (Greeley et al., 2019; O'Brien et al., 2003).

760 The estimated impact of microbursts on the atmosphere and the radiation
 761 belts is significant. Relativistic microburst electrons impacting the atmosphere are
 762 ionized at < 100 km altitudes, with higher energy electrons penetrating closer to
 763 the surface. The resulting chemical reaction of microburst electrons impacting the
 764 atmosphere produces odd hydrogen HO_x and odd nitrogen NO_x molecules, which
 765 are partially responsible for destroying ozone (O_3). Seppälä et al. (2018) modeled
 766 a six hour relativistic microburst storm and found that the mesospheric ozone was
 767 reduced by 7 – 12% in the summer months and 12 – 20% in the winter months, so
 768 microbursts may have a non-negligible contribution to the dynamics of atmospheric
 769 ozone. Furthermore, microbursts have also been estimated to have a significant
 770 impact on the outer radiation belt electron population. The loss of all radiation
 771 belt electrons due to microbursts have been estimated to be on the order of a day
 772 (Breneman et al., 2017; Douma et al., 2019; Lorentzen et al., 2001b; O'Brien et al.,
 773 2004; Thorne et al., 2005).

774 The wave-particle interactions responsible for generating microbursts are also

believed to accelerate electrons in the radiation belts. As mentioned earlier, when an electron is in resonance with a wave, energy is exchanged with the wave and the electron is either accelerated or decelerated. The signature of wave-particle acceleration been observed for radiation belt electrons (e.g. Horne et al., 2005; Meredith et al., 2002; Reeves et al., 2013), and O'Brien et al. (2003) presented evidence that enhancements in chorus waves, microbursts, and radiation belt electrons are related. To explain their observations, O'Brien et al. (2003) proposed that microburst precipitation is a side effect of electron acceleration due to chorus waves.

The widely used theoretical framework to model the wave-particle interactions responsible for accelerating electrons and scattering microbursts is quasi-linear diffusion (e.g. Horne et al., 2005; Meredith et al., 2002; Summers et al., 1998; Thorne et al., 2005; Walker, 1993; ?). This framework is explained in Chapter 2, and applied to an observation of a microburst in the heart of the radiation belt. Qualitatively, when a particle is resonant with a wave it can either be transported in pitch angle towards the loss cone and lose energy to the wave, or transported away from the loss cone and gain energy from the wave.

As previously mentioned, the range of observed microburst energies range from a few tens of keV (e.g Datta et al., 1997; Parks, 1967) to greater than 1 MeV (e.g. Blake et al., 1996; Greeley et al., 2019). The microburst electron flux (J) falls off in energy, and the microburst energy spectra is typically well fit to a decaying exponential

$$J(E) = J_0 e^{-E/E_0} \quad (1.21)$$

where J_0 is the flux at 0 keV (unphysical free parameter) and E_0 quantifies the efficiency of the scattering mechanism in energy (e.g. Datta et al., 1997; Lee et al., 2005; Parks, 1967). A small E_0 suggests that mostly low energy particles are scattered.

798 In contrast a high E_0 suggests that the scattering mechanism scatters low and high
799 energy electrons. Reality is a bit more messy and a high E_0 may be a signature of a
800 scattering mechanism that is most efficient at scattering high energy electrons, with a
801 relatively minor efficiency to scatter low energy electrons. Since there are many more
802 low energy electrons available to scatter, there may be relatively more low energy
803 electrons scattered.

804 The short microburst duration, as observed by a single LEO satellite in a highly
805 inclined orbit (motion is mostly latitudinal), has an ambiguity when interpreting what
806 is a microburst. The two possible realities are: a microburst is very narrow in latitude
807 and persistent, or transient. There are a few ways to distinguish between the two
808 possible realities, and each one has a unique set of advantages.

809 A high altitude balloon essentially provides a stationary view of the precipitating
810 particles under the radiation belt footprints. An intense transient microburst can be
811 unambiguously identified above the slowly varying background. On the other hand,
812 if the microburst precipitation is stationary, there will be too little contrast between
813 the microburst and the background fluxes to be found.

814 Multi-spacecraft missions provide an alternate solution that can determine if
815 a microburst is a spatial or a transient phenomena. As is illustrated in Fig. 1.14,
816 a transient microburst can be recognized if two spacecraft, one trailing the other,
817 simultaneously observe it. The size of the microburst footprint must then be
818 larger than the spacecraft separation. On the contrary, if two spacecraft observe a
819 microburst-like feature at the same location but at different times, then the feature is
820 stationary and may be a curtain (Blake and O'Brien, 2016). Both balloon and multi-
821 spacecraft observational methods have a unique set of strengths. This dissertation
822 takes the multi-spacecraft approach to identify and study microbursts.

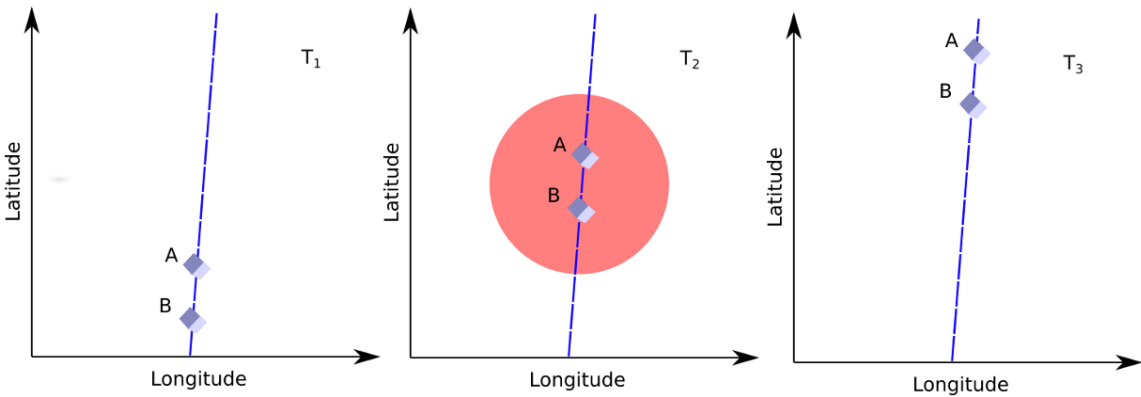


Figure 1.14: Three snapshots of a temporal microburst observed simultaneously by a pair of polar-orbiting spacecraft. The spacecraft are identified by labels "A" and "B" and are traveling upwards on the blue dashed orbital track. At T_1 the spacecraft are traveling upwards and no microburst is observed. Then at T_2 both spacecraft simultaneously observe a microburst shown by the red circle and the microburst size must be greater than the spacecraft separation. In the last snapshot, T_3 , the microburst has precipitated and no longer observed by the spacecraft.

823

Scope of Research

824 This dissertation furthers our understanding of the microburst scattering
 825 mechanism by presenting observational evidence of microburst scattering directly,
 826 and measuring microburst sizes and comparing them to the size of chorus waves.
 827 Chapter 2 describes a microburst scattering event observed by NASA's Van Allen
 828 Probes. For this event, particle and wave measurements were analyzed and modeled
 829 in the theoretical framework of pitch angle and energy diffusion. The following two
 830 chapters present studies of microburst sizes in comparison to chorus waves. Chapter
 831 3 describes a bouncing packet microburst observation made by the FIREBIRD-II
 832 mission where the microburst's lower bound longitudinal and latitudinal sizes were
 833 estimated. Chapter 4 expands the case study from Chapter 3 to a statistical study
 834 of microburst sizes using The Aerospace Corporation's AeroCube-6 (AC6) CubeSats.
 835 In this study, a Monte Carlo and analytic microburst size models were developed

836 to account for the compounding statistical effects of random microburst sizes and
837 locations. Lastly, Chapter 5 will summarize this work and make concluding remarks
838 regarding outstanding questions in microburst physics.

839

CHAPTER TWO

840

EVIDENCE OF MICROBURSTS OBSERVED NEAR THE EQUATORIAL

841

PLANE IN THE OUTER VAN ALLEN RADIATION BELT

842

Contribution of Authors and Co-Authors

843 Manuscript(s) in Chapter(s) 1

844

845 Author: [type author name here]

846 Contributions: [list contributions here, single-spaced]

847 Co-Author: [type co-author name here]

848 Contributions: [list contributions here, single-spaced]

849 Co-Author: [type co-author name here]

850 Contributions: [list contributions here, single-spaced]

851

852

Manuscript Information

853 [Type Author and Co-author(s) Names Here]

854 Geophysical Research Letters

855 Status of Manuscript: Published in a peer-reviewed journal

856 Wiley

857 Volume 45, Issue 16

858

Key Points

- 859 • First report of direct observation of microbursts at high altitude, near the
 860 equatorial plane.
- 861 • Microbursts' duration, flux enhancement, and energy spectra are similar to prior
 862 observations in LEO.
- 863 • Microburst generation is not consistent with a single quasi-linear gyroresonant
 864 interaction with chorus waves.

865

Abstract

866 We present the first evidence of electron microbursts observed near the equatorial
 867 plane in Earth's outer radiation belt. We observed the microbursts on March 31st,
 868 2017 with the Magnetic Electron Ion Spectrometer and RBSP Ion Composition
 869 Experiment on the Van Allen Probes. Microburst electrons with kinetic energies
 870 of 29-92 keV were scattered over a substantial range of pitch angles, and over time
 871 intervals of 150-500 ms. Furthermore, the microbursts arrived without dispersion in
 872 energy, indicating that they were recently scattered near the spacecraft. We have
 873 applied the relativistic theory of wave-particle resonant diffusion to the calculated
 874 phase space density, revealing that the observed transport of microburst electrons is
 875 not consistent with the hypothesized quasi-linear approximation.

876

Introduction

877 Since the Van Allen radiation belts were discovered by Van Allen (1959) and
 878 Vernov and Chudakov (1960), decades of work has focused on understanding their
 879 origins and effects on the near-Earth space environment and ionosphere-thermosphere

system. The energy content of the outer belt is dominated by energetic electrons, with dynamics controlled by a complex interplay between various source and loss mechanisms. One important loss and acceleration mechanism is gyroresonant diffusion in energy and pitch angle (PA) due to scattering of electrons by plasma waves (e.g. Bortnik et al., 2008; Horne and Thorne, 2003; Meredith et al., 2002; Millan and Thorne, 2007; Summers et al., 1998; Thorne and Andreoli, 1981; Thorne et al., 2005; Walker, 1993).

Chorus waves are commonly associated with PA and energy diffusion. These waves are typically generated by substorm injections into the inner magnetosphere, which lead to a temperature anisotropy of the source electrons with energies up to tens of keV (e.g. Horne et al., 2003; Li et al., 2009a). Since these source electrons drift eastward, chorus is most frequently observed in the dawn sector, but it has been observed at all magnetic local times (MLT) (Li et al., 2009b). Chorus waves are believed to generate electron microburst precipitation through wave-particle interactions.

Microbursts are typically defined as an increase of electron flux in or near the atmospheric loss cone that last < 1 s (e.g. Anderson and Milton, 1964; Blake et al., 1996; Lorentzen et al., 2001a). Empirical and theoretical analyses indicate that microbursts are an important loss process since they can substantially deplete the radiation belt electrons on the order of one day (e.g. Breneman et al., 2017; Lorentzen et al., 2001b; O'Brien et al., 2004; Thorne et al., 2005). Previously, microbursts have been observed in the upper atmosphere in the form of bremsstrahlung X-rays (e.g. Anderson et al., 2017; Parks, 1967; Woodger et al., 2015) and directly in low Earth orbit (LEO) (e.g. Blake et al., 1996; Blum et al., 2015; Breneman et al., 2017; Crew et al., 2016; Lee et al., 2012, 2005; Lorentzen et al., 2001a,b; Mozer et al., 2018; Nakamura et al., 1995, 2000; O'Brien et al., 2004, 2003).

906 We observed for the first time, microburst-like signatures near their hypothesized
 907 origin within the heart of the outer radiation belt. The unique microburst
 908 observations we report here were possible with the Van Allen Probe-A's (RBSP-
 909 A) Magnetic Electron Ion Spectrometer's (MagEIS) fast sampling rate (\sim 11 ms),
 910 and RBSP Ion Composition Experiment's (RBSPICE) PA coverage. The observed
 911 microbursts' duration, energy spectra, and energy dispersion signature were similar to
 912 microbursts previously reported from LEO. Furthermore, we simultaneously observed
 913 structureless "hiss-like" whistler mode wave power in the lower band chorus frequency
 914 range (Li et al., 2012). From previous observations in LEO (e.g. Blake et al., 1996),
 915 it is believed that microbursts result from the impulsive scattering of electrons into
 916 or near the loss cone, which is on the order of a few tens of degrees in LEO. With this
 917 assumption, high altitude microburst observations near the magnetic equator should
 918 be very difficult to make since the atmospheric loss cone there is only a few degrees
 919 wide. Thus, the loss cone is smaller than the angular resolution of most particle
 920 detectors. Even when an instrument is observing the loss cone, the instrument's field
 921 of view will include some portion of the trapped population. The trapped electron flux
 922 is typically orders of magnitude higher than that in the loss cone, so that microbursts
 923 scattered into the loss cone will be obscured. We present observational evidence that
 924 suggests that the sudden impulse of electrons studied here is consistent with the
 925 creation of microbursts. Furthermore, these microbursts were scattered over a broad
 926 PA range outside of the loss cone, though the loss cone was not directly observed by
 927 MagEIS and RBSICE.

928 This paper explores the properties of the observed microbursts by utilizing in-
 929 situ RBSP measurements of waves and particles. This unique high altitude point of
 930 view enables us to test whether the observed microburst scattering is consistent with
 931 a quasi-linear diffusion process. We have tested this hypothesis with in-situ electron

932 phase space density (PSD) measurements and the relativistic theory of wave-particle
 933 resonant diffusion (Summers et al., 1998; Walker, 1993) to determine if the microburst
 934 electrons diffused in PA and energy.

935 Spacecraft Instrumentation

936 NASA's RBSP mission (Mauk et al., 2013), launched on August 30th, 2012,
 937 consists of a pair of identically instrumented spacecraft. Their orbit and instru-
 938 mentation are uniquely configured to enrich our understanding of the particles and
 939 waves in the inner magnetosphere. The RBSP spacecraft are in highly elliptical, low-
 940 inclination orbit, with perigee of \sim 600 km and apogee of \sim 30,000 km altitude. Their
 941 attitude is maintained by spin-stabilization with a period of \sim 11 s and the spin axis is
 942 roughly sun-pointing. In this analysis, energetic electron measurements from MagEIS
 943 (Blake et al., 2013) and RBSPICE (Mitchell et al., 2013) were used, complemented by
 944 magnetic field and wave measurements from Electric and Magnetic Field Instrument
 945 and Integrated Science (EMFISIS) (Kletzing et al., 2013).

946 We observed these microbursts with RBSP-A's MagEIS low energy instrument
 947 (MagEIS-A) which measures 20-240 keV electrons. It has an angular acceptance
 948 of $3^\circ - 10^\circ$ in the spacecraft spin plane, and 20° perpendicular to the spin plane.
 949 MagEIS-A has a high rate data mode which samples at 1000 angular sectors per
 950 spacecraft spin (11 ms cadence). MagEIS low on RBSP-B on the other hand samples
 951 at 64 angular sectors per spacecraft spin (172 ms cadence), so it was only used for
 952 context.

953 To expand the PA coverage of MagEIS-A, we used the RBSPICE-A time-of-
 954 flight instrument. RBSPICE-A measures electron energies in the range of 19 keV -
 955 1 MeV with a fan of six telescopes (the sixth telescope is used only for calibration
 956 and was excluded from this analysis). These telescopes have an overall acceptance

957 angle of 160° by 12° which allows them to simultaneously sample a substantial part
 958 of the Pitch Angle Distribution (PAD). RBSPICE-A gathers data over 32 sectors
 959 per spacecraft spin (≈ 310 ms cadence) and each sector is divided into three sub-
 960 sectors corresponding to three measurement modes (Manweiler and Zwiener, 2018).
 961 At the time of the observation, the sub-sector used for electron measurements had
 962 an accumulation time of 77 ms. We used RBSPICE-A's Electron Basic Rate (EBR)
 963 telemetry data in this analysis which is not averaged, though it is an integral energy
 964 channel.

965 To understand the dynamics of the local magnetic field, we used the EMFISIS
 966 instrument. EMFISIS provides measurements of the DC magnetic field with flux gate
 967 magnetometers. In addition, it measures electromagnetic waves from 10 Hz to 500
 968 kHz with search coil magnetometers. The spectral matrix and burst data products
 969 used in this analysis were from the EMFISIS waveform receiver (WFR) (10 Hz - 12
 970 kHz) and the high frequency receiver (10 kHz - 500 kHz). Burst data were selectively
 971 captured at a 35 kHz sample rate, and the survey mode spectral matrix data was
 972 captured every 6s.

973

Observations

974 MagEIS-A and RBSPICE-A observed the microburst-like signatures on March
 975 31st, 2017 at $L^* \approx 6$ and $MLT \approx 19$, calculated with the Tsyganenko 2004 magnetic
 976 field model (Tsyganenko and Sitnov, 2005). The magnetosphere was in the recovery
 977 phase of a storm, with minimum Dst of -75 nT observed on March 27th. The local
 978 electron number density was on the order of 1 cm^{-3} at this time, so both RBSP
 979 spacecraft were located outside the plasmasphere. The two spacecraft were separated
 980 by 1700 km, at magnetic latitudes $\lambda \approx -19^\circ$ and $\lambda \approx -18^\circ$ for RBSP-A and RBSP-B,
 981 respectively.

982 MagEIS-A observed microburst electron flux (J) at energies ≥ 92 keV around
 983 11:17 UT as shown in panel (a) in Fig. 4.1. For directional information, panel (b)
 984 in Fig. 4.1 shows flux as a function of local pitch angle (α_L) and time for 46-66 keV
 985 electrons. Electrons that traveled towards the northern hemisphere had $\alpha_L < 90^\circ$ and
 986 southern hemisphere had $\alpha_L > 90^\circ$. The interval between the two vertical dashed
 987 black lines contain the four microbursts examined in this study. We observed these
 988 microbursts at $\alpha_L < 50^\circ$, but MagEIS-A did not sample into the 0° loss cone.

989 Figure 4.1 panel (c) shows the EMFISIS WFR data from RBSP-A. Between
 990 11:17:05 and 11:17:10 UT, we observed an isolated burst of whistler mode wave power
 991 in the frequency range $0.1 < \omega < 0.3 \Omega_{ce0}$, where Ω_{ce0} is the equatorial electron
 992 gyrofrequency. No individual rising or falling tone elements were observed during
 993 this period, and the waves appeared more “hiss-like” (e.g. Li et al., 2012). This wave
 994 was near-parallel propagating (evidence shown in Appendix A) and about 10 minutes
 995 later, weak chorus rising tone elements were observed (not shown).

996 Panels (d)-(f) in Fig. 4.1 are in the same format as panels (a)-(c), but for RBSP-
 997 B. An injection or boundary was observed with RBSP-B at 11:16:50 UT and RBSP-A
 998 observed a similar feature soon after 11:18 UT (not shown).

999 A zoomed-in version of Fig. 4.1 panels (a) and (b) is shown in Fig. 4.2. Panel
 1000 (a) shows the four microburst-like signatures observed between 11:17:10 and 11:17:12
 1001 UT, at energies up to 92 keV. The observed duration of the microbursts was 150
 1002 - 500 ms, and they did not arrive dispersed in energy, which indicates that they
 1003 were recently scattered near the spacecraft location. We use IRBEM-Lib, a library
 1004 dedicated to radiation belt modeling (Boscher et al., 2012), to calculate the mirror
 1005 point altitudes, which were found to be above LEO. Panel (b) shows the RBSPICE-
 1006 A EBR time series with the group of microbursts observed at the same time as
 1007 in panel (a). To understand the timing relationship between the MagEIS-A and

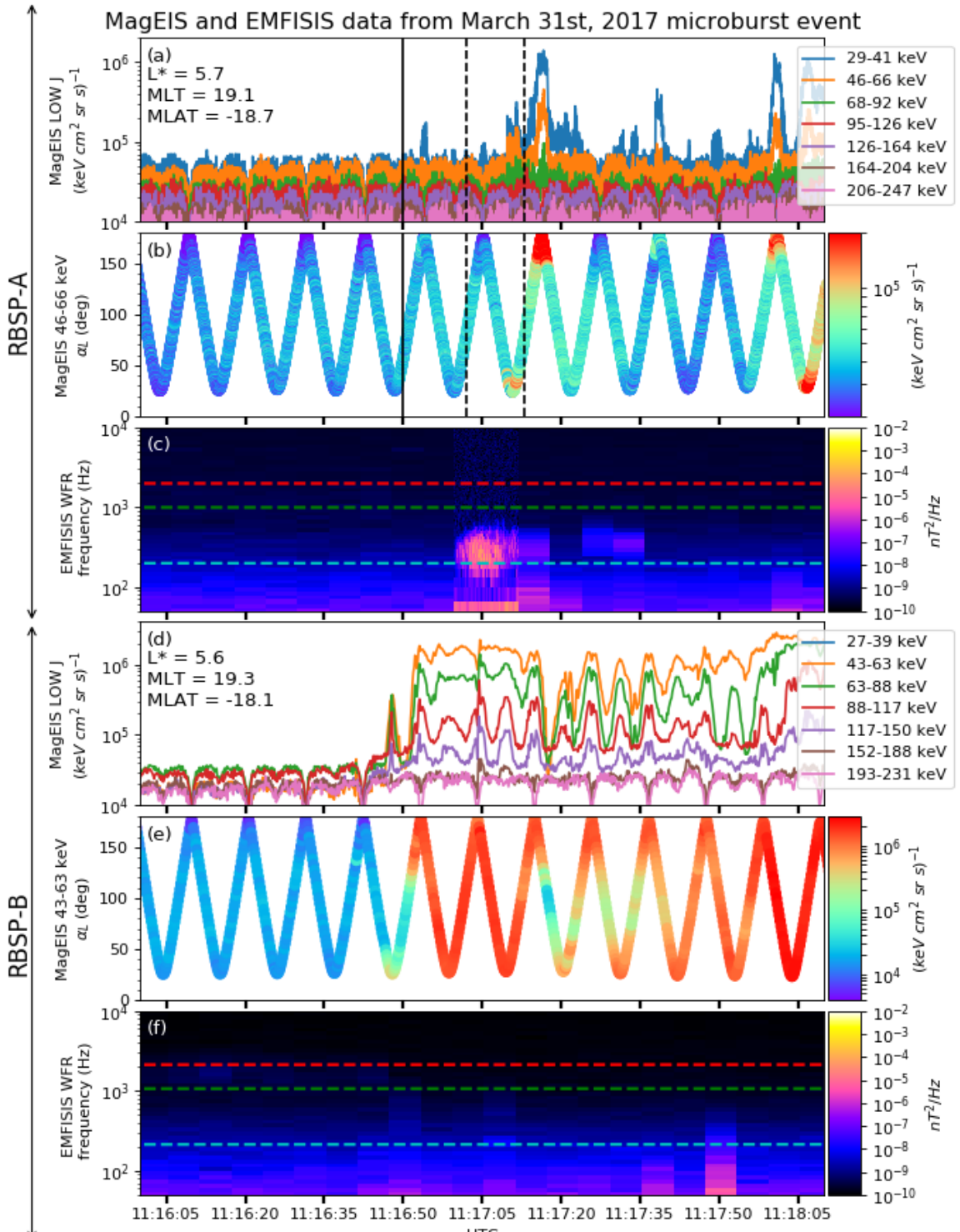


Figure 2.1: Electron and wave conditions from the MagEIS-A and EMFISIS WFR sensors for the microburst time interval. Panels (a), (b), and (c) are from RBSP-A with its position information annotated in panel (a). Panels (d), (e), and (f) are from RBSP-B with its position information annotated in panel (d). Panel (a) is the MagEIS-A high rate timeseries. Panels (b) and (e) show the evolution of the MagEIS-A J as a function of α_L from the ~ 40 to ~ 60 keV channel. Every 10th point is shown in panel (b). The solid black line in panels (a) and (b) mark the end of the time period used for the PSD fit extrapolation analysis explained in section

1008 RBSPICE-A observations, we marked the times when MagEIS-A observed the four
 1009 microbursts by vertical black arrows in panels (a) and (b). MagEIS-A observed the
 1010 first microburst ~ 0.5 s before RBSPICE-A. The bounce period of locally mirroring,
 1011 100 keV electrons was ~ 0.8 s, so this was unlikely to have been a returning bounce.
 1012 This evidence confirms that these microburst signatures are packets of electrons and
 1013 not a boundary moving back and forth at RBSP-A's location. To understand the
 1014 PA extent of these microbursts, panel (c) shows the 29-41 keV MagEIS-A J and
 1015 RBSPICE-A EBR as a function of α_L and time. The microburst J was observed
 1016 by MagEIS-A between $25^\circ < \alpha_L < 50^\circ$ and RBSPICE-A between $100^\circ < \alpha_L < 160^\circ$,
 1017 with the highest intensities close to $\alpha_L = 90^\circ$. RBSPICE-A observed a 10-80%
 1018 enhancement in count rate over those PAs with the evidence presented in Appendix
 1019 A.

1020 Analysis

1021 First, we estimated the microburst energy spectra. For each microburst shown in
 1022 Fig. 4.2, its flux was averaged and baseline subtracted using the method from O'Brien
 1023 et al. (2004) and then fit with an exponential function. The calculated exponential
 1024 E-folding energy was found to vary between 25 and 35 keV, which is consistent with
 1025 spectra derived from prior measurements (Datta et al., 1997; Lee et al., 2012, 2005).

1026 We then tested the hypothesis that the microburst electrons were transported
 1027 in energy and PA by a single chorus wave. We used a procedure similar to sections
 1028 3.1 and 4.5 in Meredith et al. (2002) which we describe below.

1029 Microburst and Source PSD

1030 We estimated the electron PSD, $f(p_\perp, p_\parallel)$ where p_\perp and p_\parallel are the perpendicular
 1031 and parallel components of the electron momentum relative to the local magnetic field,

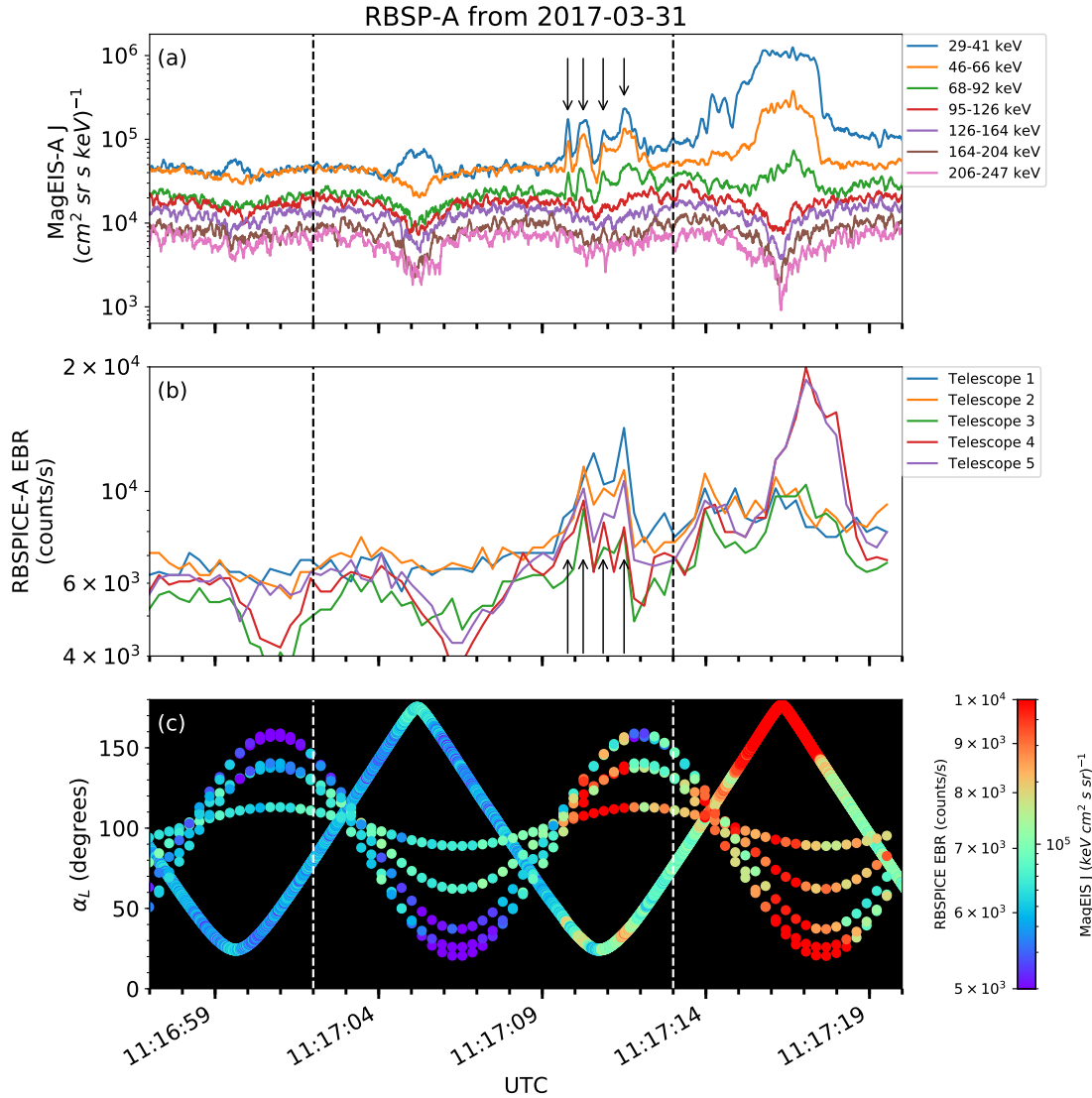


Figure 2.2: Panel (a) shows the MagEIS-A high rate timeseries. Panel (b) shows the RBSPICE EBR count rate timeseries for $\zeta = 19$ keV electrons. The microbursts were observed between 11:17:10 - 11:17:12 UT and are indicated with the vertical black arrows in panels (a) and (b) for MagEIS-A times. Panel (c) shows the RBSPICE EBR (family of relatively sparse sampled curves) and MagEIS-A J from the 29-41 keV energy channel (single curve) as a function of α_L . The vertical dashed lines show the time interval for the PSD analysis.

for the microburst time period. MagEIS-A $J(E, \alpha_L)$ was averaged between 11:17:02 and 11:17:13 UT and binned by α_L into 5° bins. Then, we assumed the conservation of the first adiabatic invariant and mapped α_L to equatorial PA, α_{eq} . The binned $J(E, \alpha_{eq})$ was then converted to $f(p_\perp, p_\parallel)$ via

$$f(p_\perp, p_\parallel) = \frac{J(E, \alpha_{eq})}{p^2}, \quad (2.1)$$

where $p = \sqrt{p_\perp^2 + p_\parallel^2}$. Lastly, α_{eq} was used to separate p into p_\perp and p_\parallel via

$$\frac{p_\parallel}{m_e c} = \frac{\sqrt{E(E + 2E_0)} \cos(\alpha_{eq})}{E_0} \quad (2.2)$$

$$\frac{p_\perp}{m_e c} = \frac{\sqrt{E(E + 2E_0)} \sin(\alpha_{eq})}{E_0} \quad (2.3)$$

where c is the speed of light, E is the kinetic energy, m_e is the electron mass, and E_0 is the electron rest energy. The observed $f(p_\perp, p_\parallel)$ in dimensionless momentum space is shown in Fig. 4.3 in all panels between the p_\parallel axis and the white dotted lines. The bright spot in $f(p_\perp, p_\parallel)$ in the upper p_\parallel plane represents the four microbursts. Along with the observed PSD, we use Fig. 4.3 to explore the various PSD extrapolation and diffusion model assumptions which are described below.

We proceed under the assumption that the source of the microburst electrons is not likely to be at the latitude of the observation, and is closer to the magnetic equator. To look for a source of microburst electrons, we extrapolate the unobserved $f(p_\perp, p_\parallel)$ of electrons with $|\lambda_m| < 19^\circ$ using two cases with a 90° -peaked PAD of the form

$$f(E, \alpha_{eq}) = f_0(E) \sin^n(\alpha_{eq}) \quad (2.4)$$

where $f_0(E)$ is a scaling parameter and n is a power parameter. Similarly to the

1044 in-situ $f(p_{\perp}, p_{||})$, the $f(E, \alpha_{eq}) \mapsto f(p_{\perp}, p_{||})$ conversion was applied.

1045 In the first case, we fitted Eq. 2.4 to the quiet time $J(E, \alpha_{eq})$ from 11:15:00 to
 1046 11:16:50 UT (end time shown as the black vertical line in Fig. 4.1). The fitted
 1047 PAD was relatively flat with $0.4 < n < 0.5$ and highest magnitude of f_0 was
 1048 $0.05 c^3/(cm MeV)^3$. This extrapolated $f(p_{\perp}, p_{||})$ is shown in Fig. 4.3 panels (A) and
 1049 (E), between the dotted white lines for scattering at $\lambda = 0^\circ$ and 20° , respectively.
 1050 To confirm the relatively low n parameter, we found times where RBSP-A was in
 1051 a similar L-MLT location, but closer to the magnetic equator. At 2 and 19 UT on
 1052 the same day, we fit the $J(E, \alpha_{eq})$, and the fit parameters were very similar to the
 1053 pre-microburst $f(p_{\perp}, p_{||})$ at 11 UT. Thus it is a reasonable assumption that $f(p_{\perp}, p_{||})$
 1054 was relatively flat near the equator.

1055 In the other case, we estimate how large n would have to be in order to find
 1056 sufficient PSD in MagEIS-A's energy range to be a source of the microburst electrons.
 1057 We used $n \in \{1, 2, 4\}$ and we forced the $f_0(E)$ parameter to match the observed
 1058 $f(p_{\perp}, p_{||})$ at the most equatorial PAs observed by MagEIS-A. These extrapolations
 1059 are shown in columns 2-4 in Fig. 4.3. There was enough source PSD anywhere in
 1060 MagEIS-A's energy range only if $n \geq 2$.

1061 Motion of resonant electrons in phase space

To calculate the motion of resonant electrons in momentum space, we used the relativistic theory of wave-particle resonant diffusion developed by Walker (1993) and Summers et al. (1998) and applied in Meredith et al. (2002). The chorus wave can modify $f(p_{\perp}, p_{||})$ when a resonance condition is satisfied. The cyclotron resonance condition between an electron with velocity $v = \sqrt{v_{||}^2 + v_{\perp}^2}$ and a parallel propagating

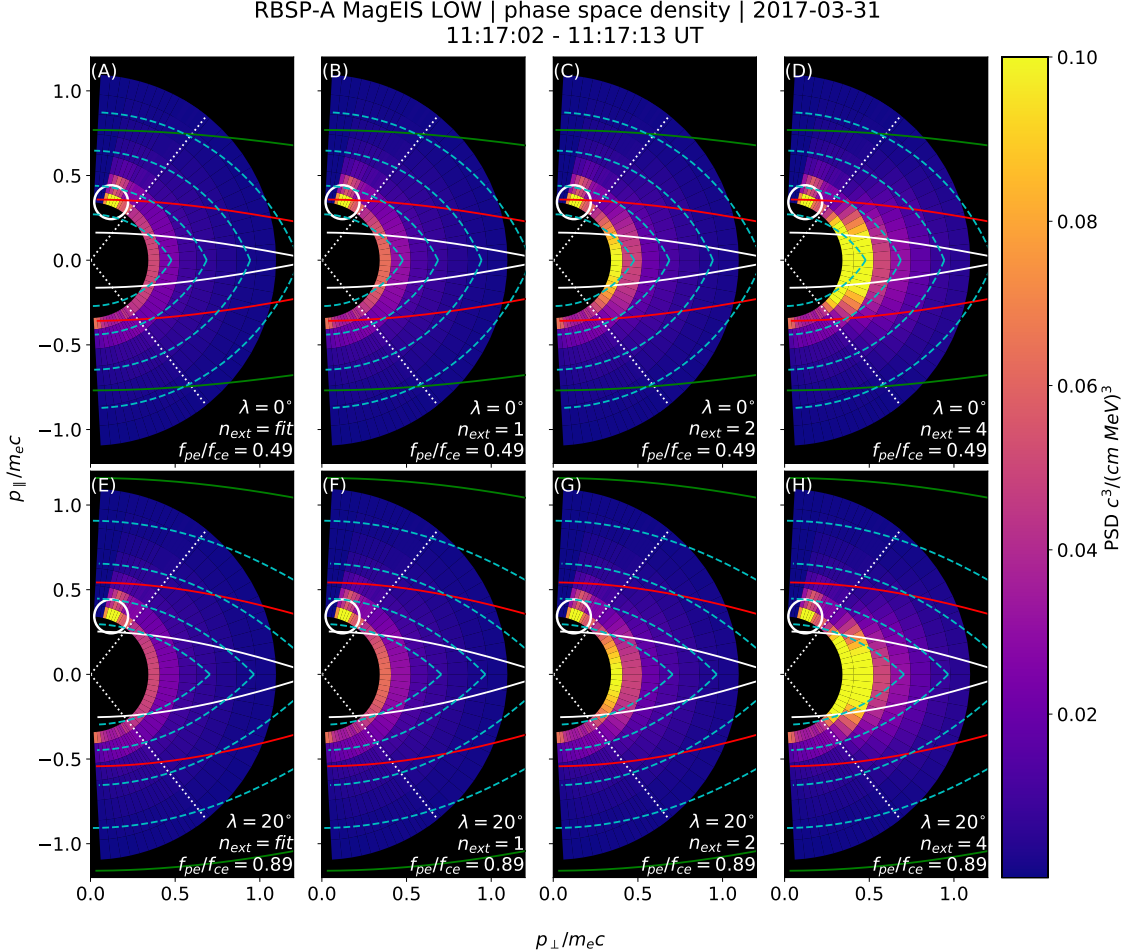


Figure 2.3: The colored annulus represents $f(p_\perp, p_\parallel)$ in normalized momentum space, parallel and perpendicular to the background magnetic field. The microburst $f(p_\perp, p_\parallel)$ is highlighted with the white circle. The columns show different powers of the sine extrapolation, and rows show the different magnetic latitudes of the scattering. The white dotted traces represent the boundary between the data and extrapolation. The green, red, and white solid traces are the resonance curves for $\omega = 0.2\Omega_{ce}$, $0.4\Omega_{ce}$, $0.6\Omega_{ce}$, respectively. The cyan dashed traces are the diffusion curves for a $\omega = 0.4\Omega_{ce}$ wave (waves of other frequency have similar diffusion curves). The magnetic latitude of the scattering, the ratio of the plasma to the cyclotron frequency, and the power of the sine extrapolation is annotated in each panel. For the resonance and diffusion curves, the density model assumed a $n_L = 1 e^-/cm^3$ and $\psi = -1$.

wave of frequency ω and wave number k_{\parallel} is given by

$$\omega - v_{\parallel} k_{\parallel} = \frac{\Omega_{ce}}{\gamma}, \quad (2.5)$$

where Ω_{ce} is the electron gyrofrequency at the scattering location, and γ is the relativistic correction. Assuming the cold plasma approximation,

$$k_{\parallel} = \frac{\omega}{c} \sqrt{1 - \frac{\omega_{pe}^2}{\omega(\omega - |\Omega_{ce}|)}}, \quad (2.6)$$

where ω_{pe} is the plasma frequency. For a particular set of parameters, Eq. 2.5 defines a curve in momentum space that describes which electrons will resonate with a monochromatic wave.

To calculate k_{\parallel} , we approximated the electron number density, $n_e(\lambda)$ locally and at the magnetic equator. Locally, the plasma density was approximately $n_e(\lambda = -20^\circ) = n_L \approx 1 \text{ cm}^{-3}$. We used magnetospheric seismology techniques (e.g. Takahashi and Denton, 2007) to parameterize $n_e(\lambda)$ elsewhere along the field line with

$$n_e(\lambda) = n_e(0) \left(\frac{LR_e}{R(\lambda)} \right)^{\psi} \quad (2.7)$$

where R_e is the Earth's radius, $R(\lambda)$ is the radial distance from the Earth to the spacecraft, and ψ is the exponent parameter. Assuming a dipole magnetic field for which $R(\lambda) = LR_e \cos^2 \lambda$ (e.g. Schulz and Lanzerotti, 1974), we can express Eq. 2.7 in terms of n_L via

$$n_e(\lambda) = n_L \left(\frac{\cos \lambda_L}{\cos \lambda} \right)^{2\psi} \quad (2.8)$$

where we used $\psi = -1$ (higher density at the magnetic equator) in this analysis. We chose this exponent parameter because it is a realistic best case scenario for the

¹⁰⁷² electrons to be transported along the diffusion curves (described below).

Walker (1993) and Summers et al. (1998) argued that a resonant electron will move along diffusion curves in momentum space. A diffusion curve is derived as follows. In the reference frame moving with a monochromatic chorus wave's phase velocity (wave frame), the chorus wave is stationary and there is no electric field. Thus in the wave frame, the electron's kinetic energy is conserved, and the electron's velocity in the wave frame can be expressed in differential form as

$$v_{\parallel}dv_{\parallel} + v_{\perp}dv_{\perp} = 0. \quad (2.9)$$

After a Lorentz transformation of Eq. 2.9 into the magnetosospheric frame, kinetic energy will no longer be conserved. After integration and manipulation of Eq. 2.9, we obtain:

$$\left(1 - \frac{u_0^2 v_0^2}{c^4}\right)v_{\parallel}^2 - 2u_0\left(1 - \frac{v_0^2}{c^2}\right)v_{\parallel} + \left(1 - \frac{u_0^2}{c^2}\right)v_{\perp}^2 = v_0^2 - u_0^2 \quad (2.10)$$

¹⁰⁷³ where $u_0 = \omega/k_{\parallel}$ is the phase velocity, and v_0 is a constant of integration (Summers
¹⁰⁷⁴ et al., 1998; Walker, 1993). Equation 2.10 defines a family of diffusion curves in
¹⁰⁷⁵ momentum space on which resonant electrons will move. The distance that an
¹⁰⁷⁶ electron moves along a diffusion curve is a function of wave and plasma parameters,
¹⁰⁷⁷ and is estimated from the magnitude of the diffusion coefficients and the resonance
¹⁰⁷⁸ time.

¹⁰⁷⁹ Comparing the microburst PSD to diffusion theory

¹⁰⁸⁰ Superposed on the PSD plots in Fig. 4.3 are resonance curves for chorus waves
¹⁰⁸¹ of $\omega = 0.2\Omega_{ce}$, $0.4\Omega_{ce}$, $0.6\Omega_{ce}$ and a few diffusion curves for a $\omega = 0.4\Omega_{ce}$ wave.
¹⁰⁸² These curves were parameterized by λ using a dipole magnetic field for $\lambda = 0^\circ$

(Fig. 4.3, panels A-D) and $\lambda = 20^\circ$ (Fig. 4.3, panels E-H). If the transport of microburst electrons is consistent with gyro-resonant diffusion, a diffusion curve that passes through the microburst $f(p_\perp, p_\parallel)$ must also pass through another region with at least the same magnitude PSD ($f(p_\perp, p_\parallel) \geq 0.1 \text{ c}^3/(\text{cm MeV})^3$) e.g. Fig. 4.3, panel (D). With this constraint, an artificially high extrapolated $f(p_\perp, p_\parallel)$ with $n > 2$ (5 times larger than calculated from the fits) must be assumed for there to have been a sufficient source of PSD anywhere in MagEIS-A's energy range.

We now show that by comparing MagEIS observations with theory, that the minimum wave amplitude necessary to scatter these electrons is much higher than was observed by EMFISIS-A. If we assume a unrealistic PAD with enough PSD just equatorward of RBSP-A, we can use MagEIS-A observations to calculate the minimum $\Delta\alpha_{eq}$ that the electrons were transported. We then used diffusion theory to calculate the necessary wave amplitude. For microbursts with larger PAs, MagEIS-A observed a transport of $\Delta\alpha_{eq} = 9^\circ$ and for microbursts with smaller PAs, the observed transport was $\Delta\alpha_{eq} = 24^\circ$. The required wave amplitude was calculated with Eq. 3 from Thorne and Andreoli (1981) assuming a maximum resonance period of a quarter bounce. The observed change in PA requires a wave amplitude $0.2 < |B_w| < 0.5 \text{ nT}$. For a few brief moments, the EMFISIS-A WFR waveform data showed $0.1 < |B_w| < 0.15 \text{ nT}$, so a transport of 9° is plausible, but not likely for 24° .

Another source of microburst electrons may be from energies below MagEIS-A's range. The Helium, Oxygen, Proton, and Electron mass spectrometer (Funsten et al., 2013) on RBSP-A observed $f(p_\perp, p_\parallel) \geq 0.1 \text{ c}^3/(\text{cm MeV})^3$ for $\gtrsim 23 \text{ keV}$ electrons at this time. We then assumed the wave amplitude derived above to predict the transport in energy. We used the fact that the momentum and pitch angle diffusion coefficients, D_{pp} and $D_{\alpha\alpha}$ are related via $D_{pp}/p^2 \sim D_{\alpha\alpha}$ or equivalently, $\Delta p/p \sim \Delta\alpha$. The observed PA transport corresponds to an energy transport of $6 < \Delta E < 16$

1109 keV. Therefore, this wave can transport 23 keV electrons from smaller pitch angles
 1110 to larger pitch angles and would be observed in the 29 – 41 keV MagEIS-A channel.
 1111 However, this wave is insufficient to transport electrons to the 68 – 92 keV channel
 1112 in one interaction. Therefore we conclude that quasi-linear diffusion cannot explain
 1113 the observed microbursts.

1114

Discussion and Conclusions

1115 These novel observations of impulsive electron signatures reported here fall
 1116 well within the broad definition of a microburst as described in section 3. Their
 1117 properties were similar to microbursts observed in LEO, with an E-folding energy of
 1118 $25 < E_0 < 35$ keV (Datta et al., 1997; Lee et al., 2012, 2005), duration of 150-500
 1119 ms (Lorentzen et al., 2001a), observed upper energy limit of 92 keV, and a lack of
 1120 clear energy dispersion (Breneman et al., 2017). With MagEIS-A’s high time and
 1121 energy resolution, we conclude that these dispersionless microbursts were recently
 1122 scattered near the spacecraft. Furthermore, RBSPICE-A’s PA coverage suggests
 1123 that these electrons were scattered over a substantial range of PAs, with the highest
 1124 intensities near $\alpha_L = 90^\circ$. Overall, our observational evidence suggests that on time
 1125 scales shorter than one bounce period, the chorus wave effectively accelerated trapped
 1126 electrons over a broad PA range.

1127 In the theoretical framework of wave-particle resonant diffusion applied to the
 1128 observed PSD in section 3, we determine that the observed scattering is not consistent
 1129 with the quasi-linear approximation. The nearest source of sufficient PSD is too
 1130 far away in phase space to have been transported by the hypothesized quasi-linear
 1131 process over a timescale shorter than one bounce period (one interaction). A similar
 1132 conclusion was made by Mozer et al. (2018) who used quasi-linear theory constrained
 1133 by RBSP wave measurements. They successfully modeled the one second average

1134 precipitating flux observed with AeroCube-6 (AC-6) CubeSats during a conjunction,
 1135 but they were unable to model the AC-6 fluxes on smaller time scales.

1136 To put these microburst observations into a wider magnetospheric perspective,
 1137 we observed them during the recovery phase of a minimum Dst of -75 nT storm, a
 1138 statistically favorable time period for microbursts (O'Brien et al., 2003). Furthermore,
 1139 during the same storm on March 27th, the Arase spacecraft observed highly correlated
 1140 lower band chorus with 10-50 keV electron precipitation inside the loss cone. At
 1141 that time, Arase's magnetic field footprint was near The Pas All-Sky Imager (part
 1142 of the THEMIS mission) which simultaneously observed pulsating auroral patches
 1143 (Kasahara et al., 2018). While microbursts and pulsating auroral patches have not
 1144 been clearly connected, they are both believed to be a product of electron scattering
 1145 by whistler mode waves (e.g. Lorentzen et al., 2001a; Nishimura et al., 2011; O'Brien
 1146 et al., 2003; Ozaki et al., 2012).

1147 The combined capabilities of the various RBSP wave and particle instruments
 1148 enable comprehensive studies of wave-particle scattering and the resulting microburst
 1149 precipitation. From a preliminary search by the authors, other microburst-like
 1150 signatures have been found with RBSP. Similar to previous studies (e.g. Blum et al.,
 1151 2015; O'Brien et al., 2003), a statistical study of high-altitude microbursts in L-MLT
 1152 space needs to be conducted before we can verify that these microbursts are the
 1153 counterpart of the microbursts observed in LEO and the upper atmosphere.

1154 Acknowledgments

1155 The authors acknowledge the technicians, engineers, and scientists who made the
 1156 RBSP and AC-6 missions possible. One author (Shumko) would like to acknowledge
 1157 Dana Longcope for his help in understanding the quasi-linear diffusion theory. Dr.
 1158 Gkioulidou was supported by JHU/APL subcontract 131803 to the NJIT under NASA

1159 Prime contract NNN06AA01C. EMFISIS work was supported by JHU/APL contract
1160 no. 921647 under NASA Prime contract No. NAS5-01072. The MagEIS instrument
1161 was funded by NASA's Prime contract no. NAS5-01072. The level 3 MagEIS-A
1162 "high rate" data is available in the Supporting Information, level 1 RBSPICE EBR
1163 data is archived at <http://rbspicea.ftecs.com/>, and the EMFISIS level 2 spectral
1164 matrix and burst data as well as the level 3 magnetometer data is archived at
1165 <http://emfisis.physics.uiowa.edu/data/index>. The IRBEM Library can be obtained
1166 at irbem.sf.net.

1167

CHAPTER THREE

1168

MICROBURST SCALE SIZE DERIVED FROM MULTIPLE BOUNCES OF A

1169

MICROBURST SIMULTANEOUSLY OBSERVED WITH THE FIREBIRD-II

1170

CUBESATS

1171

Contribution of Authors and Co-Authors

1172

Manuscript(s) in Chapter(s) 1

1173

1174 Author: [type author name here]

1175 Contributions: [list contributions here, single-spaced]

1176 Co-Author: [type co-author name here]

1177 Contributions: [list contributions here, single-spaced]

1178 Co-Author: [type co-author name here]

1179 Contributions: [list contributions here, single-spaced]

1180

1181

Manuscript Information

1182 [Type Author and Co-author(s) Names Here]

1183 Geophysical Research Letters

1184 Status of Manuscript: Published in a peer-reviewed journal

1185 Wiley

1186 Volume 45, Issue 17

1187

1188 This article is available under the terms of the Creative Commons Attribution
1189 Non-Commercial No Derivatives License CC BY-NC-ND (which may be updated
1190 from time to time) and permits non-commercial use, distribution, and reproduction
1191 in any medium, without alteration, provided the original work is properly cited and
1192 it is reproduced verbatim.

1193

Key Points

1194

- Multiple bounces from a microburst were observed by the two FIREBIRD-II CubeSats at LEO.
- The lower bounds on the microburst scale size at LEO were 29 ± 1 km (latitudinal) and 51 ± 11 km (longitudinal).
- Deduced lower bound equatorial scale size was similar to the whistler-mode chorus source scale.

1200

Abstract

1201

We present the observation of a spatially large microburst with multiple bounces made simultaneously by the FIREBIRD-II CubeSats on February 2nd, 2015. This is the first observation of a microburst with a subsequent decay made by two co-orbiting but spatially separated spacecraft. From these unique measurements, we place estimates on the lower bounds of the spatial scales as well as quantify the electron bounce periods. The microburst's lower bound latitudinal scale size was 29 ± 1 km and the longitudinal scale size was 51 ± 1 km in low earth orbit. We mapped these scale sizes to the magnetic equator and found that the radial and azimuthal scale sizes were at least 500 ± 10 km and 530 ± 10 km, respectively. These lower bound equatorial scale sizes are similar to whistler-mode chorus wave source scale sizes, which supports the hypothesis that microbursts are a product of electron scattering by chorus waves. Lastly, we estimated the bounce periods for 200-800 keV electrons and found good agreement with four common magnetic field models.

1214

Introduction

1215 The dynamics of radiation belt electrons are complex, and are driven by
 1216 competition between source and loss processes. A few possible loss processes are
 1217 radial diffusion (Shprits and Thorne, 2004), magnetopause shadowing (Ukhorskiy
 1218 et al., 2006), and pitch angle and energy diffusion due to scattering of electrons by
 1219 plasma waves (e.g. Abel and Thorne, 1998; Horne and Thorne, 2003; Meredith et al.,
 1220 2002; Mozer et al., 2018; Selesnick et al., 2003; Summers et al., 1998; Thorne et al.,
 1221 2005). There are a variety of waves that cause pitch angle scattering, including
 1222 electromagnetic ion cyclotron waves, plasmaspheric hiss, and chorus (Millan and
 1223 Thorne, 2007; Thorne, 2010). Chorus predominantly occurs in the dawn sector (6-12
 1224 magnetic local times (MLT)) (Li et al., 2009b) where it accelerates electrons with
 1225 large equatorial pitch angles and scatters electrons with small equatorial pitch angles
 1226 (Horne and Thorne, 2003). Some of these electrons may be impulsively scattered
 1227 into the loss cone, where they result in short-duration (~ 100 ms) enhancements in
 1228 precipitating flux called microbursts.

1229 Anderson and Milton (1964) coined the term microburst to describe high altitude
 1230 balloon observations of ~ 100 ms duration enhancements of bremsstrahlung X-
 1231 rays emitted from scattered microburst electrons impacting the atmosphere. Since
 1232 then, non-relativistic (less than a few hundred keV) microbursts have been routinely
 1233 observed with other balloon missions (e.g. Anderson et al., 2017; Parks, 1967; Woodger
 1234 et al., 2015). A review of the literature shows no reports of microbursts above a few
 1235 hundred keV observed by balloons (Millan et al., 2002; Woodger et al., 2015). This
 1236 lack of observation may be explained by relatively weaker pitch angle scattering of
 1237 relativistic electrons by chorus (Lee et al., 2012).

1238 In addition to the X-ray signature for bursts of electron precipitation, the

1239 precipitating relativistic and non-relativistic electrons have been measured in situ by
 1240 spacecraft orbiting in low earth orbit (LEO). Hereinafter, we refer to these electron
 1241 signatures observed by LEO spacecraft also as microbursts. Microbursts have been
 1242 observed with, e.g. the Solar Anomalous and Magnetospheric Particle Explorer's
 1243 (SAMPEX) \gtrsim 150 keV and \gtrsim 1 MeV channels (Blake et al., 1996; Blum et al., 2015;
 1244 Lorentzen et al., 2001a,b; Nakamura et al., 1995, 2000; O'Brien et al., 2004, 2003) and
 1245 Focused Investigation of Relativistic Electron Bursts: Intensity, Range, and Dynamics
 1246 (FIREBIRD-II) with its \gtrsim 200 keV energy channels (Anderson et al., 2017; Breneman
 1247 et al., 2017; Crew et al., 2016).

1248 Understanding microburst precipitation and its scattering mechanism is impor-
 1249 tant to radiation belt dynamics. The scattering mechanism has been observationally
 1250 studied by e.g. Lorentzen et al. (2001b) who found that microbursts and chorus
 1251 waves predominantly occur in the dawn sector and Breneman et al. (2017) made
 1252 a direct observational link between individual microbursts and chorus elements.
 1253 Microbursts have been modeled and empirically estimated to be capable of depleting
 1254 the relativistic electron population in the outer radiation belt on the order of a day
 1255 (Breneman et al., 2017; O'Brien et al., 2004; Shprits et al., 2007; Thorne et al., 2005).
 1256 An important parameter in this estimation of instantaneous radiation belt electron
 1257 losses due to microbursts is their scale size. Parks (1967) used balloon measurements
 1258 of bremsstrahlung X-rays to estimate the high altitude scale size of predominantly low
 1259 energy microbursts to be 40 ± 14 km. In Blake et al. (1996) a microburst with multiple
 1260 bounces was observed by SAMPEX, and the microburst's latitudinal scale size in LEO
 1261 was estimated to have been "at least a few tens of kilometers". Blake et al. (1996)
 1262 concluded that typically microbursts are less than a few tens of electron gyroradii in
 1263 size (at $L = 5$ at LEO, the gyroradii of 1 MeV electrons is on the order of 100 m).
 1264 Dietrich et al. (2010) used SAMPEX along with ground-based very low frequency

1265 stations to conclude that during one SAMPEX pass, the observed microbursts had
1266 scale sizes less than 4 km.

1267 Since February 1st, 2015, microbursts have been observed by FIREBIRD-II, a
1268 pair of CubeSats in LEO. Soon after launch, when the two FIREBIRD-II spacecraft
1269 were at close range, a microburst with a scale size greater than 11 km was observed
1270 (Crew et al., 2016). On the same day, FIREBIRD-II simultaneously observed a
1271 microburst with multiple bounces. The microburst decay was observed over a period
1272 of a few seconds, while the spacecraft were traveling predominantly in latitude. Here
1273 we present the analysis and results of the latitude and longitude scale sizes and
1274 bounce periods of the first microburst with multiple bounces observed with the two
1275 FIREBIRD-II spacecraft.

1276 Spacecraft and Observation

1277 The FIREBIRD missions are comprised of a pair of identically-instrumented
1278 1.5U CubeSats (15 x 10 x 10 cm) that are designed to measure electron precipitation
1279 in LEO (Klumpar et al., 2015; Spence et al., 2012). The second mission, termed
1280 FIREBIRD-II, was launched on January 31st 2015. The two FIREBIRD-II CubeSats,
1281 identified as Flight Unit 3 (FU3) and Flight Unit 4 (FU4), were placed in a 632 km
1282 apogee, 433 km perigee, and 99° inclination orbit (Crew et al., 2016). FU3 and FU4
1283 are orbiting in a string of pearls configuration with FU4 ahead, to resolve the space-
1284 time ambiguity of microbursts. Each FIREBIRD-II unit has two solid state detectors:
1285 one is mounted essentially at the spacecraft surface, covered only by a thin foil acting
1286 as a sun shade, with a field of view of 90° (surface detector), and the other is beneath
1287 a collimator which restricts the field of view to 54° (collimated detector). Only FU3
1288 has a functioning surface detector, so this analysis utilizes the collimated detectors.
1289 FU3's surface and collimated detectors, as well as FU4's collimated detector observe

1290 electron fluxes in six energy channels from ~ 230 keV to > 1 MeV. FIREBIRD-II's
 1291 High Resolution (HiRes) electron flux data is gathered with an adjustable sampling
 1292 period of 18.75 ms by default and can be as fast as 12.5 ms.

1293 On February 2nd, 2015 at 06:12 UT, both FIREBIRD-II spacecraft simulta-
 1294 neously observed an initial microburst, followed by subsequent periodic electron
 1295 enhancements of diminishing amplitude shown in Fig. 3.1. This is thought to be
 1296 the signature of a single burst of electrons, some of which precipitate, but the rest
 1297 mirror near the spacecraft then bounce to the conjugate hemisphere where they mirror
 1298 again and the subsequent bounces produce a train of decaying peaks (Blake et al.,
 1299 1996; Thorne et al., 2005). This bounce signature occurred during the transition
 1300 between the main and recovery phases of a storm with a minimum Dst of -44 nT
 1301 ($K_p = 4$, and $AE \approx 400$ nT). At this time, the HiRes data was sampled at 18.75 ms.
 1302 Five peaks were observed by both spacecraft. The fifth peak observed by FU4 was
 1303 comparable to the Poisson noise and was not used in this analysis. This microburst
 1304 was observed from the first energy channel ($\approx 200 - 300$ keV), to the fourth energy
 1305 channel ($\approx 500 - 700$ keV), and FU3's surface detector observed the microburst up
 1306 to the fifth energy channel (683 - 950 keV).

1307 The HiRes data in Fig. 3.1 shows signs of energy dispersion, characterized by
 1308 higher energy electrons arriving earlier than the lower energies. This time of flight
 1309 energy dispersion tends to smear out the initial sharp burst upon each subsequent
 1310 bounce. The first peak does not appear to be dispersed, and subsequent peaks show
 1311 a dispersion trend consistent across energy channels. The black vertical bars have
 1312 been added to Fig. 3.1 to highlight this energy dispersion. This dispersion signature
 1313 and amplitude decay implies that the first peak was observed soon after the electrons
 1314 were scattered, followed by decaying bounces.

1315 At this time, in magnetic coordinates, FIREBIRD-II was at McIlwain $L = 4.7$

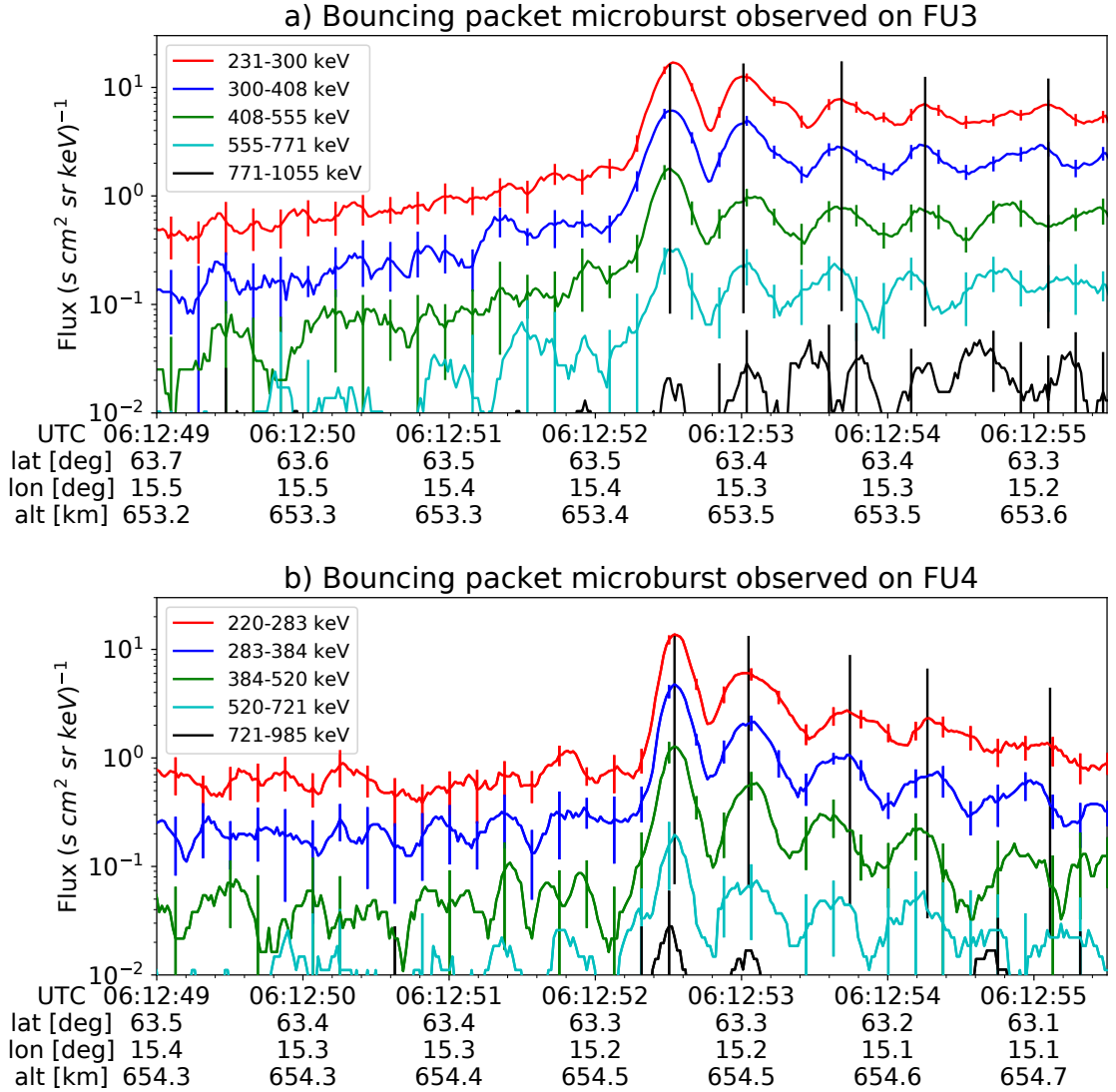


Figure 3.1: HiRes data of the microburst observed at February 2nd, 2015 at 06:12:53 UT, smoothed with a 150 ms rolling average. The subsequent bounces showed some energy dispersion. As discussed in Appendix B, a time correction of -2.28 s was applied to FU3. While the flux from five energy channels is shown, only channels with reasonable counting statistics were used for the spatial scale analysis. Vertical colored bars show the \sqrt{N} error every 10th data point and vertical black bars are lined up with the peaks in the 220-283 keV energy channel to help identify dispersion.

1316 and MLT = 8.3, calculated with the Tsyganenko 1989 (T89) magnetic field model
 1317 (Tsyganenko, 1989) using IRBEM-Lib (Boscher et al., 2012). Geographically, they
 1318 were above Sweden, latitude = 63°N, longitude = 15°E, altitude = 650 km. This
 1319 geographic location is magnetically conjugate to the east of the so-called South
 1320 Atlantic Anomaly (SAA). The SAA is the location where the mirror points of electrons
 1321 tend to occur at locations deeper in the atmosphere owing to the offset of the
 1322 dipole magnetic field from the Earth's center. Electrons with pitch angles within the
 1323 drift loss cone (DLC) will encounter the SAA and be removed from their eastward
 1324 longitudinal drift paths (Comess et al., 2013; Dietrich et al., 2010). FU3 and FU4 are
 1325 therefore both in regions where the particles in the DLC have recently precipitated,
 1326 leaving only particles that were recently scattered. At the spacecraft location, locally
 1327 mirroring electrons would have mirrored at 95 km in the opposite hemisphere, with
 1328 more field aligned electrons mirroring at even lower altitudes. From the analysis done
 1329 by Fang et al. (2010), the peak in the total ionization rate in the atmosphere for 100
 1330 keV electrons is around 80 km altitude, while the total ionization rate from 1 MeV
 1331 electrons peaks around 60 km altitude. It is, therefore, expected that a fraction of the
 1332 microburst electrons will survive each encounter with the atmosphere. By plotting
 1333 the peak flux as a function of bounce (not shown), it was found that 40 - 60 % of the
 1334 microburst electrons were lost on the first bounce, similar to the 33% loss per bounce
 1335 observed for a bouncing microburst observed by SAMPEX (Thorne et al., 2005).

1336

Analysis

1337 At the beginning of the FIREBIRD-II mission, two issues prevented the proper
 1338 analysis of the microburst's spatial scale size: the spacecraft clocks were not
 1339 synchronized, and their relative positions were not accurately known. We addressed
 1340 these issues with a cross-correlation time lag analysis described in detail in Appendix

1341 B. From this analysis, the time correction was 2.28 ± 0.12 s (applied to Fig. 3.1) and
 1342 the separation was 19.9 ± 0.9 km at the time of the microburst observation.

1343 Electron Bounce Period

1344 We used this unique observation of bouncing electrons to calculate the bounce
 1345 period, t_b as a function of energy and compare it to the energy-dependent t_b curves
 1346 derived from four magnetic field models, the results of which are shown in Fig. 3.2.
 1347 The observed t_b and uncertainties were calculated by fitting the baseline-subtracted
 1348 HiRes flux. The baseline flux used in this analysis is given in O'Brien et al. (2004)
 1349 as the flux at the 10th percentile over a specified time interval, which in this analysis
 1350 was taken to be 0.5 seconds. The flux was fitted with a superposition of Gaussians
 1351 for each energy channel, and the uncertainty in flux was calculated using the Poisson
 1352 error from the microburst and baseline fluxes summed in quadrature. Using the fit
 1353 parameters, the mean t_b for the lowest four energy channels is shown in Fig. 3.2. The
 1354 trend of decreasing t_b as a function of energy is evident in Fig. 3.2, which further
 1355 supports the assumption that the subsequent peaks are bounces, and not a train of
 1356 microbursts scattered by bouncing chorus.

1357 The decaying peaks in the 231-408 keV electron flux observed by FU3's lowest
 1358 two energy channels (see Fig. 3.1) were right-skewed. One explanation is that there
 1359 was in-channel energy dispersion within those channels. Since t_b of higher energy
 1360 electrons is shorter, a right-skewed peak implies that higher energy electrons were
 1361 more abundant within that channel e.g. in FU3's 231-300 keV channel, the 300 keV
 1362 electrons will arrive sooner than the 231 keV electrons, but will they will be binned
 1363 in the same channel. A Gaussian fit cannot account for this in-channel dispersion,
 1364 and as a first order correction, minima between peaks was used to calculate t_b , and
 1365 is shown in Fig. 3.2. The observed energy-dependent dispersion shown in Fig. 3.2

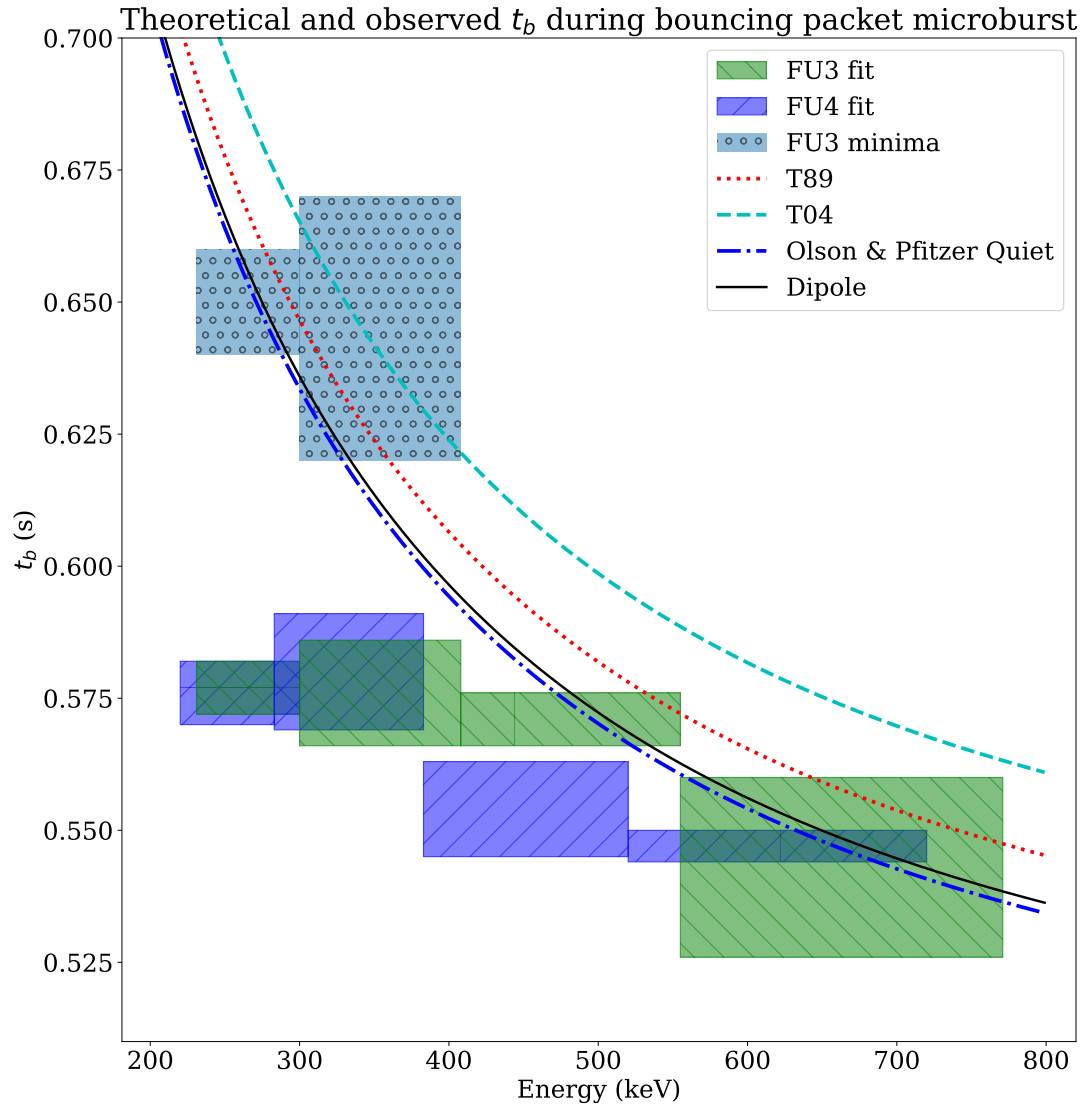


Figure 3.2: Observed and theoretical t_b for electrons of energies from 200 to 770 keV. The solid black line is t_b in a dipole magnetic field, derived in Schulz and Lanzerotti (1974). The red dotted and cyan dashed lines are the t_b derived using the T89, and T04 magnetic field models with IRBEM-Lib. Lastly, the blue dot-dash curve is the t_b derived using the Olson & Pfitzer Quiet model. The green and purple rectangles represent the observed t_b for FU3 and FU4 using a Gaussian fit, respectively. The blue rectangles represent the observed t_b calculated with the minima between the bounces. The width of the boxes represent the width of those energy channels, and the height represents the uncertainty from the fit.

1366 is consistent with higher energy peaks returning sooner. This dispersion consistency
 1367 further supports the assumption that the subsequent peaks are bounces, and not a
 1368 train of microbursts scattered by bouncing chorus.

1369 To compare the observed and modeled t_b , we superposed t_b curves for various
 1370 models including an analytical solution in a dipole (Schulz and Lanzerotti, 1974), and
 1371 numerical models: T89, Tsyganenko 2004 (T04) (Tsyganenko and Sitnov, 2005), and
 1372 Olson & Pfitzer Quiet (Olson and Pfitzer, 1982) in Fig. 3.2. The numerical t_b curves
 1373 were calculated using a wrapper for IRBEM-Lib. This code traces the magnetic field
 1374 line between mirror points, and calculates t_b assuming conservation of energy and the
 1375 first adiabatic invariant for electrons mirroring at FIREBIRD-II. With the empirical
 1376 t_b , the models agree within FIREBIRD-II's uncertainties, but the T04 model has the
 1377 largest discrepancy compared to the other models.

1378 Microburst Energy Spectra

1379 Next, we investigated the energy spectra of this microburst. The energy spectra
 1380 was modeled with an exponential that was fit to the peak flux derived from the
 1381 Gaussian fit parameters in section 3 to all but the highest energy channel. We found
 1382 that the E-folding energy, $E_0 \sim 100$ keV. This spectra is similar to spectra show
 1383 by Lee et al. (2005) from STSAT-1 and Datta et al. (1997) from sounding rocket
 1384 measurements. The energy spectra is soft for a typical microburst observed with
 1385 FIREBIRD-II and there was no statistically significant change in E_0 for subsequent
 1386 bounces.

1387 Microburst Scale Sizes

1388 Lastly, after we applied the time and separation corrections detailed in Appendix
 1389 B, we mapped the locations of FU3 and FU4 in Fig. 3.3. The locations where FU3 saw
 1390 peaks 1-5 and where FU4 saw peaks 1-4 are shown as P1-5 and P1-4, respectively.

1391 The lower bound on the latitudinal extent of the microburst was the difference in
 1392 latitude between P1 on FU3 and P4 on FU4 and was found to be 29 ± 1 km. The
 1393 uncertainty was estimated from the spacecraft separation uncertainty described in
 1394 Appendix B. This scale size is the largest reported by FIREBIRD-II.

1395 In section 3, we showed that the observed decaying peaks were likely due to
 1396 bouncing, so we assume that the observed electrons in subsequent bounces were the
 1397 drifted electrons from the initial microburst. Under this assumption, the scattered
 1398 electrons observed in the last bounce by FIREBIRD-II, must have drifted east from
 1399 their initial scattering longitude, allowing us to calculate the minimum longitudinal
 1400 scale size. Following geometrical arguments, the distance that electrons drift east in
 1401 a single bounce is a product of the circumference of the drift shell foot print, and the
 1402 fraction of the total drift orbit traversed in a single bounce and is given by,

$$d_{az} = 2\pi(R_E + A) \cos(\lambda) \frac{t_b}{\langle T_d \rangle} \quad (3.1)$$

where R_E is the Earth's radius, A is the spacecraft altitude, λ is the magnetic latitude,
 t_b is the electron bounce period, and $\langle T_d \rangle$ is the electron drift period. Parks (2003)
derived $\langle T_d \rangle$ to be,

$$\langle T_d \rangle \approx \begin{cases} 43.8/(L \cdot E) & \text{if } \alpha_0 = 90^\circ \\ 62.7/(L \cdot E) & \text{if } \alpha_0 = 0^\circ \end{cases} \quad (3.2)$$

1403 where E is the electron energy in MeV, L is the L shell, and α_0 is the equatorial pitch
 1404 angle. Electrons mirroring at FIREBIRD-II have $\alpha_0 \approx 3.7^\circ$ and so the $\alpha_0 = 0^\circ$ limit
 1405 was used.

1406 The microburst's longitudinal scale size is defined as the distance the highest
 1407 energy electrons drifted in the time between the observations of the first and last
 1408 peaks. This scale size is given by $D_{az} = n d_{az}$ where n is the number of bounces

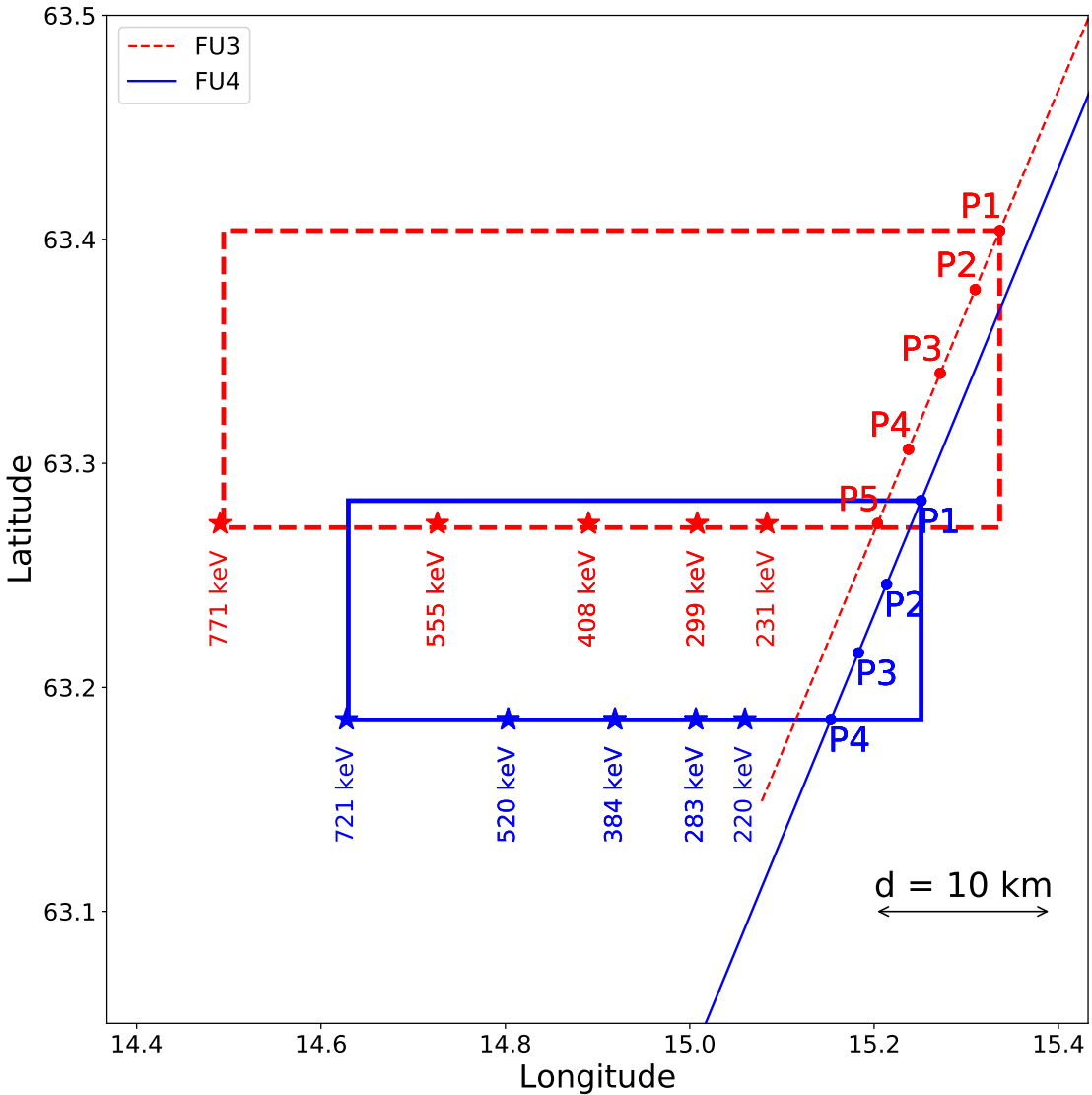


Figure 3.3: The topology of the FIREBIRD-II orbit and the multiple bounces of the microburst projected onto latitude and longitude with axis scaled to equal distance. Attributes relating to FU3 shown in red dashed lines, and FU4 with blue solid lines. The spacecraft path is shown with the diagonal lines, starting at the upper right corner. The labels P1-4 for FU4 and P1-5 for FU3 indicate where the spacecraft were when the N^{th} peak was seen in the lowest energy channel in the HiRes data. The stars with the accompanying energy labels represent the locations of the electrons with that energy that started at time of P1, and were seen at the last peak on each spacecraft. The rectangles represent the lower bound of the microburst scale size, assuming that the majority of the electrons were in the upper boundary of energy channel 4.

1409 observed. The stars in Fig. 3.3 (with labels corresponding to energy channel
 1410 boundaries) represent the locations when the microburst was observed at P1, such
 1411 that an electron of that energy would drift eastward to be seen at P5 for FU3 and P4
 1412 for FU4. Since FU3 observed more peaks it observed the larger longitudinal scale size
 1413 which is shown with the red dashed box in Fig. 3.3. FU3’s fourth energy channel’s
 1414 bounds are 555 keV and 771 keV, which correspond to longitudinal distances of 39 ± 1
 1415 km and 51 ± 1 , respectively. The uncertainty was estimated by propagating the
 1416 uncertainty in the bounce time Eq. 3.1. While the observed minimum longitudinal
 1417 scale size is dependent on FIREBIRD-II’s energy channels, the true scale size may
 1418 not be.

1419 To investigate how the microburst scale size compares to the scale sizes of chorus
 1420 waves near the magnetic equator, the microburst’s longitudinal and latitudinal scale
 1421 sizes and their uncertainties in LEO were mapped to the magnetic equator with T89.
 1422 The radial scale size (latitudinal scale mapped from LEO) was greater than 500 ± 10
 1423 km. The azimuthal scale size (longitudinal scale mapped from LEO) of 555 keV
 1424 electrons was greater than 450 ± 10 km and for the 771 keV electrons it was greater
 1425 than 530 ± 10 km. The lower bound microburst scale size is similar to the chorus
 1426 scale sizes derived by Agapitov et al. (2017, 2011), and is discussed below.

1427 Discussion and Conclusions

1428 We presented the first observation of a large microburst with multiple bounces
 1429 made possible by the twin FIREBIRD-II CubeSats. The microburst’s lower bound
 1430 LEO latitudinal and longitudinal scale sizes of 29 ± 1 km and 51 ± 1 km make
 1431 it one of the largest observed. The microburst’s LEO scale size was larger than
 1432 the latitudinal scale sizes of typical > 1 MeV microbursts reported in Blake et al.
 1433 (1996), approximately 10 times larger than reported in Dietrich et al. (2010), and

1434 approximately 2.6 times larger than other simultaneous microbursts observed by
 1435 FIREBIRD-II (Crew et al., 2016). Lastly, the scale sizes derived here were similar to
 1436 the scale sizes of \gtrsim 15 keV microbursts observed with a high altitude balloon (Parks,
 1437 1967). No energy dependence on the minimum latitudinal scale size was observed,
 1438 while the observed energy dependence of the minimum longitudinal scale size is an
 1439 artifact of the technique we used to estimate their drift motion.

1440 The microburst scale size obtained in Section 3 and scaled to the geomagnetic
 1441 equator can be compared with the scales of chorus waves presumably responsible for
 1442 the rapid burst electron precipitation. Early direct estimates of the chorus source
 1443 scales were made by the coordinated measurement by ISEE-1, 2. The wave power
 1444 correlation scale was estimated to be about several hundred kilometers across the
 1445 background magnetic field (Gurnett et al., 1979). Furthermore, Santolik et al. (2003)
 1446 determined the correlation lengths of chorus-type whistler waves to be around 100
 1447 km based on multipoint CLUSTER Wide Band Data measurements near the chorus
 1448 source region at $L \approx 4$, during the magnetic storm of 18 April 2002. Agapitov et al.
 1449 (2017, 2011, 2010) recently showed that the spatial extent of chorus source region can
 1450 be larger, ranging from 600 km in the outer radiation belt to more than 1000 km in
 1451 the outer magnetosphere. The lower bound azimuthal and latitudinal scales obtained
 1452 in Section 3 and scaled to the magnetic equator, are similar to the whistler-mode
 1453 chorus source scale sizes reported in Agapitov et al. (2017, 2011).

1454 No wave measurements from nearby spacecraft were available at this time.
 1455 Nevertheless, during the hours before and after this observation, the Van Allen Probes'
 1456 (Mauk et al., 2013) Electric and Magnetic Field Instrument and Integrated Science
 1457 (Kletzing et al., 2013) observed strong wave power in the lower band chorus frequency
 1458 range, inside the outer radiation belt between 22 and 2 MLT. Furthermore, AE ~ 400
 1459 nT at this time, and relatively strong chorus waves were statistically more likely to

¹⁴⁶⁰ be present at FIREBIRD-II's MLT (Li et al., 2009b).

¹⁴⁶¹ The empirically estimated and modeled t_b in this study agree within FIREBIRD-
¹⁴⁶² II's uncertainties, confirming that the energy-dependent dispersion was due to
¹⁴⁶³ bouncing. The t_b curves are a proxy for field line length, and this agreement implies
¹⁴⁶⁴ that they are comparable. This is expected since the magnetosphere is not drastically
¹⁴⁶⁵ compressed at 8 MLT, but we expect a larger discrepancy near midnight, where the
¹⁴⁶⁶ magnetosphere is more stretched and difficult to accurately model. In future studies,
¹⁴⁶⁷ this analysis can be used as a diagnostic tool to validate field line lengths, and improve
¹⁴⁶⁸ magnetic field models.

¹⁴⁶⁹ The similarity of the microburst and chorus source region scale sizes, as well
¹⁴⁷⁰ as magnetospheric location and conditions, further support the causal relationship
¹⁴⁷¹ between microbursts and chorus.

¹⁴⁷²

Acknowledgments

¹⁴⁷³ This work was made possible with help from the FIREBIRD team, and the
¹⁴⁷⁴ members of the Space Sciences and Engineering Laboratory at Montana State
¹⁴⁷⁵ University for their hard work to make this mission a success. In addition, M.
¹⁴⁷⁶ Shumko acknowledges Drew Turner for his suggestions regarding the bounce period
¹⁴⁷⁷ calculations, and Dana Longcope for his proofreading feedback. The FIREBIRD-II
¹⁴⁷⁸ data are available at http://solar.physics.montana.edu/FIREBIRD_II/. This analysis
¹⁴⁷⁹ is supported by the National Science Foundation under Grant Numbers 0838034 and
¹⁴⁸⁰ 1339414. Furthermore, the work of O. Agapitov was supported by the NASA grant
¹⁴⁸¹ NNX16AF85G.

1482

CHAPTER FOUR

1483

MICROBURST SIZE DISTRIBUTION DERIVED WITH AEROCUBE-6

1484

Contribution of Authors and Co-Authors

1485 Manuscript(s) in Chapter(s) 1

1486

1487 Author: [type author name here]

1488 Contributions: [list contributions here, single-spaced]

1489 Co-Author: [type co-author name here]

1490 Contributions: [list contributions here, single-spaced]

1491 Co-Author: [type co-author name here]

1492 Contributions: [list contributions here, single-spaced]

1493

1494

Manuscript Information

1495 [Type Author and Co-author(s) Names Here]

1496 Journal of Geophysical Research

1497 Status of Manuscript: **Officially submitted to a peer-reviewed journal**

1498 Wiley

1499

1500

Key Points

1501

- The dual AeroCube-6 CubeSats simultaneously observed > 35 keV microbursts at a variety of spatial separations ranging from 2 to ≈ 100 km.
- In low Earth orbit the majority of microbursts have a size on the order of a few tens of km.
- At the magnetic equator, the size of most microbursts corresponds to the size of whistler-mode chorus wave packets.

1507

Abstract

1508

Microbursts are an impulsive increase of electrons from the radiation belts into the atmosphere and have been directly observed in low Earth orbit and the upper atmosphere. Prior work has estimated that microbursts are capable of rapidly depleting the radiation belt electrons on the order of a day, hence their role to radiation belt electron losses must be considered. Losses due to microbursts are not well constrained, and more work is necessary to accurately quantify their contribution as a loss process. To address this question we present a statistical study of > 35 keV microburst sizes using the pair of AeroCube-6 CubeSats. The microburst size distribution in low Earth orbit and the magnetic equator was derived using both spacecraft. In low Earth orbit, the majority of microbursts were observed while the AeroCube-6 separation was less than a few tens of km, mostly in latitude. To account for the statistical effects of random microburst locations and sizes, a Monte Carlo and analytic models were developed to test hypothesized microburst size distributions. A family of microburst size distributions were tested and a Markov Chain Monte Carlo sampler was used to estimate the optimal distribution of the microburst size model

parameters. Finally, a majority of observed microbursts map to sizes less than 200 km at the magnetic equator. Since microburst are widely believed to be generated by scattering of radiation belt electrons by whistler mode waves, the observed microburst size correlates to coherent whistler mode chorus sizes derived in prior literature.

1527

Introduction

Since the discovery of the Van Allen radiation belts in the 1960s by Van Allen (1959) and Vernov and Chudakov (1960), decades of research has made headway in understanding the various particle acceleration and loss mechanisms. One of the extensively studied mechanisms responsible for both acceleration and loss is wave-particle scattering between whistler-mode chorus waves and electrons (Abel and Thorne, 1998; Bortnik et al., 2008; Horne and Thorne, 2003; Meredith et al., 2002; Millan and Thorne, 2007; Thorne et al., 2005). Whistler-mode chorus waves are typically generated by a temperature anisotropy of low energy electrons up to tens of kiloelectronvolts (keV) and are typically found in the $\sim 0 - 12$ magnetic local times (MLT) (Li et al., 2009a,b). Whistler-mode chorus waves interact with radiation belt electrons, and are widely believed to cause electron precipitation termed microbursts (e.g. Millan and Thorne, 2007).

Microbursts are a subsecond impulse of electrons that are observed by high altitude balloons and satellites in low Earth orbit (LEO) on radiation belt magnetic footprints $\sim 4 - 8$ L-shell (L) (e.g. Anderson and Milton, 1964; Breneman et al., 2017; Crew et al., 2016; Greeley et al., 2019; Lorentzen et al., 2001a; Mozer et al., 2018; O'Brien et al., 2003; Tsurutani et al., 2013; Woodger et al., 2015), mostly in the dawn MLTs, and with an enhanced occurrence rate during disturbed magnetospheric times (Douma et al., 2017; O'Brien et al., 2003). Microburst's role as a radiation belt electron loss mechanism has been estimated to be significant, with total radiation belt

1548 electron depletion due to microbursts estimated to be on the order of a day (Breneman
 1549 et al., 2017; Lorentzen et al., 2001b; O'Brien et al., 2004; Thorne et al., 2005). These
 1550 average microburst loss estimates are not well constrained due to assumptions made
 1551 regarding the microburst precipitation region.

1552 One of the unconstrained microburst parameters that is critical to better
 1553 quantify the role of microbursts as an instantaneous loss mechanism (the number
 1554 of electrons lost per microburst) is their physical size. Historically, after the
 1555 bremsstrahlung X-ray signatures of microbursts were discovered by Anderson and
 1556 Milton (1964), numerous microburst size studies were done using other balloon flights
 1557 in the mid 1960s. Brown et al. (1965) used data from a pair of balloons separated
 1558 by 150 km, mainly in longitude, and found that one third of all microbursts observed
 1559 were temporally coincident. Trefall et al. (1966) then used the results from Brown
 1560 et al. (1965) to model the probability that a microburst will be observed by two
 1561 balloons as a function of the radius of the microburst, radius of the precipitating area
 1562 a balloon is sensitive to, and the balloon separation. Trefall et al. (1966) concluded
 1563 that the microbursts reported by Brown et al. (1965) must have had a diameter of
 1564 230 km assuming a balloon has a circular field of view with a 140 km diameter (for
 1565 electrons stopped at 100 km altitudes). Soon after, Barcus et al. (1966) used a pair of
 1566 balloons and concluded that a microburst must have a < 200 km longitudinal extent.
 1567 Then Parks (1967) used data from a single balloon with four collimated scintillators
 1568 oriented in different directions and found that the size of some mostly low energy
 1569 microbursts to have a diameter of 80 ± 28 km, and others were less than 40 km.

1570 Direct observations of microburst electrons are made by LEO spacecraft. Blake
 1571 et al. (1996) found a microburst with a size of a few tens of km using the the Solar
 1572 Anomalous and Magnetospheric Particle Explorer (SAMPEX) and concluded that
 1573 typically microbursts are less than a few tens of electron gyroradii in size (order of

1574 a few km in LEO). Recently, Dietrich et al. (2010) used SAMPEX observations in
1575 another case study and concluded that the observed microbursts were smaller than 4
1576 km. Crew et al. (2016) used the Focused Investigation of Relativistic Electron Bursts:
1577 Intensity, Range, and Dynamics (FIREBIRD-II) CubeSats and found an example of
1578 a microburst larger than 11 km. Lastly, Shumko et al. (2018) also used FIREBIRD-II
1579 to identify a microburst with a size greater than 51 ± 1 km. If anything, the large
1580 variance in prior results imply that there is a distribution of microburst scale sizes
1581 which this study aims to estimate.

1582 Besides addressing the instantaneous radiation belt electron losses due to
1583 individual microbursts, the microburst size distribution is useful to identify the wave
1584 mode(s) responsible for scattering microbursts. By mapping the microburst size
1585 distribution in LEO to the magnetic equator it can be compared to the wave sizes
1586 estimated in prior literature. This comparison can be used to identify the waves and
1587 their properties (e.g. amplitude or coherence) responsible for scattering microburst
1588 electrons.

1589 This paper addresses these two questions by expanding the prior microburst
1590 size case studies by analyzing microburst observations over a three year time period
1591 to estimate the microburst size distribution in LEO and the magnetic equator. The
1592 twin AeroCube-6 (AC6) CubeSats are utilized for this study because they were ideally
1593 equipped to observe microbursts simultaneously over a span of three years while their
1594 total separation varied between 2 and 800 km, mostly in latitude (in-track in orbit).
1595 This paper first describes the AC-6 mission, including their orbit and instrumentation
1596 in section 4. Section 4 develops the methodology used to identify microbursts observed
1597 by each spacecraft and how they were combined to make a list of simultaneously
1598 observed microbursts. Section 4 describes the methodology used to estimate the
1599 microburst size distributions in LEO and the magnetic equator as a function of AC6

1600 separation. Then a model is developed to shed light on how the compounding effects of
 1601 a hypothesized microburst shape, size distribution, and random microburst locations
 1602 will be observed by AC6, a two-point measurement platform. Lastly, in section 4
 1603 we discuss these results and compare the microburst sizes estimated here to the size
 1604 distribution of the whistler-mode chorus waves that are believed to cause microbursts.

1605

Instrumentation

1606 The AC6 mission consists of a pair of 0.5U (10x10x5 cm) CubeSats built by
 1607 The Aerospace Corporation and launched on June 19th, 2014 into a 620 x 700 km,
 1608 98° inclination orbit. The two satellites, designated as AC6-A and AC6-B, separated
 1609 after launch and drifted apart. Both AC6 units have an active attitude control system
 1610 which allows them to adjust the atmospheric drag experienced by each AC6 unit by
 1611 orienting their solar panel “wings” with respect to the ram direction. By changing
 1612 their orientation, AC6 was able to achieve fine separation control and maintain a
 1613 separation between 2-800 km. Figure 4.1a shows the AC6 separation for the duration
 1614 of the mission. Figure 4.1b shows where AC6 was taking 10 Hz data simultaneously
 1615 as a function of L and MLT which highlights that most data was taken at 8-12 MLT,
 1616 an ideal local time for observing microbursts. Lastly Fig. 4.1b shows that the AC6
 1617 orbit was roughly dawn-dusk, sun-synchronous and precessed only a few hours in
 1618 MLT over a three year period.

1619 Each AC6 unit is equipped with three Aerospace microdosimeters (licensed to
 1620 Teledyne Microelectronics, Inc). The dosimeter used for this study is dos1 and is
 1621 identical on both AC6 units. Dos1 has a 35 keV electron threshold and all dosimeters
 1622 sample at 1 Hz in survey mode, and 10 Hz in burst mode in the radiation belts. More
 1623 detailed technical information on AC6 is described in O’Brien et al. (2016b).

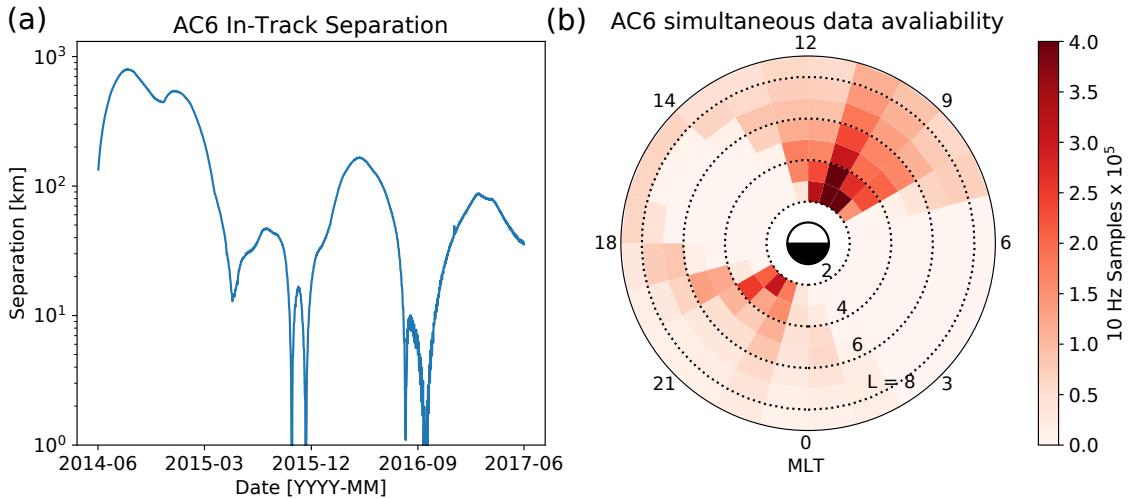


Figure 4.1: AC6 mission properties for (a) spacecraft separation and (b) number of simultaneous quality 10 Hz samples as a function of L and MLT.

1624

Methodology

1625 Microburst Detection

1626 The first step to find microbursts observed simultaneously by AC6 is to identify
 1627 them on each individual spacecraft. Microbursts were detected with two different
 1628 methods that yielded quantitatively similar results. The first method is the burst
 1629 parameter (O'Brien et al., 2003). This algorithm has been successfully used in other
 1630 microburst studies, mainly with the microbursts observed by SAMPEX (e.g. Blum
 1631 et al., 2015; Douma et al., 2017; O'Brien et al., 2003). For AC6, a burst parameter
 1632 threshold of 5 was determined to be a good trade-off between false positive and false
 1633 negative microburst detections. Another microburst detection algorithm based on
 1634 wavelet spectra frequency filtering was developed and the resulting list of microbursts
 1635 is similar to the list from the burst parameter.

1636 With the two microburst detection lists in hand, data cleaning to remove
 1637 microburst-like transmitter noise was necessary. The transmitters on AC6 can

cause unphysical count impulses in the dosimeters that resembles periodic trains of microbursts. One source of transmitter noise was observed at times when AC6 was in contact with the ground stations above the US for data downloads and commanding, thus the microburst detections made above the US that were mostly at low L were discarded.

Another source of noise is crosslink transmissions between AC6-A and AC6-B. These transmissions occurred when either spacecraft transitioned from the survey mode to 10 Hz mode. This noise is sometimes not caught by the data quality flag, so the following empirically-derived criteria were developed to remove those detections. The dosimeter with a 250 keV nominal electron threshold, dos2, was used because it had a nearly identical response to noise while rarely responded to microbursts. Since the transmitter noise is very periodic with a ≈ 0.2 s period, cross-correlation (CC) and autocorrelation (AC) methods were applied to the dos1 and dos2 time series. Detections were discarded if the following two criteria were met: either dos1 or dos2 time series had a AC peak at a 0.2 or 0.4 s lag and the dos1-dos2 CC was greater than 0.9. The AC lag criteria alone sometimes falsely removed legitimate trains of microbursts, so the second criteria insured that the detection was removed if there was also an unphysically high correlation across an order of magnitude in energy.

The lists of microbursts observed individually by AC6 were then merged into a list of temporally correlated microbursts, i.e. microbursts that were observed simultaneously by both AC6 units, with the following procedure. The general idea is that a microburst detected by one spacecraft will cross-correlate well with the time series from the other spacecraft if it observed a similar microburst, and poorly if there was no microburst observed by the other spacecraft. Each microburst detection made by either spacecraft was cross-correlated with the time series from the other spacecraft whether or not a microburst was observed by the other spacecraft. Cross-

1664 correlation windows with 1 and 1.2 s widths were chosen with slightly different
 1665 window sizes to account for random count variation due to Poisson noise. Microbursts
 1666 detections that had a cross-correlation greater than 0.8 were considered temporally
 1667 coincident. This CC threshold was chosen as it is low enough to accept user-identified
 1668 temporally coincident microbursts superposed with noise, and high enough to reject
 1669 most non-coincident events. Figure 4.2, panels (a), (c), (e), and (g) show examples
 1670 of microbursts observed by both AC6 units when they were separated by 5, 16, 37,
 1671 and 69 km, respectively.

1672 The last criteria requires that the temporal CC must be greater than the spatial
 1673 CC + 0.3. The spatial CC was calculated by shifting one spacecraft's time series
 1674 by the in-track lag to cross-correlate in the same spatial location, i.e. latitude.
 1675 This criteria was applied to remove curtains, stationary structures observed by AC6
 1676 that are narrow in latitude (Blake and O'Brien, 2016) that can be misidentified as
 1677 microbursts. Figure 4.2, panels (b), (d), (f), and (h) show the shifted time series to
 1678 confirm that there were no spatially correlated, non-microburst structures present.
 1679 Lastly the merged microburst list was spot checked by two authors to remove poorly
 1680 correlated and any duplicate events. After filtering out transmitter noise and applying
 1681 the CC criteria, 662 simultaneous microburst detections were found and used in this
 1682 study.

1683 Microburst Size Distribution in LEO and Magnetic Equator

1684 The temporally coincident microbursts, which from now on will be referred to
 1685 as microbursts, are now used to estimate the fraction of microbursts observed above
 1686 AC6 separation, s . When AC6 observes a microburst at s , the microburst's size
 1687 must be greater than s . This fact, along with the arguments presented in Section 4
 1688 in Joy et al. (2002) who studied the most probable Jovian magnetopause and bow

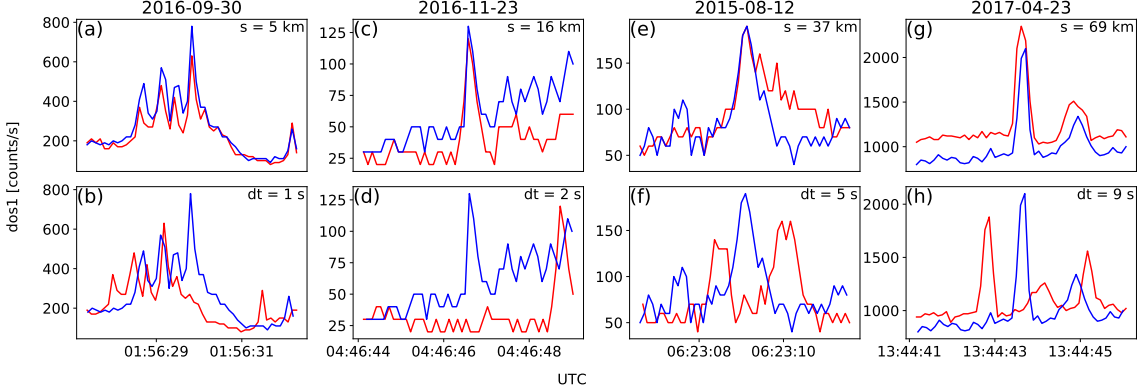


Figure 4.2: Examples of > 35 keV microbursts observed simultaneously by AC6-A in red and AC6-B in blue. Panels (a), (c), (e), and (g) show the temporally-aligned time series when AC6 were separated by $s = 5, 16, 37$, and 69 km, respectively. The corresponding panels (b), (d), (f), and (h) show the spatially-aligned time series which is made by shifting the AC6-A time series in the above panels by the in-track lag (annotated with dt) that show any spatially correlated structures. The clear temporal correlation and lack of spatial correlation demonstrates that these events are microbursts.

shock stand off distances, are used to investigate the dependence of the number of microbursts observed above s , as a function of s . This dependence is the microburst complementary cumulative distribution function $\bar{F}(s)$.

The cumulative fraction of microbursts observed above s is the ratio of $N(s)$, the normalized number of microbursts observed above s , to $N(0)$, the total number of microbursts observed

$$\bar{F}(s) = \frac{N(s)}{N(0)} \quad (4.1)$$

where $N(s)$ is defined by

$$N(s) = \sum_{i=s}^{\infty} n_i \left(\frac{S_{max}}{S_i} \right) \quad (4.2)$$

where n_i is the number of microbursts observed by AC6 in i th separation bin. The normalization term S_{max}/S_i is a ratio of the number of 10 Hz samples in

1695 the most sampled separation bin to the number of samples in the ith bin. This
 1696 normalization factor corrects AC6's non-uniform sampling in separation, thus $\bar{F}(s)$
 1697 can be interpreted as the fraction of microbursts observed above s assuming AC6
 1698 sampled evenly in separation. Microburst $\bar{F}(s)$ in LEO is shown by the black curve
 1699 in Fig. 4.3a for $4 < L < 8$ and split into one L-wide bins with the colored curves. The
 1700 separation bin width used in Fig. 4.3 is 5 km. To check for bias in $\bar{F}(s)$ due to the
 1701 choice of separation bins, $\bar{F}(s)$ was resampled using other bin widths and offsets. Bin
 1702 widths as large as 20 – 30 km and bin offsets did not qualitatively effect the curves
 1703 in Fig. 4.3a. The normalization i.e., the number of 10 Hz samples in each separation
 1704 bin, is shown in 4.3c.

1705 The overall trend in Fig. 4.3a shows a sudden cumulative probability drop off,
 1706 followed by a shoulder up to $s \approx 70$ km where $\bar{F}(s)$ drops to nearly zero. A large
 1707 negative gradient of $\bar{F}(s)$ at some separation implies that microbursts must be smaller
 1708 than that separation. To quantify this, Fig. 4.3b shows the microburst probability
 1709 density function (PDF), calculated by differentiating $\bar{F}(s)$. The microburst PDF
 1710 shows a peak at $s < 30$ km as well as a peak between 70 – 80 km separation. These
 1711 PDF peaks are evidence of a sub 30 km microburst population and larger microbursts
 1712 observed up 70–80 km separations. The shaded region around the black curves in Fig.
 1713 4.3a-b shows the standard error due to counting statistics. The uncertainty due to
 1714 false coincidence events i.e. two unrelated microbursts lining up in time by random
 1715 chance was also considered. The microburst duty cycle in a one minute window
 1716 ($\approx 1 L$) around each microburst was calculated. The false coincidence probability is
 1717 the square of the duty cycle and was found to be less than 5% for the majority of
 1718 microbursts. The false coincidence probability for each microburst was then used to
 1719 randomly remove microbursts and $\bar{F}(s)$ was recalculated in 10^4 trials. The spread in
 1720 the $\bar{F}(s)$ trial curves with microbursts randomly removed was much smaller than the

1721 uncertainty due to counting statistics alone.

1722 To compare the microburst size to the size of their hypothesized progenitor
1723 waves, the spacecraft locations during observed microbursts were mapped to the
1724 magnetic equator using the Olson-Pfitzer magnetic field model (Olson and Pfitzer,
1725 1982) which is implemented with a Python wrapper for IRBEM-Lib (Boscher et al.,
1726 2012). As previously stated, a microburst observed in LEO has a size larger than
1727 the spacecraft separation, hence that microburst would also have a size larger than
1728 the spacecraft separation after it was mapped to the magnetic equator. Thus
1729 the procedure to estimate $\bar{F}(s)$ is identical to the LEO size distribution but with
1730 a different normalization. The normalization factors were calculated by mapping
1731 every quality AC6 sample to the magnetic equator and binning them by equatorial
1732 separation into 100 km wide bins. Figure 4.4 shows the equatorial microburst size
1733 distribution in the same format as Fig. 4.3. The equatorial PDF trend is similar to
1734 LEO and most of the microbursts were observed when the AC6 equatorial separation
1735 was less than 200 km.

1736 The results in Figs. 4.3 and 4.4 show the fraction of microbursts observed above a
1737 spacecraft separation and do not fully represent the microbursts size distribution due
1738 to the compounding effects from the range of microburst sizes and random locations
1739 of microbursts with respect to AC6 i.e. even if the microburst size is much larger than
1740 the AC6 separation, some fraction of those microbursts will be only observed by one
1741 AC6 spacecraft. Thus modeling is necessary to capture the compounding influence
1742 of these statistical effects on AC6.

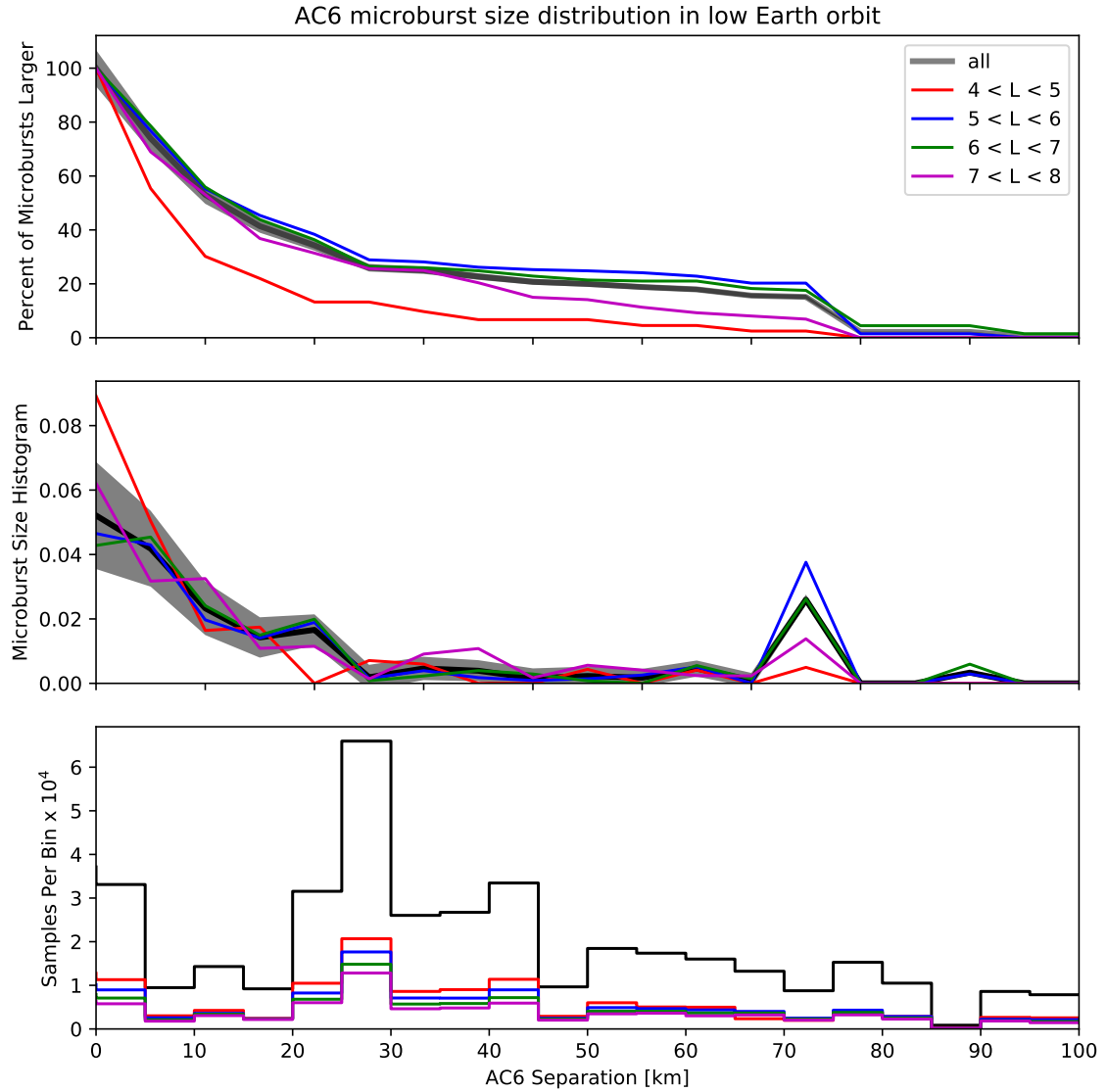


Figure 4.3: Microburst size distribution in low Earth orbit. Panel (a) shows the percent of microbursts observed above that separation after normalizing for the uneven AC6 sampling in separation. Panel (b) shows the microburst probability density (size histogram) as a function of separation. Lastly, panel (c) shows the normalization, i.e. number of simultaneous samples AC6 observed as a function of separation. The colored lines show the distributions binned by L , and the thick black curve for the entire radiation belt ($4 < L < 8$). The gray shading around the black curve shows the uncertainty due to counting statistics.

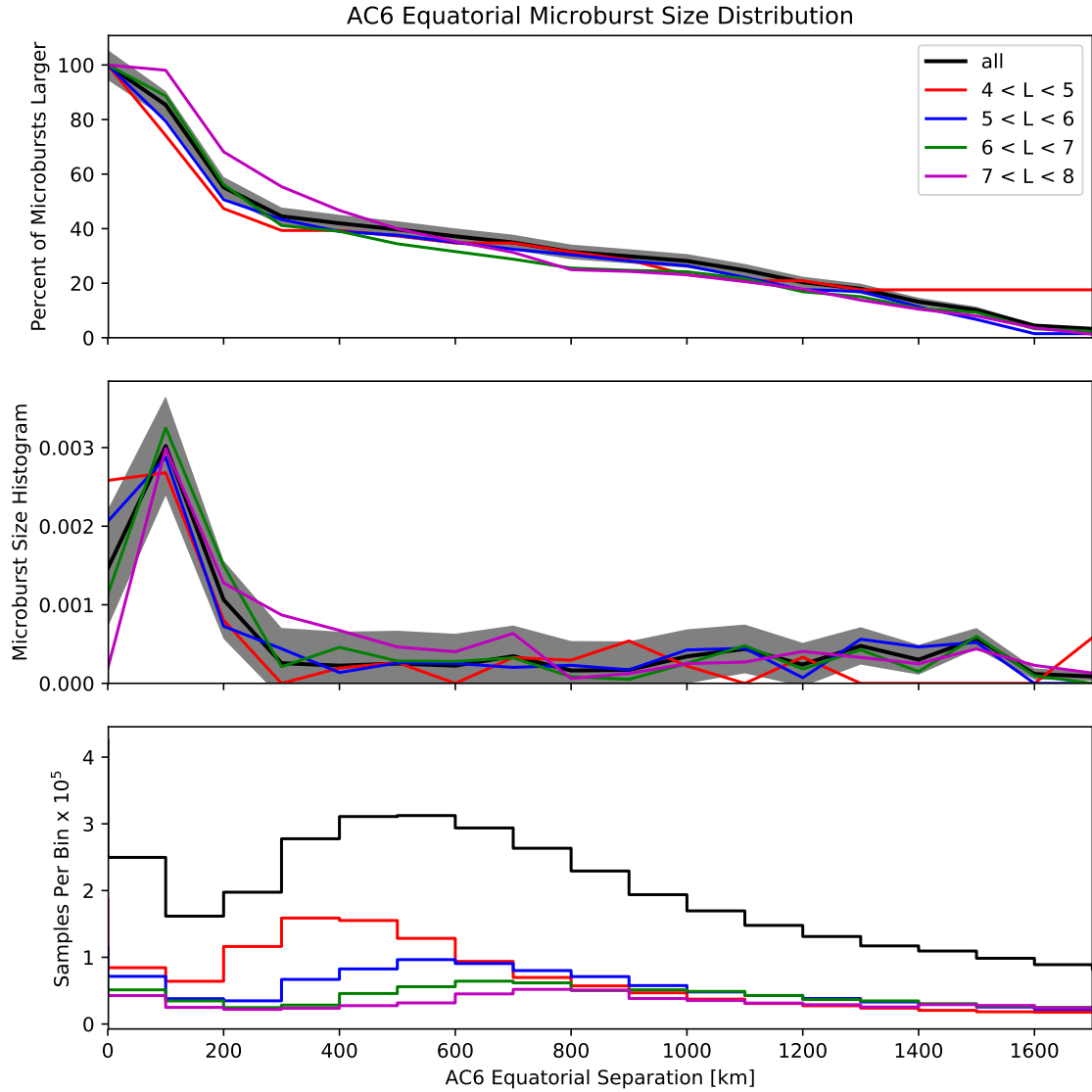


Figure 4.4: Microburst size distribution mapped to the magnetic equator in the same format as Fig. 4.3.

1743

Modeling the Distribution of Microburst Sizes1744 Monte Carlo and Analytic Models to Calculate $\bar{F}(s)$

1745 To account for the effects due to microbursts randomly occurring around
 1746 AC6 with an unknown distribution of microburst sizes, Monte Carlo (MC) and
 1747 analytic models were developed. These models assume a hypothesized distribution
 1748 of microburst sizes expressed with a probability density function $p(d|\theta)$ where θ are
 1749 the dependent variables, and a microburst footprint shape to estimate $\bar{F}(s)$. The
 1750 microburst footprint is assumed to be circular with a diameter d . $p(d|\theta)$ can be
 1751 understood as “the probability of observing a microburst of diameter d , given the
 1752 parameters θ ”. Various microburst size distributions were considered: a one-size and
 1753 two-size microburst populations, and continuous $p(d|\theta)$ such as Maxwell, Weibull,
 1754 and log-normal.

1755 The Monte Carlo model is the most intuitive. It first randomly scatters 10^5
 1756 microburst centers in a 400×400 km grid around AC6. Then each microburst
 1757 center was assigned a diameter, randomly picked from a $p(d|\theta)$ distribution after
 1758 θ parameters were specified. Spacecraft A is placed at the origin, and spacecraft B
 1759 is placed along the positive y-axis at distances from spacecraft A corresponding to
 1760 the AC6 separation bins used in Section 4. Then for each spacecraft B location, the
 1761 number of microbursts that encompass both spacecraft was counted. The modeled
 1762 fraction of microbursts observed above s is then

$$\bar{F}(s) = \frac{\sum_{i>s}^{\infty} n_i}{\sum_{i>0}^{\infty} n_i}. \quad (4.3)$$

1763 where as before the number of microbursts observed by both spacecraft in the i th bin

¹⁷⁶⁴ is n_i .

The analytic model, while identical to the MC model, highlights the geometrical concepts connecting $p(d|\theta)$ and $\bar{F}(s)$ with geometry arguments similar to Trefall et al. (1966). For a microburst with $d = 2r \geq s$, there is an area between AC6 where that microburst will be observed by both spacecraft if the microburst's center lands there. Figure 4.5a-c shows this geometry with the two spacecraft indicated with black dots with varying relations between r and s . All microbursts whose center lies inside the circular area of radius r surrounding either spacecraft will be observed by that spacecraft. If it exists, the intersection of the two circular areas around both spacecraft defines another area, $A(r, s)$ where a microburst will be observed by both spacecraft if the microburst center lands there. This area can be calculated using the circle-circle intersection area equation,

$$A(r, s) = 2r^2 \cos^{-1} \left(\frac{s}{2r} \right) - \frac{s}{2} \sqrt{4r^2 - s^2}. \quad (4.4)$$

¹⁷⁶⁵ Example geometries where $A(r, s) > 0$ are shown in Fig. 4.5b and c. With this
¹⁷⁶⁶ conceptual model and $A(r, s)$, the analytic form of $\bar{F}(s)$ can be found and is derived
¹⁷⁶⁷ in the Supporting Information (SI) Text S1. To demonstrate the effects of random
¹⁷⁶⁸ microburst locations near AC6, examples of the analytic and Monte Carlo $\bar{F}(s)$ curves
¹⁷⁶⁹ are shown in Fig. 4.5d for a one-size, $d = 40$ km microburst population.

¹⁷⁷⁰ Methods for estimating optimal θ parameters

¹⁷⁷¹ At this stage we have all of the ingredients to calculate $\bar{F}(s)$ given a prescribed
¹⁷⁷² $p(d|\theta)$. For each $p(d|\theta)$ tested, the optimal θ parameters are estimated in this study
¹⁷⁷³ using the traditional least squares regression and Bayesian inference. While we
¹⁷⁷⁴ report the θ parameters that minimize least squares, this section focuses on Bayesian
¹⁷⁷⁵ inference because it seamlessly incorporates statistical uncertainty in the data. The

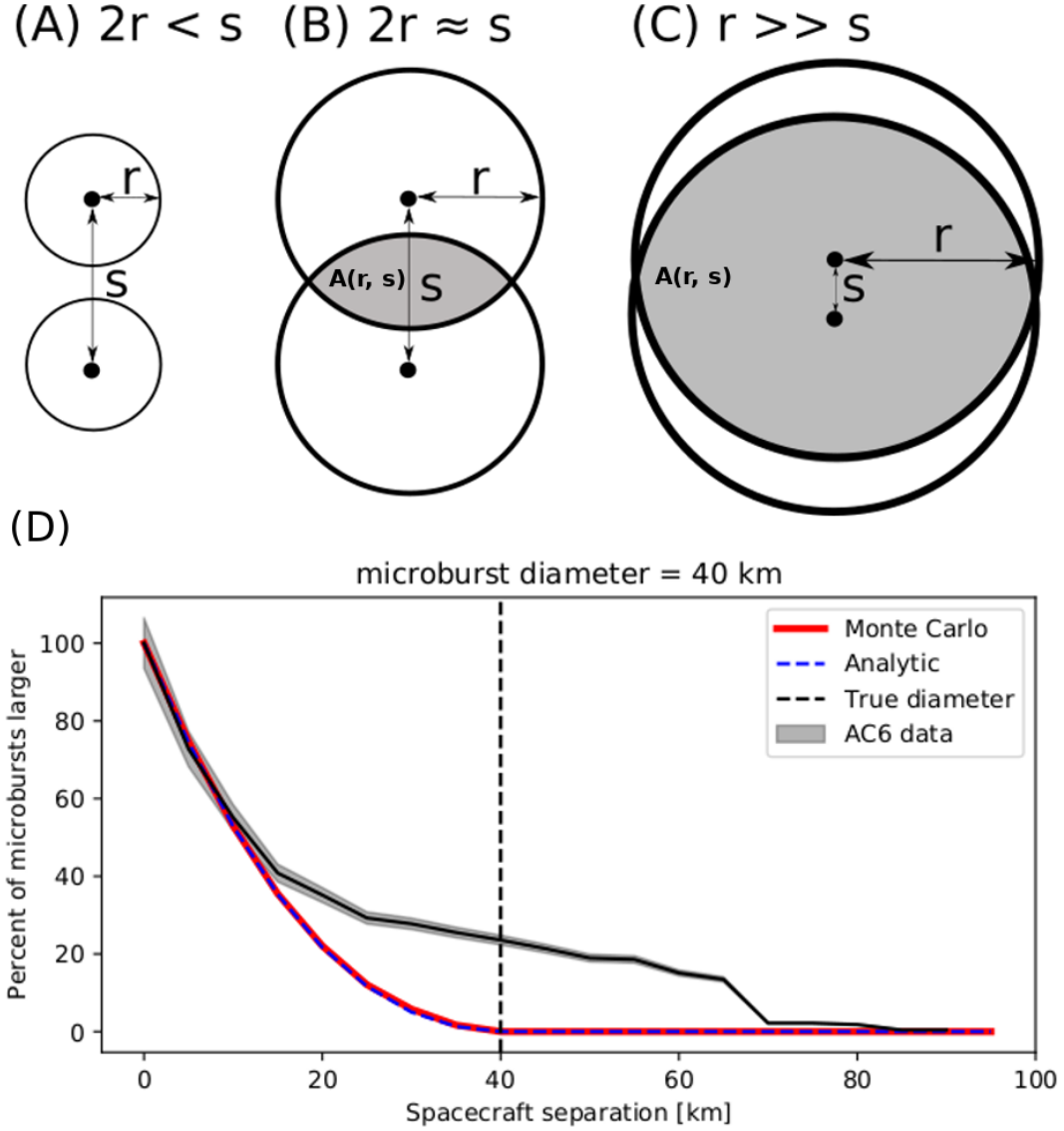


Figure 4.5: Panels A-C show the varying geometries of the analytic model. The two spacecraft are shown as black dots. The enclosing black circle around each spacecraft bounds the area where a microburst will be observed by one or both AC6 units if the microburst's center lies inside the circle. Panel (A) shows the case where microburst diameter is smaller than the AC6 separation and all microbursts will be observed by either unit A or B and never simultaneously. Panel (B) shows the intermediate case where the microburst diameter is comparable to the AC6 separation and some fraction of microbursts will be observed simultaneously. The fraction of the microbursts simultaneously observed is proportional to the circle intersection area $A(r, s)$ and is shown with grey shading. Panel (C) shows the case where the microburst diameter is much larger than the spacecraft separation and nearly all microbursts will be observed by both spacecraft. Lastly panel (D) shows $\bar{F}(s)$ from the AC6 data with a solid black line, and modeled MC and analytic $\bar{F}(s)$ curves for a single-sized microburst distribution with $d = 40$ km.

1776 uncertainty in the data is then propagated to θ which is then no longer an optimal
 1777 value, rather a distribution of values that is consistent with the observations and its
 1778 uncertainty.

1779 Bayesian inference is rooted in Bayes theorem of conditional probability. Given
 1780 the observed $\bar{F}(s)$ as y , and model's dependent variables as θ , Bayes theorem can be
 1781 written as

$$p(\theta|y) = \frac{p(y|\theta)p(\theta)}{p(y)}. \quad (4.5)$$

1782 $p(\theta)$ is the distribution of θ that describe our prior level of knowledge about that
 1783 parameter e.g. from earlier microburst size studies, a microburst size must less than
 1784 500 km in LEO. This is called the prior which is quantified by a PDF such as normal,
 1785 uniform, etc. Next term is the likelihood, $p(y|\theta)$, the conditional probability of
 1786 obtaining y given a particular θ . The likelihood probability is a probabilistic penalty
 1787 function that quantifies the discrepancy between the modeled and observed $\bar{F}(s)$ in
 1788 terms of the standard error. The resulting PDF of θ s consistent with the observations
 1789 is $p(\theta|y)$ known as the posterior distribution. The posterior is an update to our prior
 1790 distributions, modified by the likelihood i.e. the data and its uncertainties. Here, the
 1791 posterior is used to make inferences regarding the range of θ parameters that generate
 1792 a $\bar{F}(s)$ that is consistent with the observations. The last parameter in Bayes theorem
 1793 is $p(y)$. $p(y)$ is the marginal likelihood (evidence) that describes the probability of
 1794 obtaining y after marginalizing over all prior variables. Calculation of $p(y)$ is difficult,
 1795 and often not necessary for model parameter estimation.

1796 With all of the above terminology, the important takeaway is that the posterior
 1797 distribution for each model parameter is interpreted as the range of our model's
 1798 dependent parameters that are consistent with the observations. A 95% credible

1799 interval (CI) for each model parameter is reported here that is interpreted as:
 1800 assuming a hypothesized $p(d|\theta)$, there is a 95% probability that the true θ is inside
 1801 the CI. To sample the posterior distribution, the θ parameter space is explored with
 1802 a Markov Chain Monte Carlo (MCMC) sampler. In a nutshell a Markov Chain is a
 1803 process that samples random variables that depend on only the previous state of those
 1804 random variables. Hence a MCMC sampler is a Monte Carlo sampler that samples
 1805 the θ parameter space by picking random θ values based on the previous state of θ .

1806 The first and one of the most popular MCMC is the Metropolis-Hastings
 1807 sampler (Hastings, 1970; Metropolis et al., 1953). While the Metropolis-Hastings
 1808 sampler is explained in detail in Metropolis et al. (1953) and Hastings (1970) and
 1809 a good introduction given in Sambridge et al. (2006) as well as Sharma (2017), a
 1810 brief overview is warranted. The Metropolis-Hastings sampler samples the posterior
 1811 distribution in N trials. Once an initial set of θ is randomly picked from the prior,
 1812 the i^{th} trial involves the following steps. First calculate the posterior probability for
 1813 θ_i . Then pick a proposal θ_{i+1} to jump to, randomly picked near θ_i in parameter space.
 1814 If the θ_{i+1} posterior probability is higher than θ_i , the MCMC accepts the proposal
 1815 and moves to θ_{i+1} . If the posterior probability of θ_{i+1} is smaller than θ_i , there is a
 1816 random chance that θ_{i+1} will be accepted or rejected (if rejected, $\theta_{i+1} = \theta_i$ and a
 1817 new proposal is generated). This accept/reject criteria allows the sampler to trend
 1818 to more probable θ while also exploring the neighboring regions. After the N trials,
 1819 a histogram is made using the accepted θ s to produce the posterior distribution for
 1820 each model parameter.

1821 Estimating optimal parameters for various microburst size models

The MCMC sampler is first used to test the simplest microburst size model where
 all microbursts are one size and the MCMC will estimate that size. The microburst

size PDF for this model can be expressed as

$$p(d|d_0) = \delta(d - d_0) \quad (4.6)$$

where δ is the Dirac Delta function and d_0 is the diameter of all microbursts according to this model. The range of d that are consistent with the observed $\bar{F}(s)$ is shown in Fig. 4.6. Assuming this model, there is a 95% probability that the microburst diameter is between 38 and 129 km. As a sanity check the optimal size that minimizes least squares is 73 km.

A slight generalization of the one-size model is a two-size microburst population model that assumes the following microburst PDF

$$p(d|d_0, d_1, a) = a\delta(d - d_0) + (1 - a)\delta(d - d_1) \quad (4.7)$$

where the diameters of the two microburst populations are given by d_0 and d_1 and a is the parameter that quantifies the relative fractions of the two populations. The result of this model is shown in Fig. 4.7. The fit is slightly better than the one-size model, although that is to be expected given two more free model parameters. A majority, 98 %, of microbursts, have a diameter between 12 and 47 km with a rare population with a diameter between 76 and 234 km. The set of parameters that minimize least squares is 99.5 % of microbursts are small with a size of 21 km and the remaining 0.5 % of microbursts have a 140 km size.

Other, continuous PDFs were tested including: Maxwellian (Maxwell – Boltzmann), log-normal, and Weibull. The range of model parameters that are consistent with the observed $\bar{F}(s)$ are presented in the SI text S2. These distributions were chosen because they have the following properties that are most realistic: they are continuous, approach 0 in the limit as $r \rightarrow 0$ (lower bound microburst

1840 size is ultimately limited by the electron gyroradius), and can be symmetrical or
 1841 asymmetrical.

1842

Discussion

1843 The LEO microburst $\bar{F}(s)$ estimated in section 4 shows that a majority of
 1844 coincident microbursts were observed by AC6 when they were separated by less than
 1845 a few tens of km. This conclusion is consistent with prior literature and most similar
 1846 to Parks (1967) who reported that many > 15 keV microbursts are less than 40 km
 1847 in diameter while others were on average 80 ± 28 km in diameter. Furthermore, these
 1848 results are similar to the bouncing packet example shown in Blake et al. (1996) with
 1849 a size of “at least a few tens of kilometers”. The relatively small number of large
 1850 > 70 km microbursts observed by AC6 fit in well with the results from Barcus et al.
 1851 (1966) and Brown et al. (1965), although the AC6 separation is mostly latitudinal
 1852 while Barcus et al. (1966) and Brown et al. (1965) used data from pairs of balloons
 1853 separated predominantly in longitude.

1854 Without knowledge of the microburst shape, a direct comparison between the
 1855 AC6 and balloon observations is difficult. Trefall et al. (1966) discussed how a
 1856 hypothetical circular microburst at the scattering location near the magnetic equator
 1857 will be stretched into an ellipse with a semi-major axis in the longitudinal direction.
 1858 This stretching effect should be explored further as it introduces an ambiguity from
 1859 the eccentricity of the ellipse that prevents a direct latitudinal and longitudinal
 1860 comparison.

1861 When comparing our results to more recent studies, the AC6 microburst size
 1862 distribution is much larger than the sizes reported in Dietrich et al. (2010) who
 1863 used very low (VLF) frequency transmission paths and SAMPEX to conclude that
 1864 microbursts must be smaller than 4 km from a small number of microbursts observed

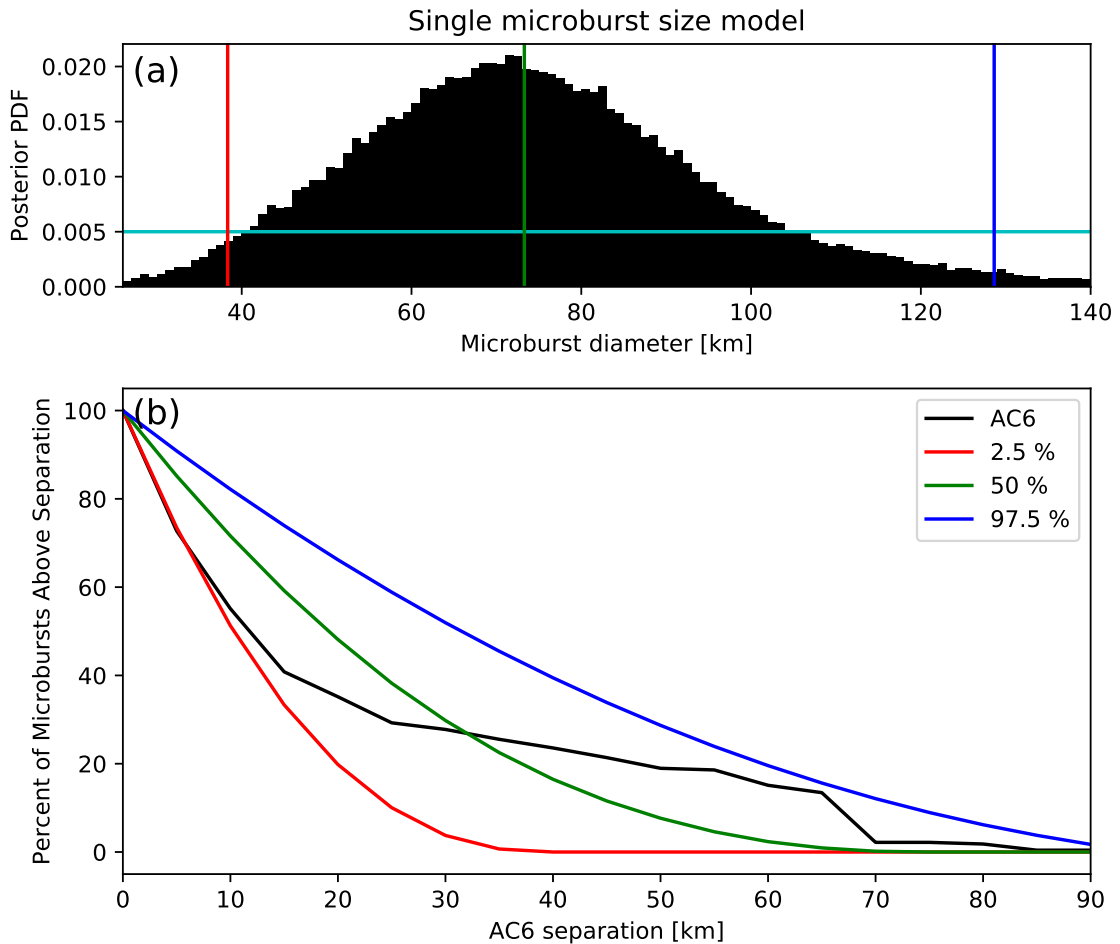


Figure 4.6: Range of plausible microburst sizes assuming all microbursts are one fixed size. Panel (a) shows the posterior probability density function of microburst diameters in black. The red, green, and blue vertical lines at 38, 73, and 129 km represent the 2.5, 50, and 97.5 posterior percentiles, respectively. A uniform prior between 0 and 200 km was assumed for this MCMC run and is shown in cyan. Panel (b) shows the percent of microbursts observed above an AC6 separation for $4 < L < 8$ in black. The 2.5, 50 and 97.5 size percentiles were estimated from the posterior and plotted in red, green, and blue curves, respectively.

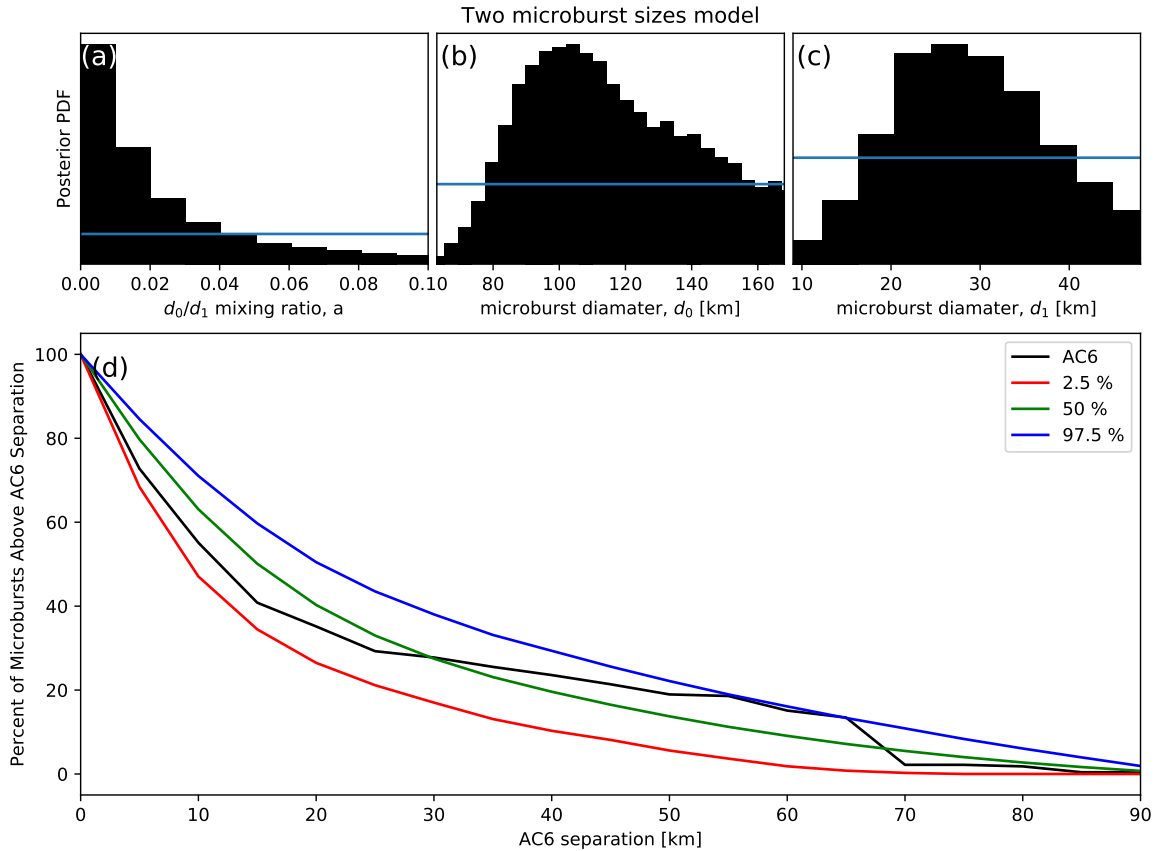


Figure 4.7: Plausible microburst percent curves assuming microburst size distribution is bimodal consisting of two sizes d_0 and d_1 with a mixing term that quantifies the relative occurrence of the d_0 to d_1 microburst populations. Panel (a) shows the posterior distribution for the microburst population mixing term, a with a median value of 0.02. The a prior was uniform between 0 and 0.2. Panel (b) shows the posterior distribution for d_0 , the larger microburst population estimated with a uniform prior between 50 and 200 km and the posterior median diameter of 122 km. Panel (c) shows the posterior distribution for d_1 , the smaller microburst population, estimated using a uniform prior between 0 and 50 km with a median diameter of 28 km. Panel (d) is similar to Fig. 4.6b and shows the AC6 microburst fraction for $4 < L < 8$ in black. A set of 1000 random parameter triples (a , d_0 , and d_1) were drawn from the posterior and used to generate a family of $\bar{F}(s)$ curves. At each s the range of consistent $\bar{F}(s)$ were quantified by the 2.5, 50 and 97.5 percentiles and shown with the red, green, and blue curves, respectively.

1865 during one SAMPEX radiation belt pass. Dietrich et al. (2010) arrived at their
 1866 conclusion by looking for temporal coincidence of microbursts and FAST events,
 1867 subsecond VLF transmission perturbations, but the connection between FAST events
 1868 and microbursts is not well understood. Lastly, our results are consistent with
 1869 FIREBIRD-II observations of a > 11 km microburst reported by Crew et al. (2016),
 1870 and the minority of microbursts observed by AC6 up to $s \approx 70$ km are consistent
 1871 with the > 51 km bouncing packet microburst reported in Shumko et al. (2018).

1872 The microburst PDF shown in Fig. 4.3b suggests that the microburst size
 1873 distribution is bimodal. This has been suggested before by Blake et al. (1996) who
 1874 noted that the > 150 keV and > 1 MeV microbursts are not always well correlated
 1875 e.g. Fig. 10 in Blake et al. (1996). The quality of the AC6 data is insufficient to
 1876 definitively conclude that there are two distinct microburst populations. The different
 1877 microburst population hypothesis can be better tested with an AC6-like mission with
 1878 better energy resolution and homogeneous MLT coverage.

1879 The model results from section 4 emphasize that care must be taken when
 1880 comparing the $\bar{F}(s)$ curves observed by AC6 and the true microburst size distribution
 1881 due to the compounding effect of an unknown microburst size distribution, unknown
 1882 microburst shape, and random microburst locations near AC6. By assuming there is
 1883 only one microburst size, the results in Fig. 4.6 suggest that there is a 95% probability
 1884 that the microburst diameter is somewhere between 38 and 129 km, a relatively wide
 1885 range of values. On the other hand, the two-size model has a smaller variance around
 1886 the AC6 $\bar{F}(s)$, which is expected with the addition of two more free parameters. The
 1887 two size model is interpreted as 98% of microbursts diameters are between 12 and 47
 1888 km and larger microbursts are very uncommon.

1889 A variety of continuous $p(d)$ such as the Maxwellian, Weibull and log-normal
 1890 were also tested. While the continuous microburst PDFs are more realistic, there is

1891 no clear choice of which microburst PDF nature prefers. The one and two-size model
 1892 are simple to interpret, and the two-size model qualitatively fits the observations the
 1893 best out of all $p(d)$ tested. Surely nature does not only have two discrete microburst
 1894 sizes. Rather, the current evidence and reasoning supports a bimodal and continuous
 1895 PDF hypothesis. Due to lack of prior observations and theoretical predictions, it is
 1896 difficult to identify and test a more appropriate $p(d)$ hypothesis at this time.

1897 The equatorial microburst $\bar{F}(s)$ estimated in section 4 and Fig. 4.4b in particular
 1898 shows that the majority of microbursts were observed when the equatorial AC6
 1899 separation was less than 200 km. We will now explore how these results compare
 1900 to prior multi-point measurements of chorus source sizes made near the magnetic
 1901 equator. The International Sun-Earth Explorers (ISEE 1 and 2) were used by Gurnett
 1902 et al. (1979) to make one of the first direct chorus source scale measurements. Gurnett
 1903 et al. (1979) estimated that the wave power correlation scale was on the order of a
 1904 few hundred km across the background magnetic field. Using the Cluster Wide Band
 1905 Data measurements Santolik et al. (2003) found the correlation scale of whistler mode
 1906 chorus waves to be around 100 km near the source region at $L \approx 4$ and midnight
 1907 MLT sector. Furthermore, Turner et al. (2017) used the four satellites comprising the
 1908 Magnetospheric Multiscale Mission and found that rising tone whistler mode chorus
 1909 elements were phase coherent up to 70 km at $L \approx 8$. Lastly, Agapitov et al. (2017,
 1910 2011, 2010, 2018) used multiple sets of spacecraft missions with wave measurements
 1911 near the chorus source region to statistically show that the extent of chorus source
 1912 region can extend from 600 km in the outer radiation belt to greater than 1,000 km
 1913 in the outer magnetosphere.

1914 The equatorial microburst size of less than a few hundred km shows that the
 1915 waves responsible for scattering microburst electrons must have correlated properties
 1916 on those scales. The wave properties necessary for scattering microburst electrons

1917 e.g. coherence, polarization, wave normal angle, etc. can be identified by studying
 1918 the waves properties that are only observed by multiple equatorial spacecraft at
 1919 small separations. These properties can then aid wave-particle scattering model
 1920 development by constraining the wave properties and scattering modes responsible for
 1921 scattering microburst electrons. In turn, future models could then make predictions
 1922 regarding the distribution of microburst sizes in LEO.

1923

Conclusions

1924 In conclusion, the twin AC6 CubeSats enabled the detailed statistical study
 1925 of microburst sizes from a two point measurement platform. Roughly 60% of
 1926 the > 35 keV microbursts were simultaneously observed while AC6 was separated
 1927 by less than 20 km and the rest were observed up to ≈ 70 km separation.
 1928 Modeling the microburst cumulative distribution function is essential to quantify
 1929 the relationship between the number of microbursts observed as a function of
 1930 separation to a hypothesized microburst size distributions. The AC6 microburst
 1931 data, together with modeling, has hinted at the existence of a bimodal microburst
 1932 size PDF with the majority of microbursts with a diameter smaller than 40 km and
 1933 a rare microburst population with a diameter around 100 km. The bimodal size
 1934 hypothesis may be more comprehensively addressed from LEO spacecraft with more
 1935 simultaneous microburst observations, homogeneous MLT coverage, and differential
 1936 energy channels. Moreover, to disentangle the compounding effect that affects two-
 1937 point microburst measurements, a X-ray imager on a high altitude balloon can observe
 1938 the atmospheric microburst footprint and determine the microburst size, shape, and
 1939 any spatial correlations with little ambiguity.

1940 When mapped to the magnetic equator, most microbursts were observed while
 1941 the mapped AC6 separation was less than 200 km. This correlates well with the sizes

1942 of highly correlated chorus waves and it suggests that the wave properties crucial for
1943 scattering microbursts must be correlated over relatively small regions. By studying
1944 the wave properties that are correlated on a few hundred km scales, the dominant
1945 wave scattering modes may be identified.

1946

Acknowledgments

1947 This work was made possible with the help from the many engineers and
1948 scientists at The Aerospace Corporation who designed, built, and operated AC6. M.
1949 Shumko was supported by NASA Headquarters under the NASA Earth and Space
1950 Science Fellowship Program - Grant 80NSSC18K1204. D.L. Turner is thankful for
1951 support from the Van Allen Probes mission and a NASA grant (Prime award number:
1952 80NSSC19K0280). **Other Aerospace and MSU funding sources...** The AC6 data is
1953 available at <http://rbspgway.jhuapl.edu/ac6> and the IRBEM-Lib version used for this
1954 analysis can be downloaded from <https://sourceforge.net/p/irbem/code/616/tree/>.

1955

CONCLUSIONS AND FUTURE WORK

1956 In this dissertation we have explored the microburst scattering mechanism
1957 directly in Chapter 2 and indirectly in Chapters 3 and 4. In Chapter 2 we used
1958 particle and wave instruments on the Van Allen Probes to study microburst signatures
1959 near their scattering region inside the radiation belts. To these observations we
1960 applied the relativistic theory of wave-particle resonant diffusion and found that the
1961 motion of the microburst electrons was not along single-wave characteristic curves in
1962 momentum phase space, given the spacecraft position, orientation and the plasma
1963 environment. This result at first appears to contradict the belief that many members
1964 of the community hold, that microburst precipitation is due to a diffusive process. In
1965 reality both are probably valid on different time scales. Individual microbursts are
1966 probably not scattered diffusively, but the combined contribution of an ensemble of
1967 microbursts will have properties that are well modeled as a diffusion process.

1968 The microburst sizes estimated in prior literature as well as Chapters 3 and
1969 4 show that there is a large variability in microburst sizes although microbursts
1970 are generally small. The study in Ch. 3 gave us a glimpse into the dynamics
1971 of a rarely observed bouncing packet microburst from a dual point measurement
1972 platform. This study has shed light on the lower bound latitudinal and longitudinal
1973 sizes of that microburst, and it was found to be larger than microburst sizes reported
1974 in recent literature, and somewhat smaller than the microburst sizes observed with
1975 high altitude balloons in the mid 1960s. A comparison between satellites separated
1976 in latitude and balloons separated in longitude is somewhat an apples to oranges
1977 comparison because the microburst shape is still unknown.

1978 The AC6 microburst study in Ch. 4 showed that in LEO, 60% of the 662
1979 microbursts were observed while the AC6 separation was less than a few tens of km

1980 while a minority of microbursts were observed up to ≈ 100 km separation. These con-
 1981 clusions agree with prior literature from high altitude balloons and LEO spacecraft,
 1982 although as mentioned before the microburst shape makes comparisons somewhat
 1983 ambiguous. The equatorial microburst size distribution is heavily dominated by
 1984 microbursts smaller than 200 km. This is a very small size, highlighting that the
 1985 waves that scatter microburst electrons must have correlated properties on those
 1986 scales. A preliminary comparison between the equatorial distributions of microbursts
 1987 and lower band whistler mode chorus waves shows a better agreement between high
 1988 amplitude chorus waves and microbursts, although a more thorough study is necessary
 1989 to address the various systematic biases.

1990

Future work

1991 An extension of the case study in Chapter 2 is a statistical study using the
 1992 Van Allen Probes. Other microburst-like events have already been identified by eye.
 1993 These other events were also simultaneously observed with enhanced wave activity,
 1994 hence they may be related and a further investigation is warranted. A microburst
 1995 detection scheme similar to the one used in Chapter 4 can be easily implemented to
 1996 automatically identify other microbursts for further study. A few compelling questions
 1997 that can be addressed with this study are: what is the typical pitch angle extent of
 1998 microbursts? Do these microbursts have a similar MLT distribution to microbursts
 1999 observed in LEO? What fraction of microbursts were observed during enhanced wave
 2000 activity? What wave modes and properties are observed during these events? And
 2001 lastly, what fraction of microbursts can be modeled with a diffusive process?

2002 Another study related to the electron bounce period analysis done in Ch. 3 can
 2003 be used to verify magnetic field models and in particular the length of magnetic field
 2004 lines. Current magnetospheric magnetic field models assume that Earth's internal

2005 magnetic field is relatively static e.g. the International Geomagnetic Reference Field,
2006 and superpose that field with a highly dynamic field model who's dynamics are driven
2007 by the plasma environment in the magnetosphere and the solar wind. The difficulty
2008 lies in accurately modeling this dynamic field, and verifying these models is somewhat
2009 difficult. One verification technique involves identifying bouncing packet microbursts
2010 observed by SAMPEX and FIREBIRD, and then estimate the electron bounce period
2011 in a similar fashion to the analysis in Ch. 3. The empirical bounce period can then
2012 be compared to modeled bounce periods from a variety of magnetic field models, and
2013 then model accuracy estimated. Identifying the bouncing packet microbursts is not
2014 easy, but may be possible with an auto-correlation or machine learning approaches
2015 e.g. a neural network.

2016 The last project described here that can be done with existing data is to test
2017 the hypothesis that curtains, which were briefly described in Ch. 4, are remnants
2018 of microbursts in the drift loss cone. One way to test this hypothesis is to look for
2019 the occurrence rates of curtains eastward and westward of the SAA. If curtains are
2020 electrons in the drift loss cone then the SAA will remove curtains as they drift to the
2021 east. Thus under the proposed hypothesis the number of curtains should be greater
2022 just to the west of the SAA than to the east. An alternative approach to test this
2023 hypothesis is to estimate how each curtain's flux changes between the two AC6 units.
2024 If curtains are drifting and have a falling energy spectra, then the larger number of
2025 slower-drifting, low energy, electrons will appear as an enhancement in the flux for
2026 the trailing spacecraft. If such a trend is apparent then curtains must be drifting,
2027 otherwise they may be actively scattered in the same location.

2028

Future missions

2029 A few upcoming missions are dedicated to study microbursts and would be able
2030 to address some of the unknown questions raised in this dissertation and discussed
2031 below.

2032 One approach to determine if microburst scattering is a diffusive or a non-linear
2033 process can be done in LEO where the transport of microburst electrons inside the
2034 loss cone can be more easily observed. In contrast to particle measurements made
2035 near the magnetic equator where the local loss cone is only a few degrees, the loss cone
2036 in LEO is $\approx 60^\circ$ which is much easier to resolve with an instrument with multiple look
2037 directions. With this measurement, different scattering mechanisms can be studied.
2038 If the scattering process is diffusive, then the microburst flux will be monotonically
2039 decreasing (or flat) deeper into the loss cone. A non-linear scattering process, on
2040 the other hand, will have a more complex pitch angle vs flux profile e.g. a relative
2041 maximum at 0° , followed by decreasing flux towards the loss cone boundary. One
2042 mission that plans to make this measurement is The Relativistic Electron Atmospheric
2043 Loss (REAL) CubeSat. This CubeSat, planned to launch in 2021, will sample the
2044 inside and outside of the loss cone with a solid state detector with a five look directions.

2045 As previously mentioned, the unknown microburst shape makes microburst size
2046 comparisons between balloons and satellites ambiguous. One of the most feasible
2047 ways to resolve this ambiguity is to image microburst precipitation in the upper
2048 atmosphere using a balloon. This imaging is possible because when microburst
2049 electrons impact the atmosphere, they scatter with Earth's atmosphere and generate
2050 bremsstrahlung X-rays. These X-rays have a relatively long mean free path at ≈ 35
2051 km balloon altitudes so a balloon-borne imager will predominately observe primary
2052 X-rays emitted directly from the microburst electrons. This idea is the basis for the

2053 upcoming Balloon Observations Of Microburst Scales (BOOMS) mission. BOOMS
2054 will fly a set of X-ray pinhole imagers containing a scintillator crystal (to convert
2055 from X-rays to visible light) and a grid of photomultiplier tubes (PMT) underneath
2056 to record the distribution of light. The distribution of light across the grid of
2057 PMTs, together with instrument modeling, can be used to convert between the PMT
2058 signal and the angular position for each observed X-ray. Over a longer exposure, a
2059 probabilistic image can then be constructed of the microburst X-ray source. Then
2060 the microburst shape, and any spatial correlations of trains of microbursts can be
2061 observed.

- 2063 Abel, B. and Thorne, R. M. (1998). Electron scattering loss in earth's inner
2064 magnetosphere: 1. dominant physical processes. *Journal of Geophysical Research: Space Physics*, 103(A2):2385–2396.
- 2066 Agapitov, O., Blum, L. W., Mozer, F. S., Bonnell, J. W., and Wygant, J. (2017).
2067 Chorus whistler wave source scales as determined from multipoint van allen probe
2068 measurements. *Geophysical Research Letters*, pages n/a–n/a. 2017GL072701.
- 2069 Agapitov, O., Krasnoselskikh, V., Dudok de Wit, T., Khotyaintsev, Y., Pickett,
2070 J. S., Santolik, O., and Rolland, G. (2011). Multispacecraft observations of chorus
2071 emissions as a tool for the plasma density fluctuations' remote sensing. *Journal of Geophysical Research: Space Physics*, 116(A9):n/a–n/a. A09222.
- 2073 Agapitov, O., Krasnoselskikh, V., Zaliznyak, Y., Angelopoulos, V., Le Contel, O.,
2074 and Rolland, G. (2010). Chorus source region localization in the earth's outer
2075 magnetosphere using themis measurements. *Annales Geophysicae*, 28(6):1377–
2076 1386.
- 2077 Agapitov, O., Mourenas, D., Artemyev, A., Mozer, F., Bonnell, J., Angelopoulos, V.,
2078 Shastun, V., and Krasnoselskikh, V. (2018). Spatial extent and temporal correlation
2079 of chorus and hiss: Statistical results from multipoint themis observations. *Journal of Geophysical Research: Space Physics*, 123(10):8317–8330.
- 2081 Anderson, B., Shekhar, S., Millan, R., Crew, A., Spence, H., Klumpar, D., Blake, J.,
2082 O'Brien, T., and Turner, D. (2017). Spatial scale and duration of one microburst
2083 region on 13 August 2015. *Journal of Geophysical Research: Space Physics*.
- 2084 Anderson, K. A. and Milton, D. W. (1964). Balloon observations of X rays in the
2085 auroral zone: 3. High time resolution studies. *Journal of Geophysical Research*,
2086 69(21):4457–4479.
- 2087 Barcus, J., Brown, R., and Rosenberg, T. (1966). Spatial and temporal character of
2088 fast variations in auroral-zone x rays. *Journal of Geophysical Research*, 71(1):125–
2089 141.
- 2090 Baumjohann, W. and Treumann, R. A. (1997). *Basic space plasma physics*. World
2091 Scientific.
- 2092 Blake, J., Carranza, P., Claudepierre, S., Clemons, J., Crain, W., Dotan, Y.,
2093 Fennell, J., Fuentes, F., Galvan, R., George, J., et al. (2013). The magnetic electron
2094 ion spectrometer (MagEIS) instruments aboard the radiation belt storm probes
2095 (RBSP) spacecraft. *Space Science Reviews*, 179(1-4):383–421.

- 2096 Blake, J., Looper, M., Baker, D., Nakamura, R., Klecker, B., and Hovestadt, D.
 2097 (1996). New high temporal and spatial resolution measurements by sampex of the
 2098 precipitation of relativistic electrons. *Advances in Space Research*, 18(8):171 – 186.
- 2099 Blake, J. B. and O'Brien, T. P. (2016). Observations of small-scale latitudinal
 2100 structure in energetic electron precipitation. *Journal of Geophysical Research: Space Physics*, 121(4):3031–3035. 2015JA021815.
- 2102 Blum, L., Li, X., and Denton, M. (2015). Rapid MeV electron precipitation as
 2103 observed by SAMPEX/HILT during high-speed stream-driven storms. *Journal of Geophysical Research: Space Physics*, 120(5):3783–3794. 2014JA020633.
- 2105 Bortnik, J., Thorne, R., and Inan, U. S. (2008). Nonlinear interaction of energetic
 2106 electrons with large amplitude chorus. *Geophysical Research Letters*, 35(21).
- 2107 Boscher, D., Bourdarie, S., O'Brien, P., Guild, T., and Shumko, M. (2012). Irbem-lib
 2108 library.
- 2109 Breneman, A., Crew, A., Sample, J., Klumpar, D., Johnson, A., Agapitov, O.,
 2110 Shumko, M., Turner, D., Santolik, O., Wygant, J., et al. (2017). Observations
 2111 directly linking relativistic electron microbursts to whistler mode chorus: Van allen
 2112 probes and FIREBIRD II. *Geophysical Research Letters*.
- 2113 Breneman, A. W., Halford, A., Millan, R., McCarthy, M., Fennell, J., Sample, J.,
 2114 Woodger, L., Hospodarsky, G., Wygant, J. R., Cattell, C. A., et al. (2015). Global-
 2115 scale coherence modulation of radiation-belt electron loss from plasmaspheric hiss.
 2116 *Nature*, 523(7559):193.
- 2117 Brown, R., Barcus, J., and Parsons, N. (1965). Balloon observations of auroral zone
 2118 x rays in conjugate regions. 2. microbursts and pulsations. *Journal of Geophysical
 2119 Research (U.S.)*.
- 2120 Capannolo, L., Li, W., Ma, Q., Shen, X.-C., Zhang, X.-J., Redmon, R., Rodriguez,
 2121 J., Engebretson, M., Kletzing, C., Kurth, W., et al. (2019). Energetic electron
 2122 precipitation: multi-event analysis of its spatial extent during emic wave activity.
 2123 *Journal of Geophysical Research: Space Physics*.
- 2124 Claudepierre, S., O'Brien, T., Looper, M., Blake, J., Fennell, J., Roeder, J.,
 2125 Clemons, J., Mazur, J., Turner, D., Reeves, G., et al. (2019). A revised look
 2126 at relativistic electrons in the earth's inner radiation zone and slot region. *Journal
 2127 of Geophysical Research: Space Physics*, 124(2):934–951.
- 2128 Comess, M., Smith, D., Selesnick, R., Millan, R., and Sample, J. (2013). Duskside
 2129 relativistic electron precipitation as measured by sampex: A statistical survey.
 2130 *Journal of Geophysical Research: Space Physics*, 118(8):5050–5058.

- 2131 Crew, A. B., Spence, H. E., Blake, J. B., Klumpar, D. M., Larsen, B. A., O'Brien,
 2132 T. P., Driscoll, S., Handley, M., Legere, J., Longworth, S., Mashburn, K.,
 2133 Mosleh, E., Ryhajlo, N., Smith, S., Springer, L., and Widholm, M. (2016). First
 2134 multipoint in situ observations of electron microbursts: Initial results from the
 2135 NSF FIREBIRD II mission. *Journal of Geophysical Research: Space Physics*,
 2136 121(6):5272–5283. 2016JA022485.
- 2137 Datta, S., Skoug, R., McCarthy, M., and Parks, G. (1997). Modeling of microburst
 2138 electron precipitation using pitch angle diffusion theory. *Journal of Geophysical
 2139 Research: Space Physics*, 102(A8):17325–17333.
- 2140 Dietrich, S., Rodger, C. J., Clilverd, M. A., Bortnik, J., and Raita, T. (2010).
 2141 Relativistic microburst storm characteristics: Combined satellite and ground-based
 2142 observations. *Journal of Geophysical Research: Space Physics*, 115(A12).
- 2143 Douma, E., Rodger, C., Blum, L., O'Brien, T., Clilverd, M., and Blake, J. (2019).
 2144 Characteristics of relativistic microburst intensity from sampex observations.
 2145 *Journal of Geophysical Research: Space Physics*.
- 2146 Douma, E., Rodger, C. J., Blum, L. W., and Clilverd, M. A. (2017). Occurrence
 2147 characteristics of relativistic electron microbursts from SAMPEX observations.
 2148 *Journal of Geophysical Research: Space Physics*, 122(8):8096–8107. 2017JA024067.
- 2149 Eastwood, J., Hietala, H., Toth, G., Phan, T., and Fujimoto, M. (2015). What
 2150 controls the structure and dynamics of earths magnetosphere? *Space Science
 2151 Reviews*, 188(1-4):251–286.
- 2152 Fang, X., Randall, C. E., Lummerzheim, D., Wang, W., Lu, G., Solomon, S. C., and
 2153 Frahm, R. A. (2010). Parameterization of monoenergetic electron impact ionization.
 2154 *Geophysical Research Letters*, 37(22).
- 2155 Funsten, H., Skoug, R., Guthrie, A., MacDonald, E., Baldonado, J., Harper, R.,
 2156 Henderson, K., Kihara, K., Lake, J., Larsen, B., et al. (2013). Helium, Oxygen,
 2157 Proton, and Electron (HOPE) mass spectrometer for the radiation belt storm
 2158 probes mission. *Space Science Reviews*, 179(1-4):423–484.
- 2159 Greeley, A., Kanekal, S., Baker, D., Klecker, B., and Schiller, Q. (2019). Quantifying
 2160 the contribution of microbursts to global electron loss in the radiation belts. *Journal
 2161 of Geophysical Research: Space Physics*.
- 2162 Gurnett, D., Anderson, R., Scarf, F., Fredricks, R., and Smith, E. (1979). Initial
 2163 results from the iese-1 and-2 plasma wave investigation. *Space Science Reviews*,
 2164 23(1):103–122.
- 2165 Hastings, W. K. (1970). Monte carlo sampling methods using markov chains and
 2166 their applications.

- 2167 Hendry, A. T., Rodger, C. J., and Clilverd, M. A. (2017). Evidence of sub-mev
 2168 emic-driven electron precipitation. *Geophysical Research Letters*, 44(3):1210–1218.
- 2169 Hoots, F. R. and Roehrich, R. L. (1980). Models for propagation of norad element
 2170 sets. Technical Report 3, Spacetrack.
- 2171 Horne, R., Glauert, S., Meredith, N., Boscher, D., Maget, V., Heynderickx, D., and
 2172 Pitchford, D. (2013). Space weather impacts on satellites and forecasting the earth's
 2173 electron radiation belts with spacecast. *Space Weather*, 11(4):169–186.
- 2174 Horne, R., Thorne, R., Meredith, N., and Anderson, R. (2003). Diffuse auroral
 2175 electron scattering by electron cyclotron harmonic and whistler mode waves during
 2176 an isolated substorm. *Journal of Geophysical Research: Space Physics*, 108(A7).
- 2177 Horne, R. B. and Thorne, R. M. (2003). Relativistic electron acceleration and
 2178 precipitation during resonant interactions with whistler-mode chorus. *Geophysical
 2179 Research Letters*, 30(10). 1527.
- 2180 Horne, R. B., Thorne, R. M., Shprits, Y. Y., Meredith, N. P., Glauert, S. A., Smith,
 2181 A. J., Kanekal, S. G., Baker, D. N., Engebretson, M. J., Posch, J. L., et al.
 2182 (2005). Wave acceleration of electrons in the van allen radiation belts. *Nature*,
 2183 437(7056):227.
- 2184 Joy, S., Kivelson, M., Walker, R., Khurana, K., Russell, C., and Ogino, T. (2002).
 2185 Probabilistic models of the jovian magnetopause and bow shock locations. *Journal
 2186 of Geophysical Research: Space Physics*, 107(A10):SMP–17.
- 2187 Kasahara, S., Miyoshi, Y., Yokota, S., Mitani, T., Kasahara, Y., Matsuda, S.,
 2188 Kumamoto, A., Matsuoka, A., Kazama, Y., Frey, H., et al. (2018). Pulsating
 2189 aurora from electron scattering by chorus waves. *Nature*, 554(7692):337.
- 2190 Kletzing, C., Kurth, W., Acuna, M., MacDowall, R., Torbert, R., Averkamp, T.,
 2191 Bodet, D., Bounds, S., Chutter, M., Connerney, J., et al. (2013). The electric and
 2192 magnetic field instrument suite and integrated science (EMFISIS) on RBSP. *Space
 2193 Science Reviews*, 179(1-4):127–181.
- 2194 Klumpar, D., Springer, L., Mosleh, E., Mashburn, K., Berardinelli, S., Gunderson,
 2195 A., Handly, M., Ryhajlo, N., Spence, H., Smith, S., Legere, J., Widholm, M.,
 2196 Longworth, S., Crew, A., Larsen, B., Blake, J., and Walmsley, N. (2015). Flight
 2197 system technologies enabling the twin-cubesat firebird-ii scientific mission.
- 2198 Lee, J. J., Parks, G. K., Lee, E., Tsurutani, B. T., Hwang, J., Cho, K. S., Kim, K.-H.,
 2199 Park, Y. D., Min, K. W., and McCarthy, M. P. (2012). Anisotropic pitch angle
 2200 distribution of 100 keV microburst electrons in the loss cone: measurements from
 2201 STSAT-1. *Annales Geophysicae*, 30(11):1567–1573.

- 2202 Lee, J.-J., Parks, G. K., Min, K. W., Kim, H. J., Park, J., Hwang, J., McCarthy,
 2203 M. P., Lee, E., Ryu, K. S., Lim, J. T., Sim, E. S., Lee, H. W., Kang, K. I., and
 2204 Park, H. Y. (2005). Energy spectra of 170–360 keV electron microbursts measured
 2205 by the korean STSAT-1. *Geophysical Research Letters*, 32(13). L13106.
- 2206 Li, W., Thorne, R., Angelopoulos, V., Bonnell, J., McFadden, J., Carlson, C.,
 2207 LeContel, O., Roux, A., Glassmeier, K., and Auster, H. (2009a). Evaluation of
 2208 whistler-mode chorus intensification on the nightside during an injection event
 2209 observed on the THEMIS spacecraft. *Journal of Geophysical Research: Space
 2210 Physics*, 114(A1).
- 2211 Li, W., Thorne, R., Bortnik, J., Tao, X., and Angelopoulos, V. (2012). Characteristics
 2212 of hiss-like and discrete whistler-mode emissions. *Geophysical Research Letters*,
 2213 39(18).
- 2214 Li, W., Thorne, R. M., Angelopoulos, V., Bortnik, J., Cully, C. M., Ni, B., LeContel,
 2215 O., Roux, A., Auster, U., and Magnes, W. (2009b). Global distribution of whistler-
 2216 mode chorus waves observed on the THEMIS spacecraft. *Geophysical Research
 2217 Letters*, 36(9). L09104.
- 2218 Li, X., Selesnick, R., Schiller, Q., Zhang, K., Zhao, H., Baker, D. N., and Temerin,
 2219 M. A. (2017). Measurement of electrons from albedo neutron decay and neutron
 2220 density in near-earth space. *Nature*, 552(7685):382.
- 2221 Lorentzen, K. R., Blake, J. B., Inan, U. S., and Bortnik, J. (2001a). Observations
 2222 of relativistic electron microbursts in association with VLF chorus. *Journal of
 2223 Geophysical Research: Space Physics*, 106(A4):6017–6027.
- 2224 Lorentzen, K. R.,Looper, M. D., and Blake, J. B. (2001b). Relativistic electron
 2225 microbursts during the GEM storms. *Geophysical Research Letters*, 28(13):2573–
 2226 2576.
- 2227 Lyons, L. R. and Thorne, R. M. (1973). Equilibrium structure of radiation belt
 2228 electrons. *Journal of Geophysical Research*, 78(13):2142–2149.
- 2229 Manweiler, J. W. and Zwiener, H. M. (2018). Science Operations Center (SOC)
 2230 RBSPICE Science Data Handbook Revision: e. Technical report, Fundamental
 2231 Technologies, LLC.
- 2232 Mauk, B., Fox, N. J., Kanekal, S., Kessel, R., Sibeck, D., and Ukhorskiy, A. (2013).
 2233 Science objectives and rationale for the radiation belt storm probes mission. *Space
 2234 Science Reviews*, 179(1-4):3–27.
- 2235 Meredith, N., Horne, R., Summers, D., Thorne, R., Iles, R., Heynderickx, D., and
 2236 Anderson, R. (2002). Evidence for acceleration of outer zone electrons to relativistic
 2237 energies by whistler mode chorus. In *Annales Geophysicae*, volume 20, pages 967–
 2238 979.

- 2239 Metropolis, N., Rosenbluth, A. W., Rosenbluth, M. N., Teller, A. H., and Teller, E.
 2240 (1953). Equation of state calculations by fast computing machines. *The journal of
 2241 chemical physics*, 21(6):1087–1092.
- 2242 Millan, R. and Thorne, R. (2007). Review of radiation belt relativistic electron losses.
 2243 *Journal of Atmospheric and Solar-Terrestrial Physics*, 69(3):362 – 377.
- 2244 Millan, R. M., Lin, R., Smith, D., Lorentzen, K., and McCarthy, M. (2002). X-
 2245 ray observations of mev electron precipitation with a balloon-borne germanium
 2246 spectrometer. *Geophysical research letters*, 29(24).
- 2247 Mitchell, D., Lanzerotti, L., Kim, C., Stokes, M., Ho, G., Cooper, S., Ukhorskiy, A.,
 2248 Manweiler, J., Jaskulek, S., Haggerty, D., et al. (2013). Radiation belt storm probes
 2249 ion composition experiment (RBSPICE). *Space Science Reviews*, 179(1-4):263–308.
- 2250 Mozer, F. S., Agapitov, O. V., Blake, J. B., and Vasko, I. Y. (2018). Simultaneous
 2251 observations of lower band chorus emissions at the equator and microburst
 2252 precipitating electrons in the ionosphere. *Geophysical Research Letters*.
- 2253 Nakamura, R., Baker, D. N., Blake, J. B., Kanekal, S., Klecker, B., and Hovestadt,
 2254 D. (1995). Relativistic electron precipitation enhancements near the outer edge of
 2255 the radiation belt. *Geophysical Research Letters*, 22(9):1129–1132.
- 2256 Nakamura, R., Isowa, M., Kamide, Y., Baker, D., Blake, J., and Looper, M. (2000).
 2257 Observations of relativistic electron microbursts in association with VLF chorus.
 2258 *J. Geophys. Res*, 105:15875–15885.
- 2259 Nishimura, Y., Bortnik, J., Li, W., Thorne, R., Chen, L., Lyons, L., Angelopoulos,
 2260 V., Mende, S., Bonnell, J., Le Contel, O., et al. (2011). Multievent study of the
 2261 correlation between pulsating aurora and whistler mode chorus emissions. *Journal
 2262 of Geophysical Research: Space Physics*, 116(A11).
- 2263 O'Brien, T., Claudepierre, S., Blake, J., Fennell, J. F., Clemons, J., Roeder, J.,
 2264 Spence, H. E., Reeves, G., and Baker, D. (2014). An empirically observed pitch-
 2265 angle diffusion eigenmode in the earth's electron belt near $\lambda^* = 5.0$. *Geophysical
 2266 Research Letters*, 41(2):251–258.
- 2267 O'Brien, T., Claudepierre, S., Guild, T., Fennell, J., Turner, D., Blake, J., Clemons,
 2268 J., and Roeder, J. (2016a). Inner zone and slot electron radial diffusion revisited.
 2269 *Geophysical Research Letters*, 43(14):7301–7310.
- 2270 O'Brien, T. and Moldwin, M. (2003). Empirical plasmapause models from magnetic
 2271 indices. *Geophysical Research Letters*, 30(4).
- 2272 O'Brien, T. P., Blake, J. B., and W., G. J. (2016b). Aerocube-6 dosimeter data
 2273 readme. Technical Report TOR-2016-01155, The Aerospace Corporation.

- 2274 O'Brien, T. P., Looper, M. D., and Blake, J. B. (2004). Quantification of relativistic
 2275 electron microburst losses during the GEM storms. *Geophysical Research Letters*,
 2276 31(4). L04802.
- 2277 O'Brien, T. P., Lorentzen, K. R., Mann, I. R., Meredith, N. P., Blake, J. B., Fennell,
 2278 J. F., Looper, M. D., Milling, D. K., and Anderson, R. R. (2003). Energization of
 2279 relativistic electrons in the presence of ULF power and MeV microbursts: Evidence
 2280 for dual ULF and VLF acceleration. *Journal of Geophysical Research: Space*
 2281 *Physics*, 108(A8).
- 2282 Olson, W. P. and Pfitzer, K. A. (1982). A dynamic model of the magnetospheric
 2283 magnetic and electric fields for july 29, 1977. *Journal of Geophysical Research: Space*
 2284 *Physics*, 87(A8):5943–5948.
- 2285 Ozaki, M., Miyoshi, Y., Shiokawa, K., Hosokawa, K., Oyama, S.-i., Kataoka, R.,
 2286 Ebihara, Y., Ogawa, Y., Kasahara, Y., Yagitani, S., et al. (2019). Visualization of
 2287 rapid electron precipitation via chorus element wave–particle interactions. *Nature*
 2288 *communications*, 10(1):257.
- 2289 Ozaki, M., Yagitani, S., Ishizaka, K., Shiokawa, K., Miyoshi, Y., Kadokura, A.,
 2290 Yamagishi, H., Kataoka, R., Ieda, A., Ebihara, Y., Sato, N., and Nagano, I. (2012).
 2291 Observed correlation between pulsating aurora and chorus waves at Syowa Station
 2292 in Antarctica: A case study. *Journal of Geophysical Research: Space Physics*,
 2293 117(A8).
- 2294 Parks, G. (2003). *Physics Of Space Plasmas: An Introduction, Second Edition*.
 2295 Westview Press.
- 2296 Parks, G. K. (1967). Spatial characteristics of auroral-zone X-ray microbursts. *Journal*
 2297 *of Geophysical Research*, 72(1):215–226.
- 2298 Reeves, G., Spence, H. E., Henderson, M., Morley, S., Friedel, R., Funsten, H., Baker,
 2299 D., Kanekal, S., Blake, J., Fennell, J., et al. (2013). Electron acceleration in the
 2300 heart of the van allen radiation belts. *Science*, 341(6149):991–994.
- 2301 Reeves, G. D., McAdams, K. L., Friedel, R. H. W., and O'Brien, T. P. (2003). Ac-
 2302 celeration and loss of relativistic electrons during geomagnetic storms. *Geophysical*
 2303 *Research Letters*, 30(10):n/a–n/a. 1529.
- 2304 Sambridge, M., Gallagher, K., Jackson, A., and Rickwood, P. (2006). Trans-
 2305 dimensional inverse problems, model comparison and the evidence. *Geophysical*
 2306 *Journal International*, 167(2):528–542.
- 2307 Santolik, O., Gurnett, D., Pickett, J., Parrot, M., and Cornilleau-Wehrlin, N. (2003).
 2308 Spatio-temporal structure of storm-time chorus. *Journal of Geophysical Research:*
 2309 *Space Physics*, 108(A7).

- 2310 Santolk, O., Parrot, M., and Lefevre, F. (2003). Singular value decomposition
 2311 methods for wave propagation analysis. *Radio Science*, 38(1):n/a–n/a. 1010.
- 2312 Schulz, M. and Lanzerotti, L. J. (1974). *Particle Diffusion in the Radiation Belts*.
 2313 Springer.
- 2314 Selesnick, R. S., Blake, J. B., and Mewaldt, R. A. (2003). Atmospheric losses of
 2315 radiation belt electrons. *Journal of Geophysical Research: Space Physics*, 108(A12).
 2316 1468.
- 2317 Seppälä, A., Douma, E., Rodger, C., Verronen, P., Clilverd, M. A., and Bortnik, J.
 2318 (2018). Relativistic electron microburst events: Modeling the atmospheric impact.
 2319 *Geophysical Research Letters*, 45(2):1141–1147.
- 2320 Sharma, S. (2017). Markov chain monte carlo methods for bayesian data analysis in
 2321 astronomy. *Annual Review of Astronomy and Astrophysics*, 55:213–259.
- 2322 Shprits, Y. Y., Meredith, N. P., and Thorne, R. M. (2007). Parameterization
 2323 of radiation belt electron loss timescales due to interactions with chorus waves.
 2324 *Geophysical Research Letters*, 34(11):n/a–n/a. L11110.
- 2325 Shprits, Y. Y. and Thorne, R. M. (2004). Time dependent radial diffusion modeling
 2326 of relativistic electrons with realistic loss rates. *Geophysical Research Letters*,
 2327 31(8):n/a–n/a. L08805.
- 2328 Shumko, M., Sample, J., Johnson, A., Blake, B., Crew, A., Spence, H., Klumpar, D.,
 2329 Agapitov, O., and Handley, M. (2018). Microburst scale size derived from multiple
 2330 bounces of a microburst simultaneously observed with the firebird-ii cubesats.
 2331 *Geophysical Research Letters*, 45(17):8811–8818.
- 2332 Spence, H. E., Blake, J. B., Crew, A. B., Driscoll, S., Klumpar, D. M., Larsen,
 2333 B. A., Legere, J., Longworth, S., Mosleh, E., O’Brien, T. P., Smith, S., Springer,
 2334 L., and Widholm, M. (2012). Focusing on size and energy dependence of electron
 2335 microbursts from the van allen radiation belts. *Space Weather*, 10(11).
- 2336 Summers, D., Thorne, R. M., and Xiao, F. (1998). Relativistic theory of wave-particle
 2337 resonant diffusion with application to electron acceleration in the magnetosphere.
 2338 *Journal of Geophysical Research: Space Physics*, 103(A9):20487–20500.
- 2339 Takahashi, K. and Denton, R. E. (2007). Magnetospheric seismology using multi-
 2340 harmonic toroidal waves observed at geosynchronous orbit. *Journal of Geophysical
 2341 Research: Space Physics*, 112(A5).
- 2342 Thorne, R. M. (2010). Radiation belt dynamics: The importance of wave-particle
 2343 interactions. *Geophysical Research Letters*, 37(22). L22107.

- 2344 Thorne, R. M. and Andreoli, L. J. (1981). *Mechanisms for Intense Relativistic*
 2345 *Electron Precipitation*, pages 381–394. Springer Netherlands, Dordrecht.
- 2346 Thorne, R. M., O'Brien, T. P., Shprits, Y. Y., Summers, D., and Horne, R. B. (2005).
 2347 Timescale for MeV electron microburst loss during geomagnetic storms. *Journal*
 2348 *of Geophysical Research: Space Physics*, 110(A9). A09202.
- 2349 Trefall, H., Bjordal, J., Ullaland, S., and Stadsnes, J. (1966). On the extension of
 2350 auroral-zone x-ray microbursts. *Journal of Atmospheric and Terrestrial Physics*,
 2351 28(2):225–233.
- 2352 Tsurutani, B. T. and Lakhina, G. S. (1997). Some basic concepts of wave-particle
 2353 interactions in collisionless plasmas. *Reviews of Geophysics*, 35(4):491–501.
- 2354 Tsurutani, B. T., Lakhina, G. S., and Verkhoglyadova, O. P. (2013). Energetic
 2355 electron ($\gtrsim 10$ kev) microburst precipitation, $\sim 5\text{--}15$ s x-ray pulsations, chorus,
 2356 and wave-particle interactions: A review. *Journal of Geophysical Research: Space*
 2357 *Physics*, 118(5):2296–2312.
- 2358 Tsyganenko, N. (1989). A solution of the chapman-ferraro problem for an ellipsoidal
 2359 magnetopause. *Planetary and Space Science*, 37(9):1037 – 1046.
- 2360 Tsyganenko, N. A. and Sitnov, M. I. (2005). Modeling the dynamics of the inner
 2361 magnetosphere during strong geomagnetic storms. *Journal of Geophysical Research:*
 2362 *Space Physics*, 110(A3).
- 2363 Turner, D., Lee, J., Claudepierre, S., Fennell, J., Blake, J., Jaynes, A., Leonard,
 2364 T., Wilder, F., Ergun, R., Baker, D., et al. (2017). Examining coherency
 2365 scales, substructure, and propagation of whistler mode chorus elements with
 2366 magnetospheric multiscale (mms). *Journal of Geophysical Research: Space Physics*,
 2367 122(11).
- 2368 Ukhorskiy, A. Y., Anderson, B. J., Brandt, P. C., and Tsyganenko, N. A. (2006).
 2369 Storm time evolution of the outer radiation belt: Transport and losses. *Journal of*
 2370 *Geophysical Research: Space Physics*, 111(A11):n/a–n/a. A11S03.
- 2371 Van Allen, J. A. (1959). The geomagnetically trapped corpuscular radiation. *Journal*
 2372 *of Geophysical Research*, 64(11):1683–1689.
- 2373 Vernov, S. and Chudakov, A. (1960). Investigation of radiation in outer space. In
 2374 *International Cosmic Ray Conference*, volume 3, page 19.
- 2375 Walker, A. D. M. (1993). *Plasma waves in the magnetosphere*, volume 24. Springer
 2376 Science & Business Media.

- 2377 Woodger, L., Halford, A., Millan, R., McCarthy, M., Smith, D., Bowers, G., Sample,
2378 J., Anderson, B., and Liang, X. (2015). A summary of the BARREL campaigns:
2379 Technique for studying electron precipitation. *Journal of Geophysical Research:*
2380 *Space Physics*, 120(6):4922–4935.

APPENDIX: APPENDIX A

2382 This appendix contains Figs. A.1 and A.2. Figure A.1 shows evidence that
2383 supports our claim that the “hiss-like” chorus wave observed at 11:17:03 UT with
2384 EMFISIS WFR instrument on RBSP-A was parallel propagating. The polar angle
2385 of the wave vector and the supporting planarity of the magnetic field polarization
2386 shown in Fig. A.1 was calculated using the singular value decomposition (SVD)
2387 method (Santolk et al., 2003).

2388 Figure A.2 supports the claim that RBSPICE-A observed a 10-80% increase in
2389 the count rates at the microburst times and pitch angles. Figure A.2 shows the ratio
2390 of the RBSPICE-A’s EBR count rates during the four microbursts to the quiet time
2391 one spin before, at the same pitch angles.

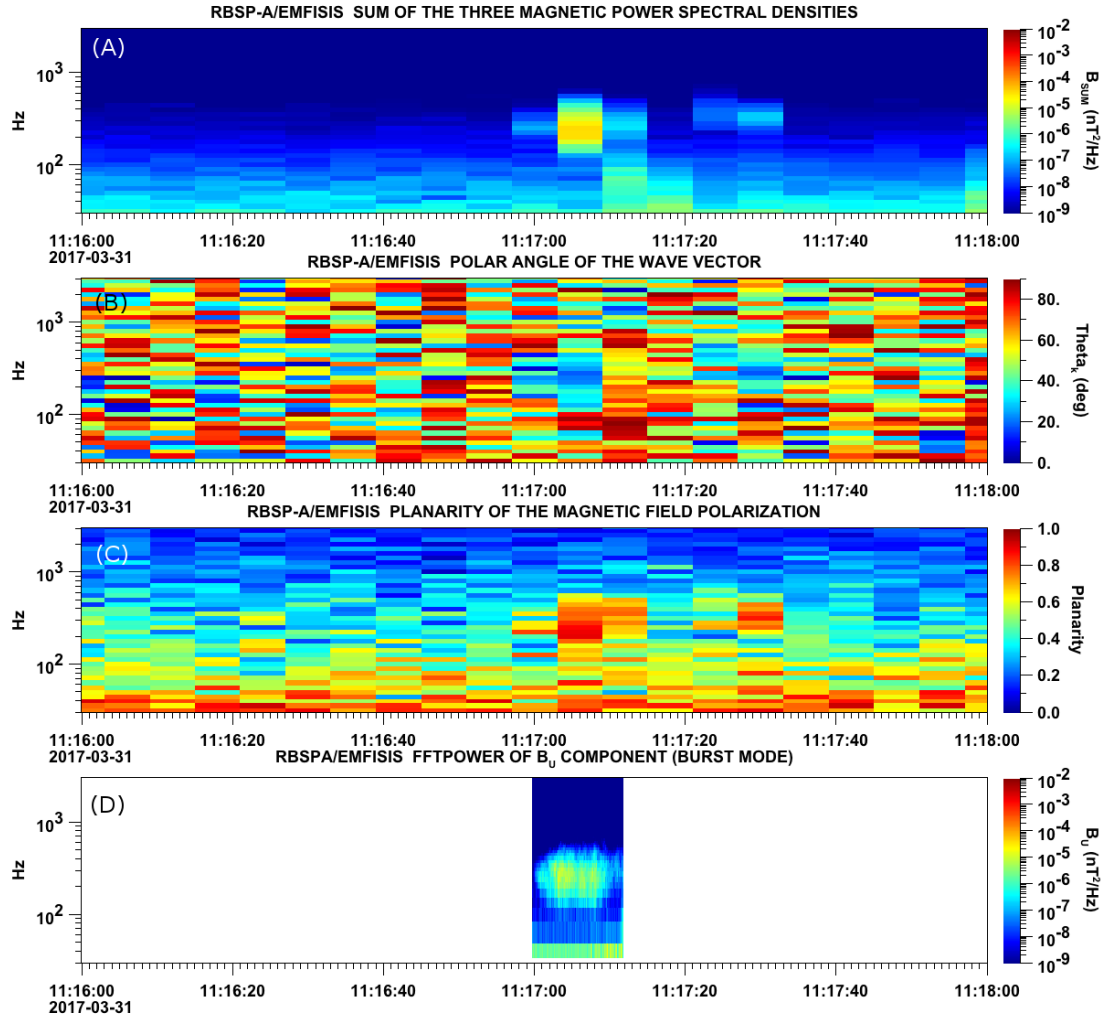


Figure A.1: Panel (A) shows the magnetic power spectral density as a function of frequency and time from the EMFISIS WFR instrument on board RBSP-A. The “hiss-like” wave used for the resonant diffusion analysis was observed starting at 11:17:03 UT. In the same format as panel (A), panel (B) shows the polar angle of the wave vector for this time period. The wave of interest had a normal wave vector, $\theta_k < 30^\circ$. Since the results in panel (B) are valid only for high planarity, panel (C) shows planarity in the same format as panels (A) and (B). The wave of interest was found to have a planarity of > 0.8 . Lastly, panel (D) shows the available burst mode data.

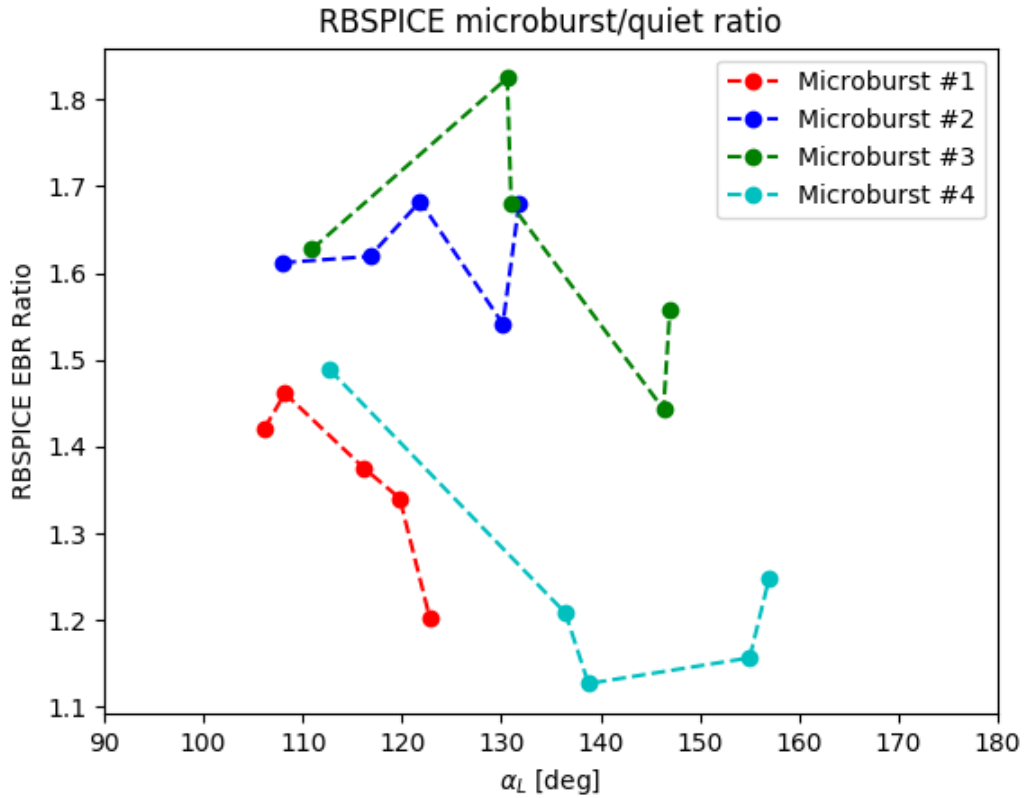


Figure A.2: Ratio of the RBSPICE EBR at microburst times indicated with the black vertical arrows in Fig. 2, to the EBR at the same pitch angles one spin prior (quiet time). The microburst flux was enhanced by 10-80% across $100^\circ < \alpha_L < 160^\circ$ PA, and appear to be peaked closer to $\alpha_L = 90^\circ$.

2393 This appendix describes the method we used to calculate the time difference and
 2394 separation between FU3 and FU4 at 06:12 UT on February 2nd, 2015. We used the
 2395 following method to calculate the clock difference, δt_c and separation, d between FU3
 2396 and FU4 at 06:12 UT on February 2nd, 2015.

2397 The relative clock difference was calculated with a cross-correlation time
 2398 lag analysis on uniquely-identified trains of microbursts that hit both spacecraft
 2399 simultaneously. Four time periods with coincident microbursts were hand-picked on
 2400 February 2nd, 2015 and are shown in Figs. B.1-B.4, panels (a) and (b). The cross-
 2401 correlation time lag analysis was applied to the HiRes time series in panels (a) and
 2402 (b), and the resulting normalized cross-correlation coefficient as a function of time is
 2403 shown in panel (c). To validate the peak lag identified in panel (c), FU3's time series
 2404 was shifted by that lag and is shown in panel (d).

2405 The clock differences from the simultaneous microbursts in Figs. B.1-B.4 were
 2406 linearly fit to account for the relative clock drift (≈ 20 ms/hour at this time), giving
 2407 a value of $\delta t_c = 2.28 \pm 0.12$ s at the time of the microburst analyzed here. This time
 2408 shift was applied to the HiRes data in Fig. 1. A clock difference of $\delta t_c = 2.45^{+0.51}_{-0.98}$ s
 2409 was independently calculated with the FIREBIRD-II telemetry beacon time stamps
 2410 that were downlinked during operational passes.

2411 We calculate the spacecraft separation, by applying same the cross-correlation
 2412 time lag analysis on structures assumed to be spatial and are shown in Figs. B.5
 2413 and B.6. The lag from the peak cross-correlation between these events is a sum of
 2414 the clock difference and time lag due to the spacecraft separation. We interpret the
 2415 time lag due to the spacecraft separation as the time difference between when the
 2416 leading satellite observed a stationary spatial feature, to when the trailing satellite
 2417 observed the same stationary spatial feature. With the method described above, we
 2418 find the spatial time lag to be $\delta t_d = 2.64 \pm 0.12$ s (after we account for the clock
 2419 difference and its uncertainty). To convert from a spatial time lag to a spacecraft
 2420 separation, we calculate the satellite velocity. We calculate the velocity using a Two
 2421 Line Element (TLE), a data format containing the orbit parameters that are used
 2422 for orbit propagation. With the TLE derived spacecraft velocity, $v = 7.57$ km/s, the
 2423 spacecraft separation was $d = 19.9 \pm 0.9$ km.

2424 An independent method to calculate the spacecraft separation was developed.
 2425 The separation was calculated using TLEs. The TLE from February 2nd was
 2426 anomalous and was not used in this analysis. Instead, seven TLEs released up to
 2427 five days after the microburst event were backpropagated, using the SGP-4 algorithm
 2428 (Hoots and Roehrich, 1980) that calculates orbital state vectors with perturbations
 2429 such as Earth's atmosphere, as well as gravitational effects from the moon and sun.
 2430 Then the predicted spacecraft separations at the time of the microburst event were

²⁴³¹ averaged to derive a separation of $d = 18.4 \pm 1.5$ km. These two methods give
²⁴³² similar separations, which implies that the stationary event assumption used in the
²⁴³³ cross-correlation time lag analysis is reasonable.

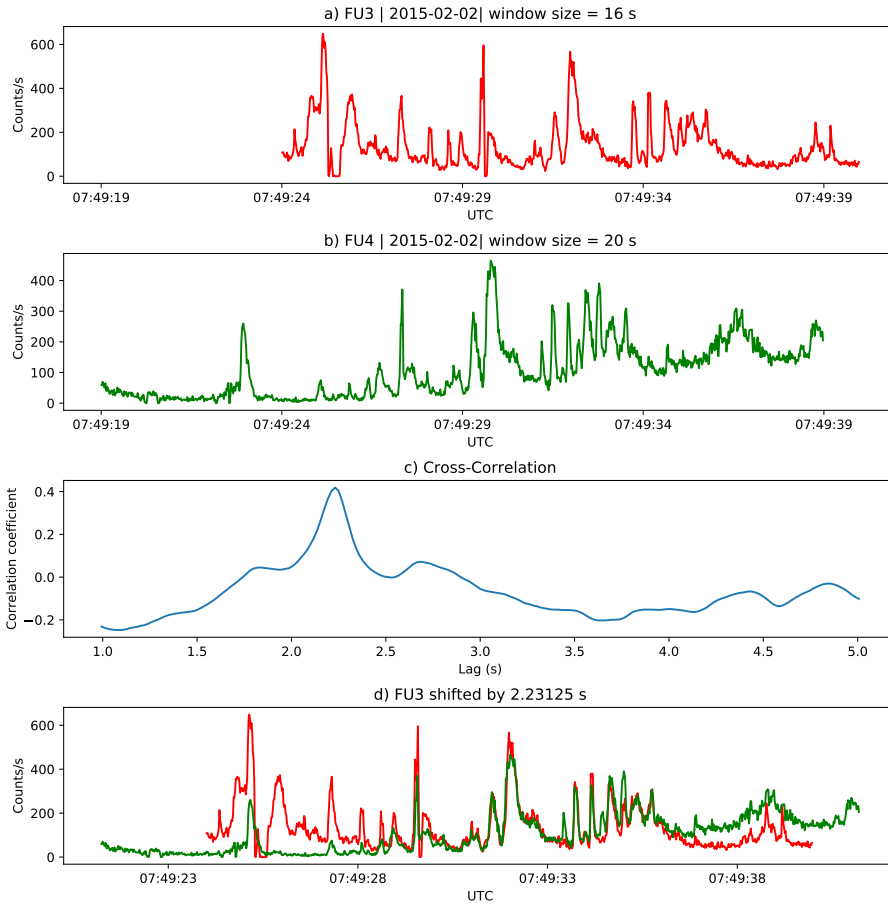


Figure B.1: Cross-correlation time lag analysis applied to a train of microbursts. Panel (a) and (b) show the count rate from the lowest energy channel. Panel (c) shows the cross-correlation coefficient as a function of time lag. Panel (d) shows the shifted timeseries. Clock difference was 2.23 s.

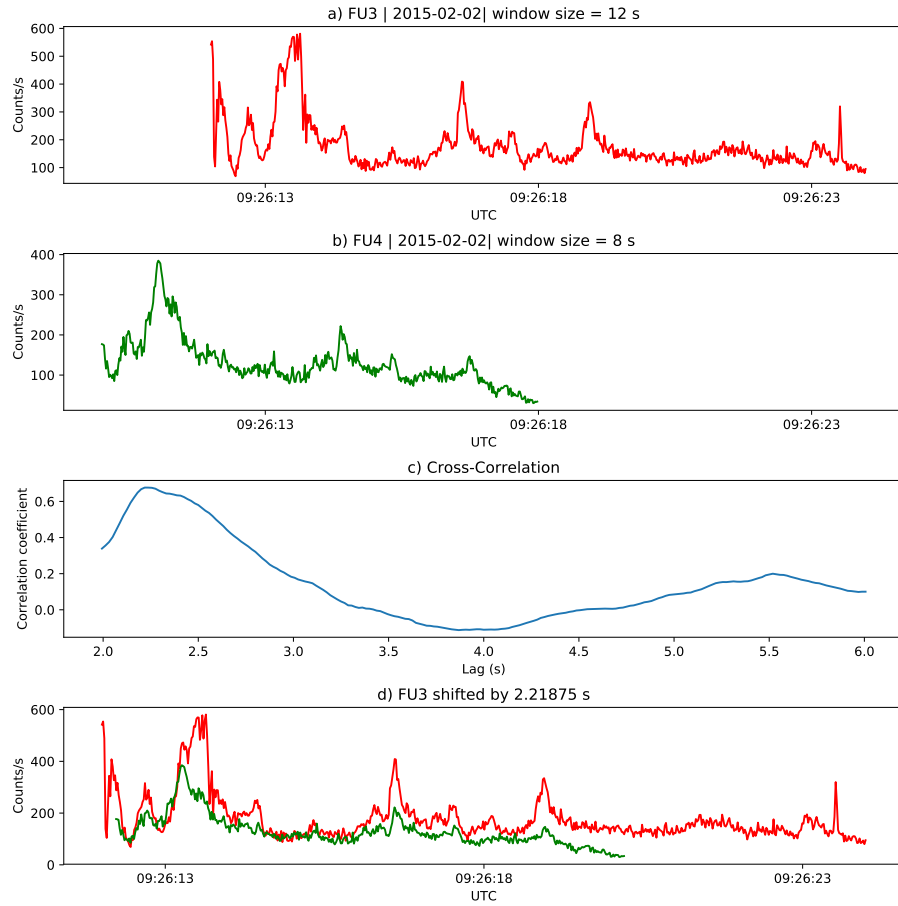


Figure B.2: Same analysis as Fig. B.1 on a different time period. Clock difference was 2.21 s.

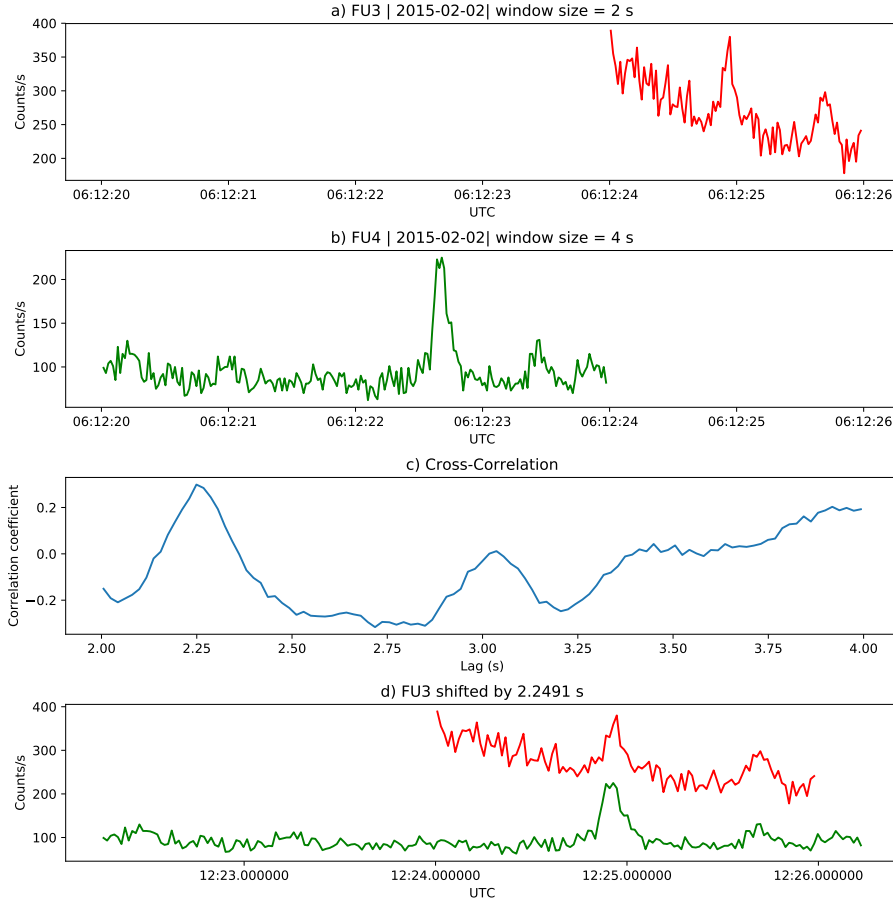


Figure B.3: Same analysis as Fig. B.1 on a different time period. Clock difference was 2.25 s.

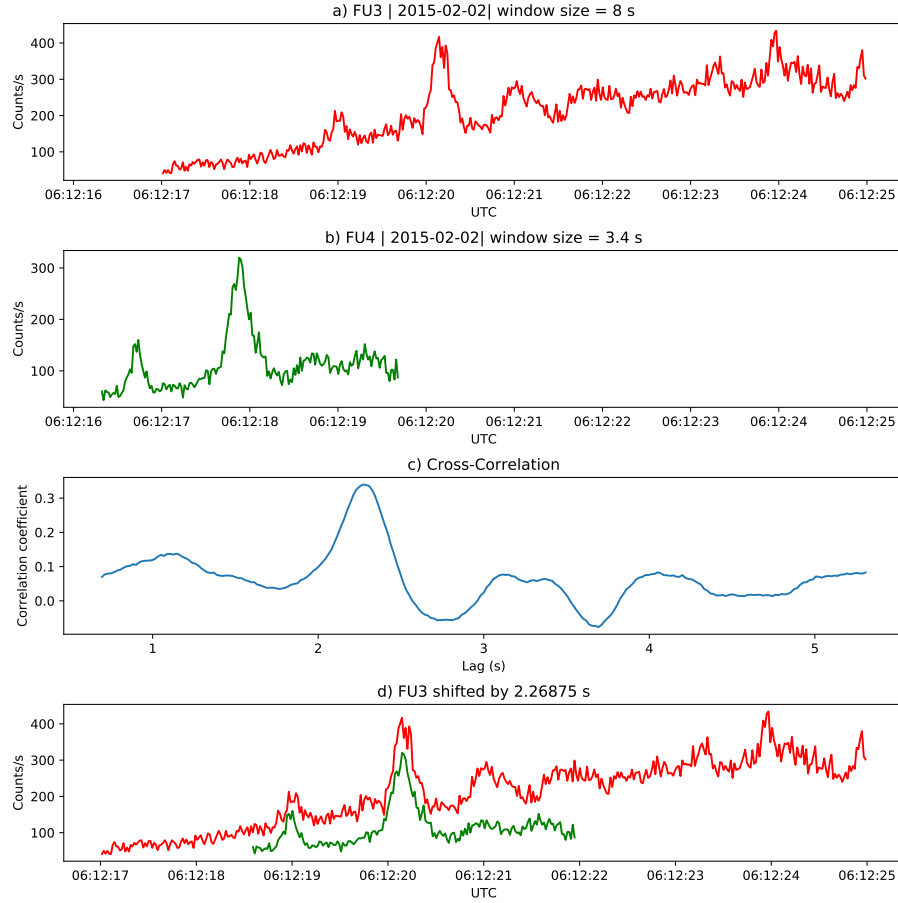


Figure B.4: Same analysis as Fig. B.1 on a different time period. Clock difference was 2.27 s.

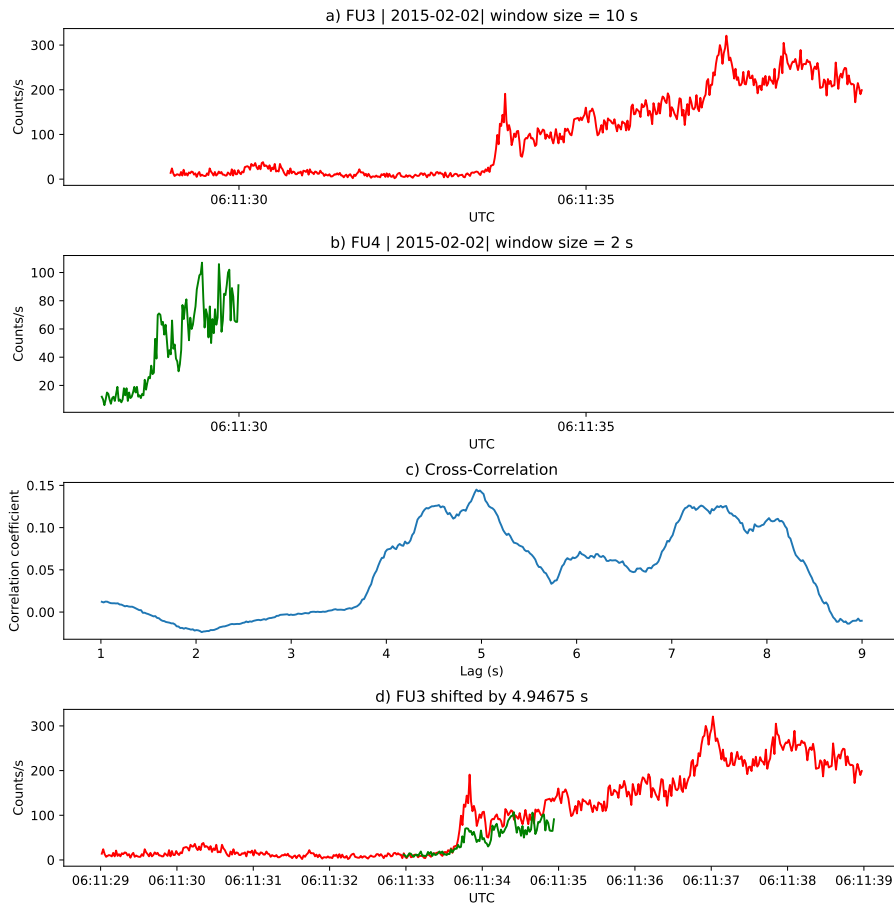


Figure B.5: Same cross-correlation time lag analysis applied to stationary spatial structures. The cross-correlation lag between these events is a sum of the clock difference and time lag due to the spacecraft separation. The lag derived at this time was 4.95 s.

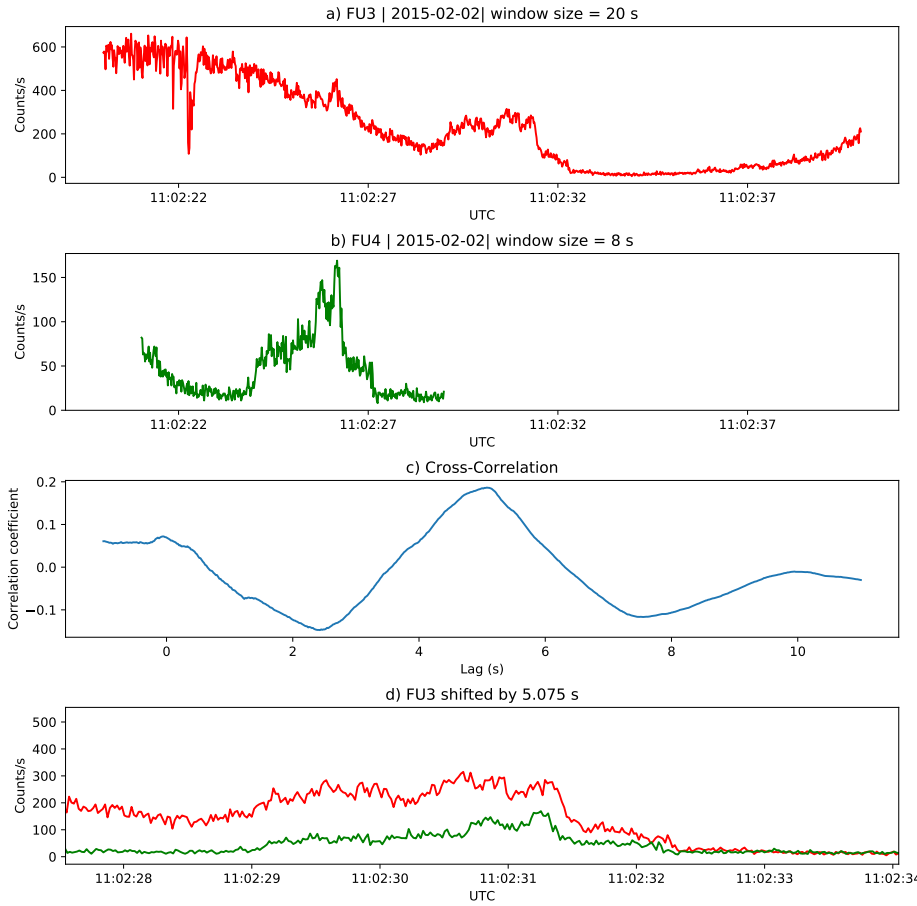


Figure B.6: Same analysis as Fig. B.5 applied to a different stationary spatial feature. The lag derived at this time was 5.01 s.

2435 This appendix contains texts S1-S3. Text S1 derives the analytic model that
2436 transforms a prescribed microburst PDF into a \bar{F} curve as a function of AC6
2437 separation, s . Text S2 expands on the two-sized microburst model results presented
2438 in Section 5.3 and the range of optimal model parameters assuming continuous
2439 microburst PDFs such as the log-normal, Weibull, and Maxwellian. Lastly, text
2440 S3 presents the percent of microbursts observed in each separation bin, as a function
2441 of separation and compares it to the observed scale size of chorus waves as a function
2442 of wave amplitude.

2443 **Text S1: Analytic Derivation of $\bar{F}(s)$** Here we derive the integral form of $\bar{F}(s)$
2444 under the following assumptions:

- 2445 1. microbursts are circular with radius r
2446 2. microbursts are randomly and uniformly distributed around AC6.

First recall the area $A(r, s)$, given in Eq. 4 in the main text and copied here for convenience

$$A(r, s) = 2r^2 \cos^{-1} \left(\frac{s}{2r} \right) - \frac{s}{2} \sqrt{4r^2 - s^2}. \quad (\text{C.1})$$

2447 A circular microburst who's center lies in $A(r, s)$ will be observed by both AC6 units
2448 and is counted in $\bar{F}(s)$. Now we derive the integral form of $\bar{F}(s)$ that accounts for
2449 the different spacecraft separations and microburst sizes that are distributed by a
2450 hypothesized PDF $p(r, \theta)$.

2451 First we will account for the effects of various spacecraft separation, assuming all
2452 microbursts are one size. For reference choose of radius, r_0 and spacecraft separation,
2453 s_0 such that $A(r_0, s_0) > 0$ which implies that some number of microbursts, n_0 will be
2454 simultaneously observed. Now, if for example the spacecraft separation (or microburst
2455 radius) is changed such that the area doubles, the second assumption implies that the
2456 number of microbursts observed during the same time interval must double as well.
2457 This can be expressed as

$$\frac{n_0}{A(r_0, s_0)} = \frac{n}{A(r, s)} \quad (\text{C.2})$$

2458 and interpreted as the conservation of the microburst area density. By rewriting Eq.
2459 C.2 as

$$n(r, s) = \left(\frac{n_0}{A(r_0, s_0)} \right) A(r, s) \quad (\text{C.3})$$

2460 it is more clear that the number of microbursts of size r observed at separation s is
2461 just $A(r, s)$ scaled by the reference microburst area density. The cumulative number
2462 of microbursts observed above s is then

$$N(r, s) = \int_s^\infty n(r, s') ds' = \left(\frac{n_0}{A(r_0, s_0)} \right) \int_s^\infty A(r, s') ds'. \quad (\text{C.4})$$

2463 Lastly, $\bar{F}(s)$ for a single r is then

$$\bar{F}(s) = \frac{N(s)}{N(0)} = \frac{\int_s^\infty A(r, s') ds'}{\int_0^\infty A(r, s') ds'} \quad (\text{C.5})$$

2464 To incorporate a continuous microburst PDF such as $p(r) = p_1\delta(r - r_1) + p_2\delta(r -$
2465 $r_2) + \dots$ we sum up the weighted number of microbursts that each size contributes to

₂₄₆₆ $N(s)$ i.e.

$$N(s) = \left(\frac{n_0}{A(r_0, s_0)} \right) \left(\int_s^\infty p_1 A(r_1, s') ds' + \int_s^\infty p_2 A(r_2, s') ds' + \dots \right) \quad (\text{C.6})$$

₂₄₆₇ The last step is to convert the sum of Dirac Delta functions into a continuous
₂₄₆₈ PDF $p(r)$ after which

$$N(s) = \left(\frac{n_0}{A(r_0, s_0)} \right) \int_s^\infty \int_0^\infty A(r, s') p(r) dr ds'. \quad (\text{C.7})$$

₂₄₆₉ With these considerations, $\bar{F}(s)$ is then given by

$$\bar{F}(s, \theta) = \frac{\int_s^\infty \int_0^\infty A(r, s') p(r, \theta) dr ds'}{\int_0^\infty \int_0^\infty A(r, s') p(r, \theta) dr ds'} \quad (\text{C.8})$$

2470 Text S2: Most probable parameter values for continuous microburst PDFs

2471 Besides the one and two-size microburst models described in the main text,
2472 continuous PDFs such as the log-normal, Weibull, and Maxwellian were fit and their
2473 optimal parameters presented here.

2474 For the Maxwellian PDF, we assumed the following form

$$p(r|a) = \sqrt{\frac{2}{\pi}} \frac{r^2 e^{-r^2/(2a^2)}}{a^3}. \quad (\text{C.9})$$

The range of a consistent with the observed data was found to be between 0 and 35 km. Next, the log-normal distribution of the following form was used

$$p(r|\mu, \sigma) = \frac{1}{\sigma r \sqrt{2\pi}} e^{\left(-\left(\ln(r)-\ln(\mu)\right)^2/(2\sigma^2)\right)} \quad (\text{C.10})$$

and the results are summarized in C.1. Lastly the Weibull distribution of the following form was tested

$$p(r|c, r_0, \lambda) = c \left(\frac{r - r_0}{\lambda} \right)^{c-1} \exp \left(- \left(\frac{r - r_0}{\lambda} \right)^c \right). \quad (\text{C.11})$$

2475 for which the model parameters are summarized in Table C.2.

Table C.1: Range of log-normal model parameters consistent with the observed AC6 $\bar{F}(s)$

percentile (%)	μ	σ
2.5	1.8	0
50	21.8	0.4
97.5	52.0	1.1

Table C.2: Range of Weibull model parameters consistent with the observed AC6 $\bar{F}(s)$

percentile (%)	c	r_0	λ
2.5	0.6	1.3	2.7
50	5.5	26.2	32
97.5	19.3	72.5	72.2

²⁴⁷⁶ **Text S3: Comparison of microburst to whistler mode chorus $\bar{F}(s)$**
²⁴⁷⁷ **TBD**